



universität
wien

MASTERARBEIT

Titel der Masterarbeit

„Pressure dependence of the Sn-P phase diagram and investigations in the ternary system Ni-P-Sn“

Verfasserin

Anna Ritscher, Bakk.rer.nat

angestrebter akademischer Grad

Master of Science (MSc)

Wien, Juni.2012

Studienkennzahl lt. Studienblatt:

A 066 862

Studienrichtung lt. Studienblatt:

Masterstudium Chemie

Betreuer:

O. Univ.-Prof. Dr. Herbert Ipser

Acknowledgement

The present work was done from August 2011 to June 2012 under the supervision of o. Univ.-Prof. Dr. Herbert Ipser at the Department of Inorganic Chemistry/ Materials Chemistry at the University of Vienna.

First of all I want to express my gratitude to Prof. H. Ipser for his guidance and his constant and encouraging support of the whole research work. I am very thankful for the opportunity to write my Master thesis in his institute and for the help concerning all questions to theoretical and experimental details.

Furthermore I want to thank all my colleagues for the very warm welcome at the department, the friendly working atmosphere and for helping me with all kind of practical questions.

Also, I am very thankful to my family, who always supported me in every possible way during my studies, as well as to all of my friends for their interest and for making my life exciting and swinging.

Moreover, thanks go to Dr. Clemens Schmetterer for his advises and for sharing his knowledge of the challenging phosphorus-tin system.

I also want to thank Dr. Stephan Puchegger, from the Department of Physics, for his support at SEM measurements.

Finally the financial support of the Austrian Science Foundation FWF (Fonds zur Förderung der wissenschaftlichen Forschung) is gratefully acknowledged.

TABLE OF CONTENT

1 Introduction	1
2 Literature review	4
2.1 Phosphorus and its vapor pressure 4	
2.2 Binary systems 5	
2.2.1 Sn-P 5	
2.2.2 Ni-P 9	
2.2.3 Ni-Sn 13	
2.3 Ternary system Ni-P-Sn 16	
3 Applied methods	19
3.1 Isopiestic method 19	
3.2 X-ray powder diffraction (XRD) 20	
3.2.1 Formation of X-rays 20	
3.2.2 Diffraction of X-rays, powder diffraction 21	
3.2.3 Instrumental setup 23	
3.2.4 Rietveld refinement 23	
3.3 Light optical microscopy (LOM) 24	
3.4 Scanning electron microscopy (SEM) 26	
4 Experimental	29
4.1 The binary system Sn-P 29	
4.1.1 Preparation of samples, Isopiestic method 29	
4.1.2 XRD 32	
4.2 The ternary system Ni-P-Sn 33	
4.2.1 Sample preparation 33	
4.2.2 XRD 36	
4.2.3 Metallography 36	
4.2.3.1 LOM 37	
4.2.3.2 SEM 37	

5 Results and discussion 38

- 5.1 Results in the system Sn-P | 38
 - 5.1.1 Isopiestic measurements | 38
 - 5.1.1.1 Formation of Sn_3P_3 | 46
 - 5.1.1.2 Limiting liquidus composition | 50
 - 5.1.1.3 Formation of Sn_3P_4 | 52
 - 5.1.1.4 Formation of SnP_3 | 54
 - 5.1.2 Thermodynamic data | 57
 - 5.1.2.1 Partial enthalpy of mixing | 61
 - 5.1.2.2 Standard molar Gibbs energy of formation | 62
 - 5.1.2.2.1 Sn_3P_3 | 62
 - 5.1.2.2.2 Sn_3P_4 | 65
 - 5.1.2.2.3 SnP_3 | 67
- 5.2 Results in the system Ni-P-Sn | 69

6 Summary 74

- 6.1 Summary (English) | 74
- 6.2 Zusammenfassung (Deutsch) | 76

7 References 78

8 Appendices 85

- 7.1 List of figures | 85
- 7.2 List of tables | 87
- 7.3 Curriculum vitae | 88

1 Introduction [1, 2]

Electroless nickel plating, sometimes also called auto-catalytic or chemical plating, is a widely used plating process that provides a uniform deposition of nickel layers on metallic or non-metallic substrates without the need for an external current.

For example, in the electronic industry Cu is a common contact material for printed circuit boards (PCBs). It is used in the under bump metallization (UBM) for ball grid arrays (BGA) and in flip chip technology. However, Cu suffers easily from oxidation during storage so the surface has to be protected by surface layers. Furthermore the Ni-layer serves as diffusion barrier between Cu and the Sn-rich solder and thus prevents dissolving of Cu and the extensive growth of intermetallic compounds (IMCs) of Cu-Sn. Nowadays Sn-based solders are the most attractive materials for the replacement for the conventional Pb-containing solders. Pb-Sn solders have long been used due to their excellent mechanical properties as well as great wetting properties. However, they are harmful relating to environmental reasons.

Electroless nickel plating is a controlled autocatalytic chemical reduction process for the deposition of protective coatings. It was first applied by Brenner and Riddell [3] in 1947. Usually the layers have a thickness of 5-10 μm . Electroless plating is a quite cheap technique and only basic equipment is required. Characteristics of these Ni-coatings are large areas of uniform thickness, great corrosion resistance, low stress, excellent solderability and selective deposition. These qualities make the method advantageous to the normal electroplated Ni.

The principle of electroless plating is the continuous development of a nickel coating on a substrate which is immersed into a plating bath. The plating bath generally consists of a nickel salt, which is dissolved in an aqueous solution, together with a reductant and a complexing agent as a pH-buffer. Sodium hypophosphite (NaH_2PO_2) is often used as reducing agent.

During the plating process it cannot be avoided that also P is deposited on the substrate. The obtained electroless nickel layers can incorporate up to 15 at% P [4]. The microstructure of the Ni(P)-coating changes with the amount of P. The layers have crystalline structure at lower P-contents but get amorphous for contents above

9.5 at% [5, 6]. The deposition rate is also affected by the pH-value of the plating bath, a higher pH leads to thicker Ni(P)-layers but with lower P-content [6].

In recent years the use of Au-finish after electroless Ni plating has increased. In this technique, which is called electroless nickel/immersion gold (ENIG) (Fig. 1.1), after the deposition of the amorphous Ni(P) layer the surface is covered with an ultra thin layer of Au as contact material. The gold is applied to the Ni(P) coating in order to protect it until the soldering process. Additionally the Ni(P)/Au layer provides good wettability, also after several reflows and has a higher mechanical strength and better fatigue resistance than Cu [7]. The Au-layer has to be of a suitable thickness in order to maintain the solderability of Ni. The Au-layer itself is not considered in the majority of the solder related literature because it gets dissolved entirely during soldering.

Hence, during the soldering process the Ni(P) layers interact with the solder material. A high number of studies are found in literature about this topic. All previous studies about the interfacial reactions between Ni(P) with Sn-based solders and the developing reaction products were performed without any knowledge of the phase equilibria in the ternary system Ni-P-Sn. However, in some papers possible reaction products were described, e.g. the formation of Ni_3Sn_4 [8]. Some authors reported the formation of the binary compound Ni_3P in the joint [7, 9], others also identified further nickel phosphides, such as Ni_2P and Ni_{12}P_5 [10-12]. This varying formation of phosphides is in some extent affected by the amount of P in the original Ni(P) layer. In other studies the formation of Ni-P-Sn layers [13, 14] is described whereas some authors claimed the formation of ternary IMC layers such as Ni_2PSn [11, 12] and Ni_3PSn [15], a ternary compound whose existence is not clarified yet.

The formation of Ni_3P deteriorates the quality of the soldering joint due to the formation of voids in the Ni(P) layer and, thus, to the diffusion of Cu from the substrate to the solder material or the Ni_3Sn_4 . Then IMCs containing Sn-Cu are formed, e.g. $(\text{Ni}_{1-x}\text{Cu}_x)_3\text{Sn}_4$ [8].

In order to understand the occurring reactions during the soldering process and to identify and characterize the reaction products, it is absolutely necessary to entirely know all of the corresponding phase diagrams. More precisely, to determine the interaction of Sn-based solders with the Ni(P) substrate, knowledge about the ternary

system Ni-P-Sn as well as the binary phase diagrams Sn-P, Ni-P and Ni-Sn are needed. Especially, for the system Sn-P limited experimental information is available and it shows a strong dependence on the vapour pressure of P.

The present work concentrated on the experimental research of the binary system Sn-P and the ternary system Ni-P-Sn. The binary system was investigated by means of vapour pressure measurements using an isopiestic technique. Other experimental techniques were X-ray powder diffraction (XRD) and scanning electron microscopy (SEM) as a metallographic method.

The work was performed with the aim to improve the existing phase diagram version and to better understand the vapor pressure dependence of the system Sn-P. Furthermore, the ternary phase diagram should be investigated at lower temperatures in the Sn-rich part of the system.

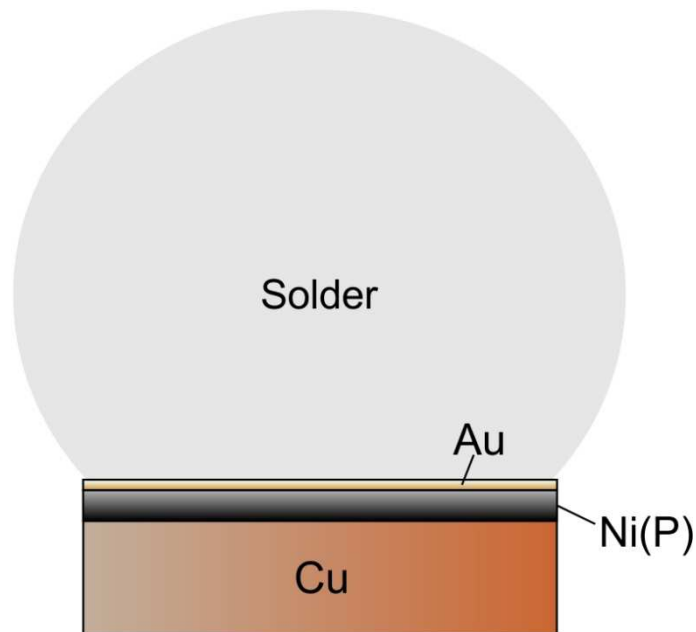


Fig. 1.1 Schematic illustration of UBM-process with ENIG-protected Cu

2 Literature review

2.1 Phosphorus and its vapor pressure

The element phosphorus occurs in four allotropic modifications with different colors, white (or yellow), red, violet and black phosphorus. At room temperature the thermodynamic stability of the modifications increases in the order $P_{\text{white}} \rightarrow P_{\text{red}} \rightarrow P_{\text{violet}} \rightarrow P_{\text{black}}$. However, the transformation rate is so small under standard conditions that the white, red and violet modifications are stable besides the black phosphorus. With increasing temperature, the stability changes, above 550 °C the violet modification is the most stable one and above 620 °C the white one, as gaseous $P_4(g)$.

Black phosphorus can be obtained by heating white phosphorus under pressure; it has an orthorhombic structure with puckered layers, resembling graphite. With increasing pressure the orthorhombic structure changes into a rhombohedral (~80 kbar) or into a simple cubic structure (~110 kbar). The violet modification of phosphorus is also known as Hittorf's phosphorus (Johann W. Hittorf 1865). It has a complex monoclinic structure and is produced by annealing P_{white} above 550 °C for some days. Red phosphorus can be produced by heating P_{white} at about 200-400 °C. It exists as an amorphous network but can crystallize on further heating.

The most reactive modification of phosphorus is the white one with a boiling point of 280 °C. As a solid and as a liquid it consists mostly of tetrahedral P_4 molecules, also in the vapor P_4 is the dominant species up to the temperature of 800 °C. There the tetrahedral decompose more and more to P_2 -molecules (dissociation rate at 800 °C is ~1 %), at 1200 °C already 50 % of the gas phase consists of P_2 . Above 2000 °C the P_2 -molecules decompose to P-atoms. As white phosphorus gradually changes to the red modification it often appears yellow. White phosphorus is very reactive and is a pyrophoric material. This and further information can be found in Reference [16].

In the present experimental work the major factor of interest is the vapor pressure of the element which is strongly dependent on the temperature. It is known that the vapor pressure of the white modification is higher than that of red phosphorus [17]. This fact ensures that the pressure during the isopiestic experiments (see sections 3.1 and 5.1.1) is exclusively defined by the white modification.

2.2 Binary systems

2.2.1 Sn-P

Except for a limited number of experimental data, the system Sn-P has not been studied in detail.

The current version of the phase diagram printed in Massalski et al. [18] is primarily based on the work of Vivian [19]. His measurements were also the basis to draw the phase diagram reported by Hansen and Anderko [20].

Furthermore Olofsson [21] carried out XRD investigations on the system but did not establish a phase diagram version.

The early study of Vivian [19] is based on the investigation of samples prepared in pressure tubes. From his metallographic and thermal analysis he generated a phase diagram. In some of the samples he found two layers of molten material which differ in optical appearance. From this observation the author assumed the existence of two liquid miscibility gaps. The characteristic temperatures, obtained in the work, are based on thermal analysis using the cooling curves exclusively.

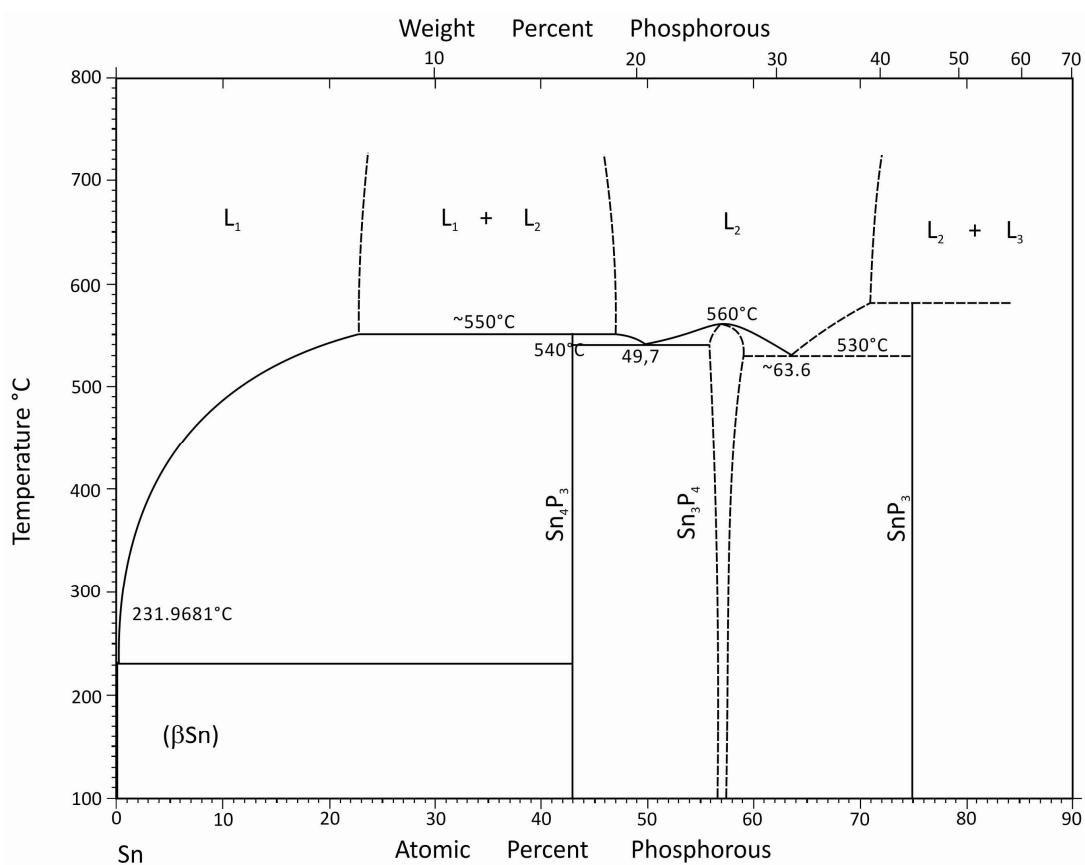


Fig. 2.1 Binary Sn-P phase diagram according to Massalski [18]

Arita and Kamo [22] studied the system applying vapor pressure measurements of phosphorus over the Sn-P alloys by the dew point method together with thermal analysis. According to the results of their study they published liquidus data up to a composition of 35 at% P and thermochemical data like thermodynamic activities and partial molar enthalpies of formation. Based on these results, Okamoto [23] established a phase diagram, in which, though, the data points of Arita and Kamo [22] were plotted incorrectly. This error was repeated by Predel [24] who based his work on Okamoto [23].

However, the phase diagram was considerably modified by Levinsky [25]. He considered the fact, that the system is very much depending on the high vapor pressure of phosphorus. Already Vivian [19] reported the difficulty of preparing samples with a P content of more than 8.5 wt% (≈ 26.2 at%), which required the use of pressure tubes. During the melting progress evaporation of P takes place, apparently the phase diagram is not isobaric. Levinsky [25] suggested a phase diagram fairly different to that printed in Massalski [18]. In his work he claimed that the binary compounds are formed directly out of the gas phase at a pressure of P less than 1 bar. This pressure dependent phase diagram is shown in Fig. 2.2 for a pressure of 0.7 bar. This proposition is also in agreement with the work of Zaikina et al. [26] who investigated the formation of Sn_3P_4 according to the reaction $\text{Sn}_4\text{P}_3 + \text{G} = \text{Sn}_3\text{P}_4$.

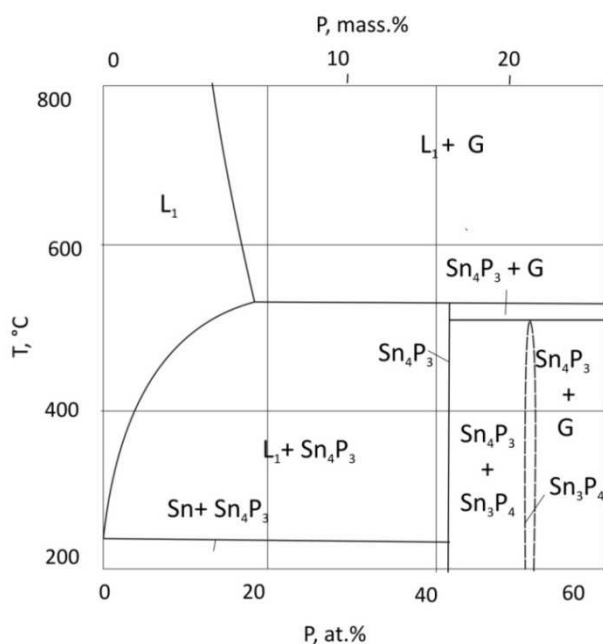


Fig. 2.2 Isobaric Sn-P phase diagram at a P pressure of 0.7 bar according to Levinsky [25]

A more recent experimental investigation of the system was done by Ganesan et al. [27]. This work is based on an isopiestic technique and Knudsen cell based mass loss measurements combined with the elaboration of thermodynamic models. It concentrates on the analysis of the phosphorus vapor pressure over samples of tin-phosphorus in a P concentration range of 0-71 at% up to temperatures of about 1000 K. The Knudsen cell mass loss method was used for low temperatures up to nearly 700 K. Based on these experimental results he obtained liquidus data and calculated standard molar Gibbs energies of formation for the three binary compounds Sn_4P_3 , Sn_3P_4 and SnP_3 as well as partial thermodynamic properties. These calculations are in good agreement with previous results from Arita and Kamo [22] at low temperatures but differ slightly with increasing T.

In a recently published book, Schmetterer et al. [28] reported new experimental results about the phase diagram Sn-P which also include the results of Ganesan et al. [27] mentioned above. They concentrated their investigations on the Sn-rich part of the system, again due to evaporation problems of phosphorus.

Their experimental results are mainly based on DTA measurements. The most Sn-rich invariant reaction, which was not specified in the work of Vivian [19] was discovered to be a eutectic reaction $L = (\text{Sn}) + \text{Sn}_4\text{P}_3$ close to the melting point of pure Sn at 231 °C. Schmetterer et al. [28] also reproduced the liquidus curve up to 23 at% P and found out that this latter composition is actually richer in Sn than the miscibility gap $[\text{L}_1+\text{L}_2]$ shown in Massalski [18]. However, other invariant reactions shown in [18] could not be confirmed by Schmetterer et al. [28] during DTA measurements due to the very strong evaporation of P at higher temperatures. Samples placed inside the predicted $[\text{L}_1+\text{L}_2]$ miscibility gap lost large amounts of P and the authors suggested that the phase diagram version of Levinsky [25] is more likely to be correct than the one printed in Massalski [18]. The compounds are formed out of the gas phase which is present over the entire composition range and not out of the liquid phase alone. The gas phase consists of almost pure phosphorus.

Structural data are also available for the system. Apart from the pure elements, the following three binary phases are found to be stable in the system under conventional conditions: Sn_4P_3 , Sn_3P_4 and SnP_3 .

The hexagonal structure of Sn_4P_3 was determined by Eckerlin and Kischio [29] and Olofsson [30] nearly at the same time. SnP_3 was first described by Gullman and Olofsson [31]. The crystal structure of Sn_3P_4 has been identified recently by Zaikina [26] and later confirmed by Ganesan et al. [32] through X-ray powder diffraction of a single phase sample. Other authors claimed the existence of the metastable or high pressure phases SnP (Katz et al. [33], Donohue [34]) and Sn_7P_{10} (Massalski [18]).

All structural details and all corresponding references are given in Tab.2.1.

Tab.2.1 Crystal structure data in the system Sn-P

Phase	Composition maximum range at%P	Pearson symbol	Space group	Strukturbericht	Proto-type	Cell dimension a[Å]	Cell dimension c[Å]	Reference
(β Sn)	0	<i>tI4</i>	<i>I4₁/amd</i>	A5	β Sn	5.8308()	3.181()	[35]
(α Sn)	0	<i>cF8</i>	<i>Fd$\bar{3}m$</i>	A4	C _{diamond}	5.5359()	-	[35]
Sn_4P_3	42.9	<i>hR7</i>	<i>R$\bar{3}m$</i>	-	Bi_3Se_4	3.9688(1)	35.34(1)	[29]
Sn_3P_4	~57.1	<i>hR7</i>	<i>R$\bar{3}m$</i>	-	-	4.4290(6)	28.360(6)	[26]
SnP_3	75	<i>hR8</i>	<i>R$\bar{3}m$</i>	-	SnP_3	7.3785(5)	10.5125(11)	[31]
Metastable/high pressure phases								
SnP	50	<i>cF8</i>	<i>Fm$\bar{3}m$</i>	B1	NaCl	5.5359(1)	-	[34]
	50	<i>hP16</i>	<i>P$\bar{3}m1$</i>	-		8.78(1)	5.98(1)	[33]
	50	<i>tI4</i>	<i>I4mm</i>	-	AsGe	3.831(1)	5.963(1)	[34]
Sn_7P_{10}	58.8	<i>h**</i>	-	-	-	-	-	[18]

2.2.2 Ni-P

Although there had been a lot of investigations in the system Ni-P the phase diagram is not clarified entirely. The present publications about the system do not show results over the entire composition range but are rather limited to the Ni-rich part of the system. The system cannot experimentally be investigated at higher P content due to the severe increasing vapor pressure of phosphorus at higher concentration, which was already mentioned for the system Sn-P (see section 2.2.1). This pressure dependence of the system Ni-P was described by Levinsky [36].

An earlier version of the phase diagram was established by Lee and Nash [37], which forms also the basis of the phase diagram version printed in Massalski [18]. Their work is focused on the Ni-rich part of the system up to a P-content of only 35 at% and thus is incomplete.

Information about the P-rich section is rare. Jolibois [38] as well as Biltz and Heimbrecht [39] published data for P contents beyond 66.7 at% and assumed the existence of the phases NiP_3 , NiP_2 and Ni_2P .

Other studies had been done by Konstantinov [40], who looked at cooling curves and did microscopic investigations. He was the first to suggest a high- and a low-temperature modification of Ni_5P_2 . Nowotny and Henglein [41] published crystallographic information on the system (Ni_3P , Ni_2P , Ni_5P_2 and $\text{Ni}_7\text{P}_3=\text{Ni}_{12}\text{P}_5$) and Yupko et al. [42] performed XRD and DTA measurements and introduced a high-temperature modification of Ni_{12}P_5 . Oryshchyn et al. [43] started investigations on the binary system based on XRD and EPMA measurements and were able to determine the structure of Ni_5P_2 LT.

The phase diagram was reinvestigated and modified by Schmetterer et al. [44] based on XRD, EPMA and DTA measurements up to a P content of 66.7 at%. They determined a considerable homogeneity range of the two high-temperature modifications of Ni_5P_2 and Ni_{12}P_5 as well as reaction temperatures and liquidus data of alloys between 35 and 66.7 at%. From these data they confirmed the existence of the phase NiP_3 also at room temperature.

According to these experimental data they established an adapted version of the phase diagram which is published in a review by Okamoto [45] (shown in Fig. 2.3). However, in the phase diagram the binary compound NiP_3 is plotted incorrectly as it

exists only at higher temperature. An enlarged version of the Ni-P system from 18 to 40 at% P is given in Fig. 2.4.

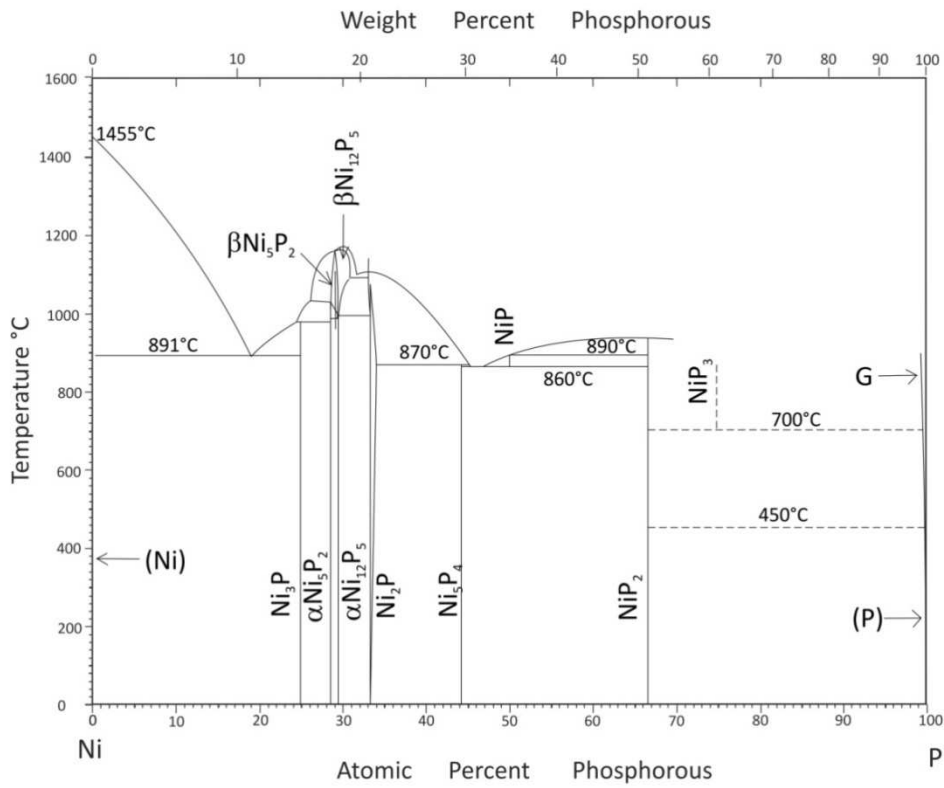


Fig. 2.3 Ni-P phase diagram according to Okamoto [45]

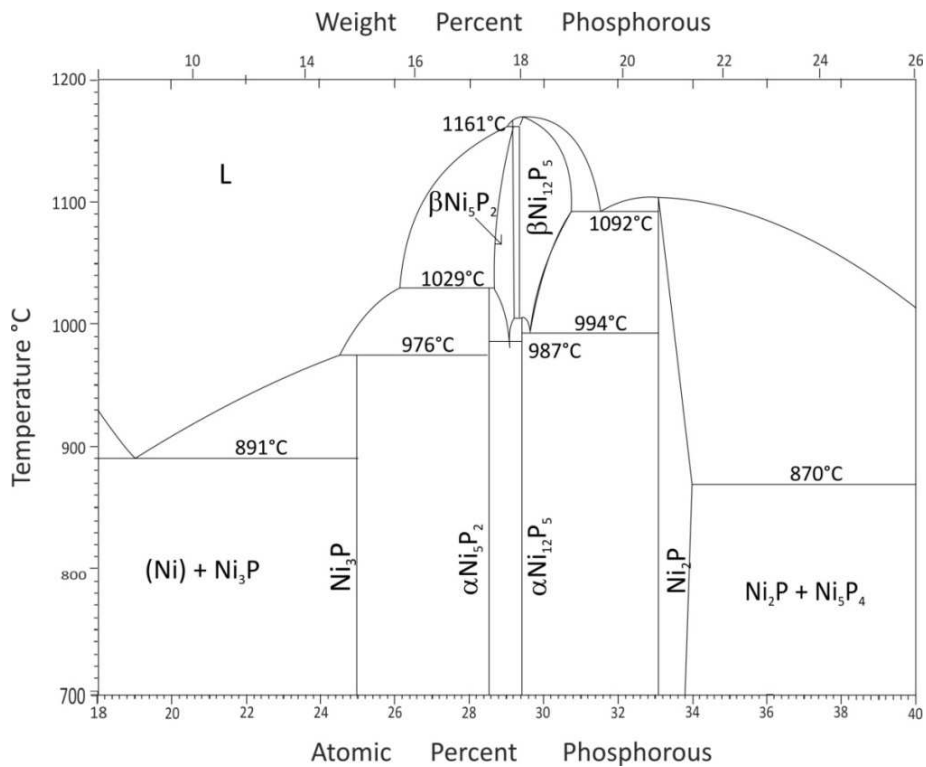


Fig. 2.4 Enlarged Ni-P phase diagram (18-40 at%P) according to Okamoto [45]

The available structural data and their corresponding references are given in Tab. 2.2.

Tab. 2.2 Crystal structure data of the system Ni-P (comp. maximum range according to Okamoto [45])

Phase	Composition maximum range at%P	Pearson symbol	Space group	Strukturbericht	Prototype	Reference
(Ni)	0	<i>cF4</i>	<i>Fm$\bar{3}m$</i>	A1	Cu	[46]
Ni ₃ P	25	<i>tI32</i>	<i>I$\bar{4}$</i>	D0 _e	Ni ₃ P	[47]
β Ni ₅ P ₂ / Ni ₅ P ₂ HT	28.7-29.2	-	-	-	-	[40]
α Ni ₅ P ₂ / Ni ₅ P ₂ LT	28.6	<i>hP168</i>	<i>P$\bar{3}$</i>	-	-	[43]
β Ni ₁₂ P ₅ / Ni ₁₂ P ₅ HT	29.4-30.7	-	-	-	-	[42]
α Ni ₁₂ P ₅ / Ni ₁₂ P ₅ LT	29.4	<i>tI34</i>	<i>I4/m</i>	-	-	[48]
Ni ₂ P	33.3-34	<i>hP9</i>	<i>P$\bar{6}2m$</i>	C22	Fe ₂ P	[49]
Ni ₅ P ₄	44.4	<i>hP36</i>	<i>P$\bar{6}_3mc$</i>	-	-	[50]
NiP	50	<i>aP16</i>	<i>Pcba</i>	-	-	[51]
NiP ₂	66.7	<i>mC12</i>	<i>C2/c</i>	-	-	[51]
NiP ₃	75	<i>cI32</i>	<i>I$\bar{m}\bar{3}$</i>	D0 ₂	CoAs ₃	[52]
P (red)	100	-	-	-	-	-

The structure Ni_{1.22}P which is present in the earlier phase diagram version of Lee and Nash [37] was reported by Larsson [51] but the phase could not be found in later work by Schmetterer et al. [44]

The work of Schmetterer et al. [44] also shows some changes at the invariant reactions concerning temperature and reaction type. A summary of all invariant reactions is shown in Tab. 2.3.

The thermochemistry of the system was already briefly summarized by Lee and Nash [37] and Schlesinger [53]. More recent thermodynamic data were given by Shim et al. [54] as well as by Ganesan et al. [55]. The version from Shim et al. [54] is based on thermodynamic modeling of the system, however it shows severe errors especially in the P-rich section due to incomplete description of the thermodynamic properties. Ganesan et al. [55] focused their work on isopiestic measurements and received new data for integral Gibbs energies and partial thermodynamic properties of P.

Tab. 2.3 Invariant reactions in the system Ni-P according to Schmetterer et al. [44]

Reaction	Temperature [°C]	Reaction type
$L \rightleftharpoons (Ni) + Ni_3P$	891	Eutectic
$L + Ni_5P_2 LT \rightleftharpoons Ni_3P$	976	Peritectic
$L + Ni_5P_2 HT \rightleftharpoons Ni_5P_2 LT$	1029	Peritectic
$Ni_5P_2 HT \rightleftharpoons Ni_5P_2 LT + Ni_{12}P_5 LT$	987	Eutectoid
$Ni_{12}P_5 HT \rightleftharpoons Ni_5P_2 HT + Ni_{12}P_5 LT$	~1006	Eutectoid
$L + Ni_{12}P_5 HT \rightleftharpoons Ni_5P_2 HT$	1161	Peritectic
$L \rightleftharpoons Ni_5P_2 HT$	-	*)
$L + Ni_5P_2 HT \rightleftharpoons Ni_{12}P_5 HT$	-	*)
$L \rightleftharpoons Ni_{12}P_5 HT$	1170	Congruent
$Ni_{12}P_5 HT \rightleftharpoons Ni_{12}P_5 LT + Ni_2P$	994	Eutectoid
$L \rightleftharpoons Ni_{12}P_5 HT + Ni_2P$	1092	Eutectic
$L \rightleftharpoons Ni_2P$	1105	Congruent
$L + Ni_2P \rightleftharpoons Ni_5P_4$	870	Peritectic
$L \rightleftharpoons Ni_2P + Ni_5P_4$	-	*)
$L \rightleftharpoons Ni_5P_4 + NiP$	863	Eutectic
$NiP \rightleftharpoons Ni_5P_4 + NiP_2$	860	Eutectoid
$L + NiP_2 \rightleftharpoons NiP$ (tentative)	~890	Peritectic
$Ni_5Sn_4 + NiP_2 \rightleftharpoons Ni_{1.22}P$	-	*)
$Ni_{1.22}P \rightleftharpoons Ni_5Sn_4 + NiP_2$	-	*)
$NiP_3 \rightleftharpoons NiP_2 + G$	-	*)

*) these invariant reactions from literature [37] were not found in [44]

2.2.3 Ni-Sn

The Ni-Sn phase diagram has been investigated repeatedly. It is a very complex system with several invariant reactions and different high- and low-temperature phases. A detailed description of the binary system was published by Nash and Nash [56], which moreover forms the basis of the phase diagram version printed in Massalski [18] (see Fig. 2.5).

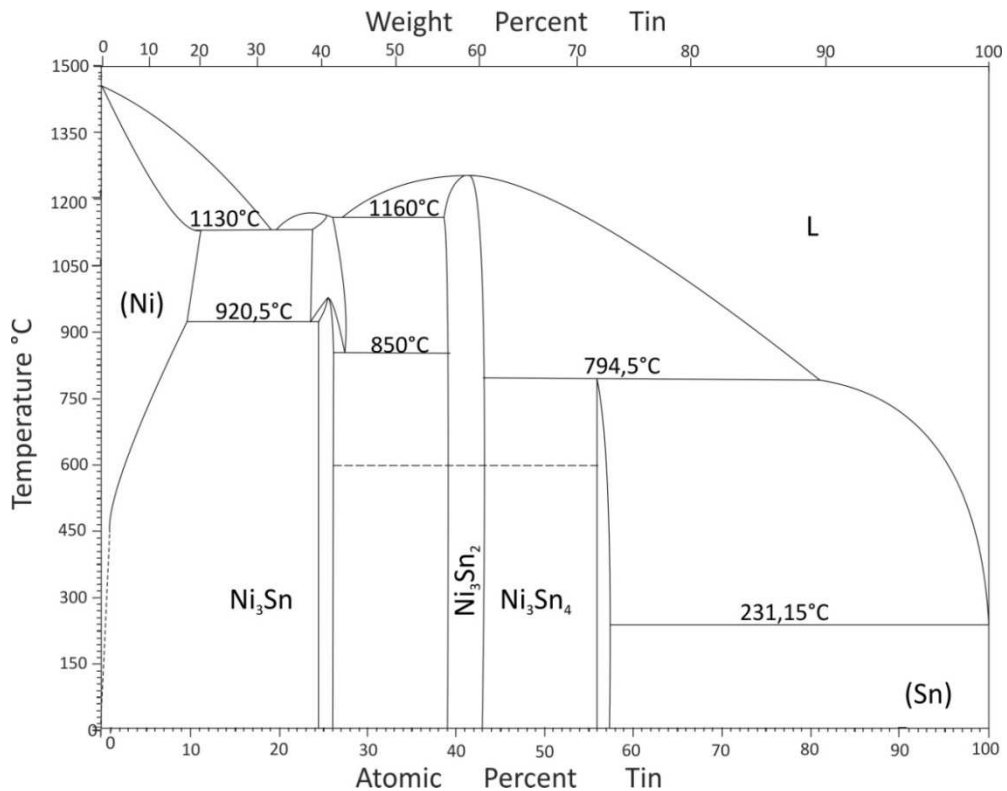


Fig. 2.5 Ni-Sn phase diagram according to Massalski [18] (based on Nash and Nash [56])

After these previous assessments new investigations of the binary system were carried out. The most recent experimental work was done by Schmetterer et al. [57] who reinvestigated the system by means of XRD, DTA and EPMA. Their version of the phase diagram differs considerably from the experimental work of Nash and Nash [56] as well as from two calculated versions published by Gosh [58] and Liu et al. [59].

A number of changes were reported in the phase diagram, a good overview of all relevant improvements and differences in the course of time, can be found in the publication of Schmetterer et al. [57].

Based on their experimental results Schmetterer et al. [57] suggested a much smaller homogeneity range of the LT structure of Ni₃Sn than in the work by Massalski

[18], whereas the homogeneity range of the HT modification widens with increasing temperature. Furthermore they reported a cubic BiF_3 structure type for the Ni_3Sn HT phase which is in agreement with an earlier work of Schubert et al. [60]. The orthorhombic structure of Ni_3Sn was confirmed to be metastable, formed at high quenching rates in a martensitic reaction.

The area around the phase Ni_3Sn_2 has been modified extremely. Whereas in the work of Massalski [18] only one modification of the low temperature phase Ni_3Sn_2 is present besides the Ni_3Sn_2 HT phase, Schmetterer et al. [57] found three phase modifications below a temperature of 508 °C. These three orthorhombic LT structures were analyzed by Leineweber et al. [61-64] but two of them have incommensurate structures (LT' and LT''). Phase transition temperatures between the Ni_3Sn_2 LT-phases and the corresponding HT phase are found to be at lower values (295 °C and 508 °C). which he concluded to be in good agreement with the evaluations of Mikulas et al. [65].

Moreover the homogeneity range of the structure Ni_3Sn_4 was shifted to higher contents of Sn (53-57 at%). Fig. 2.6 shows the current version of the Ni-Sn phase diagram according to Schmetterer et al. [57].

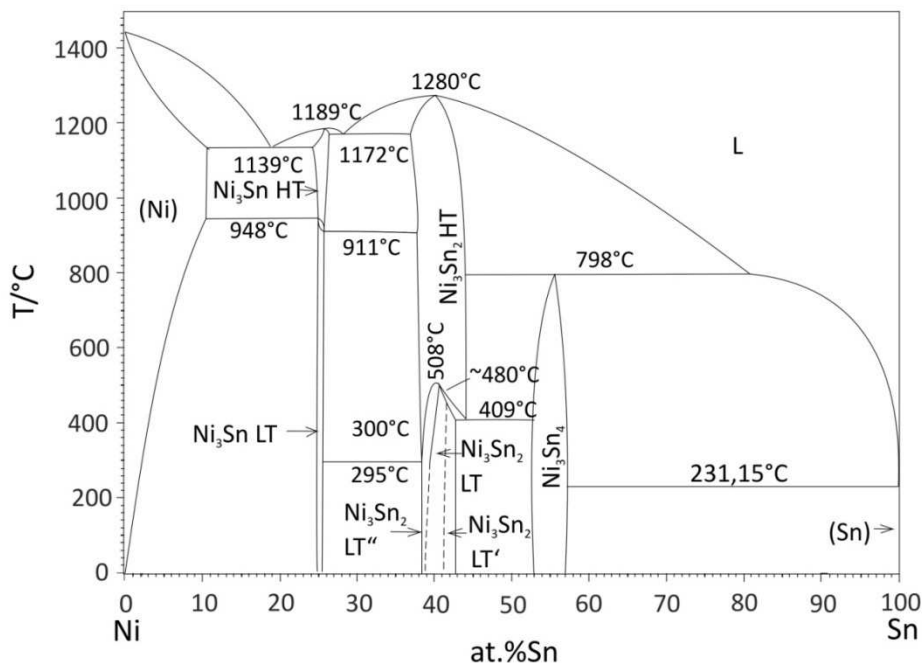


Fig. 2.6 Ni-Sn phase diagram according to Schmetterer et al. [57]

Relevant crystal structure information is given in Tab. 2.4, whereas in Tab. 2.5 the invariant reactions of the system are listed.

Tab. 2.4 Ni-Sn crystal structure data according to Schmetterer et al.[57]

Phase	Composition maximum range at% Sn	Pearson symbol	Space group	Strukturbericht	Proto-type
(Ni)	0-10.7	<i>cF4</i>	<i>Fm$\bar{3}m$</i>	A1	Cu
Ni ₃ Sn HT	24.1-26.3	<i>cF16</i>	<i>Fm$\bar{3}m$</i>	D0 ₃	BiF ₃
Ni ₃ Sn LT	24.8-25.5	<i>hP8</i>	<i>P6₃/mmc</i>	D0 ₁₉	Ni ₃ Sn
Ni ₃ Sn ₂ HT	36.7-44.0	<i>hP6</i>	<i>P6₃/mmc</i>	-	InNi ₂
Ni ₃ Sn ₂ LT''	~38.3- ~39	-	<i>Cmcm</i>	-	-
Ni ₃ Sn ₂ LT	39.3-43.1	<i>oP20</i>	<i>Pnma</i>	B1	Ni ₃ Sn ₂
Ni ₃ Sn ₂ LT'	41.25-44.0	-	<i>Cmcm</i>	-	-
Ni ₃ Sn ₄	53.0-57.0	<i>mC14</i>	<i>C2/m</i>	-	Ni ₃ Sn ₄
(β Sn)	~100	<i>tI4</i>	<i>I4₁/amd</i>	A5	β Sn
(α Sn)	~100	<i>cF8</i>	<i>Fd$\bar{3}m$</i>	A4	C _{diamond}
Metastable phases					
Ni ₃ Sn martensite		<i>oP8</i>	<i>Pmmn</i>	D0 _{α}	β Cu ₃ Ti

Tab. 2.5 Invariant reactions in the system Ni-Sn according to Schmetterer et al. [57]

Reaction	Temperature [°C]	Reaction type
$L \rightleftharpoons (Ni) + Ni_3Sn \text{ HT}$	1139	Eutectic
$Ni_3Sn \text{ HT} + (Ni) \rightleftharpoons Ni_3Sn \text{ LT}$	948	Peritectoid
$L \rightleftharpoons Ni_3Sn \text{ HT}$	1189	Congruent
$L \rightleftharpoons Ni_3Sn \text{ HT} + Ni_3Sn_2 \text{ HT}$	1172	Eutectic
$Ni_3Sn \text{ HT} \rightleftharpoons Ni_3Sn \text{ LT} + Ni_3Sn_2 \text{ HT}$	911	Eutectoid
$Ni_3Sn_2 \text{ HT} \rightleftharpoons Ni_3Sn_2 \text{ LT}'' + Ni_3Sn \text{ LT}$	295	Eutectoid
$Ni_3Sn_2 \text{ HT} + Ni_3Sn_2 \text{ LT} \rightleftharpoons Ni_3Sn_2 \text{ LT}''$	300	Peritectoid
$L \rightleftharpoons Ni_3Sn_2 \text{ HT}$	1280	Congruent
$Ni_3Sn_2 \text{ HT} \rightleftharpoons Ni_3Sn_2 \text{ LT}$	508	Congruent
$Ni_3Sn_2 \text{ HT} + Ni_3Sn_2 \text{ LT} \rightleftharpoons Ni_3Sn_2 \text{ LT}'$	~480	Peritectoid
$Ni_3Sn_2 \text{ HT} \rightleftharpoons Ni_3Sn_2 \text{ LT}' + Ni_3Sn_4$	409	Eutectoid
$Ni_3Sn_2 \text{ HT} + L \rightleftharpoons Ni_3Sn_4$	798	Peritectic
$L \rightleftharpoons (Sn) + Ni_3Sn_4$	231.15	Eutectic

2.3 Ternary System Ni-P-Sn

For the ternary system Ni-P-Sn very little information is given in literature, most of it concentrates on the ternary compounds and their crystallographic data. The only information that is available about the phase equilibria in the system is given in the publication of Schmetterer et al. [66], who created three isothermal sections at the Ni-rich corner at 550 °C, 700 °C and 850 °C.

Until now five different ternary compounds have been investigated in the system: $\text{Ni}_{10}\text{P}_3\text{Sn}$ (T1), $\text{Ni}_{21}\text{P}_6\text{Sn}_2$ (T2), $\text{Ni}_{10}\text{P}_3\text{Sn}_5$ (T3), $\text{Ni}_{13}\text{P}_3\text{Sn}_8$ (T4) and Ni_2PSn (T5). An overview of the relevant information on these ternary compounds is given in Tab. 2.6.

$\text{Ni}_{10}\text{P}_3\text{Sn}$ (T1) is a line compound with the stoichiometric composition of $\text{Ni}_{71.4}\text{P}_{21.4}\text{Sn}_{7.2}$ and was first described by Keimes [67]. Schmetterer et al. [66] confirmed the structure but suggested a different melting point at ~ 1010 °C. The compound $\text{Ni}_{21}\text{P}_6\text{Sn}_2$ (T2) is a neighboring phase of T1, it differs by only 1 at% in the Ni:P ratio. The crystal structure was described by Schmetterer et al. [68]. It is an ordered ternary version of the C_6Cr_{23} type. It is again a line compound with the melting point at 991 °C.

The other ternary phases $\text{Ni}_{10}\text{P}_3\text{Sn}_5$ (T3) and $\text{Ni}_{13}\text{P}_3\text{Sn}_8$ (T4) are reported to have similarities to the NiAs structure type, their crystal structures were identified by García-García et al. [69, 70]. They claimed that the two compounds are triclinic superstructures of the InNi_2 structure of Ni_3Sn_2 HT. Also according to Furuseth and Fjellvaag [71] T3 and T4 are formed by cooling out of the solid solution of the high temperature phase of Ni_3Sn_2 . They investigated this ternary solid solution by the disappearing phase principle as well as by determining the unit cell dimensions, and suggested the general formula $\text{Ni}_m\text{P}_x\text{Sn}_{1-x}$ ($0.00 \leq m \leq 0.65$, $0.00 \leq x \leq 0.32$) with an P-rich limit of about 17 at%. Schmetterer et al. [66] investigated the solid solution at 850 °C and affirmed the value for the maximum P content (17.6 at%) in the solid solution, though they proposed a different shape for the homogeneity range. Furuseth and Fjellvaag [71] suggested a U-like shape which was not confirmed by Schmetterer et al. [66]. At 550 °C they found out, that the maximum solubility of P in the binary solid solution is reduced to 3.3 at%. Between 850 and 700 °C the two compounds T3 and T4 develop out of the solid solution.

The ternary phase Ni₂PSn (T5) was first reported by Furuseh and Fjellvaag [72], it has a structure corresponding to the MnP-structure type with ordered Sn and P atoms. The authors claimed that this compound is a line compound whereas Schmetterer et al. [66] reported a homogeneity range of about 1 at% in all directions from EPMA measurements. The melting point of T5 was determined at 721 °C by the authors [72], where the phase decomposes according to the reaction L+Ni₂P=T5. However Schmetterer et al. [66] considered this reaction as only tentative due to some inconsistency in their DTA measurements for samples at 700 °C.

Other structures were mentioned in literature. Xia et al. [73] claimed the existence of a metastable form of the T5 phase with a tetragonal structure type which transform into the orthorhombic structure Ni₂PSn at 700 °C. They synthesized the phase by ball milling the Ni₂PSn powder. Furthermore, the phase Ni₃PSn is repeatedly named in some papers discussing lead-free solder joints and IMCs (Jee et al. [74], Sohn et al. [15], Hwan et al. [75]). The latter ones described the structure of this phase as NiAs or InNi₂-type structure type but did not give a reference. Thus, Schmetterer et al. [66] questioned the existence of the phase because in the above mentioned solder-joint papers [59-61] no exact composition was mentioned.

Tab. 2.6 the ternary Ni-P-Sn phases according to Schmetterer et al. [66]

Ternary compound	Space group	Maximum stability Temperature [°C]	composition
Ni ₁₀ P ₃ Sn (T1)	P3m1	~1010 (congruent)	Ni _{71.4} P _{21.4} Sn _{7.2}
Ni ₂₁ P ₆ Sn ₂ (T2)	Fm3m	991 (congruent)	Ni _{72.4} P _{20.7} Sn _{6.9}
Ni ₁₀ P ₃ Sn ₅ (T3)	P1	~800	Ni _{54.2} P _{16.6} Sn _{29.2} - Ni _{57.9} P _{15.3} Sn _{28.8} ^{a)} Ni ₅₄ P _{16.7} Sn _{29.3} - Ni _{56.2} P _{15.8} Sn _{28.0} ^{b)}
Ni ₁₃ P ₃ Sn ₈ (T4)	P1	700-800	Ni _{54.2} P _{11.8} Sn ₃₄ - Ni _{58.2} P ₁₁ Sn _{30.8} ^{a)} Ni ₅₄ P _{13.5} Sn _{32.5} ^{b)}
Ni ₂ PSn (T5)	Pnma	721 (peritectic)	Ni _{48.7} P _{25.3} Sn ₂₆ - Ni ₄₉ P _{24.5} Sn _{26.5}
Ni ₃ Sn ₂ HT	P63/mmc	-	Limiting ternary composition.: Ni _{52.9} P _{17.6} Sn _{29.5}

^{a)} 550 °C

^{b)} 700 °C

Schmetterer et al. [66] were the first who tried to investigate the phase equilibria in the system Ni-P-Sn. They were able to estimate three isothermal sections of the phase diagram in the Ni-rich corner of the system. They prepared samples up to a

maximum P content of 40 at% because above this limit the evaporation of P becomes severe again due to the high vapor pressure. The samples were investigated by means of XRD, EPMA and SEM. Although they reported experimental difficulties, like sample explosions and nonequilibrium samples, from these results the authors were able to create three partial thermal sections at 500 °C (shown in Fig. 2.7), 700 °C and 850 °C. They also did thermal analysis by DTA and could identify several invariant reactions in the Ni-rich corner [76].

No information in the Sn-rich and in the P-rich section of the phase diagram is available in literature, most likely because of the problems during sample preparation due to the high vapor pressure of P and the lack of information of the binary boundary system Sn-P.

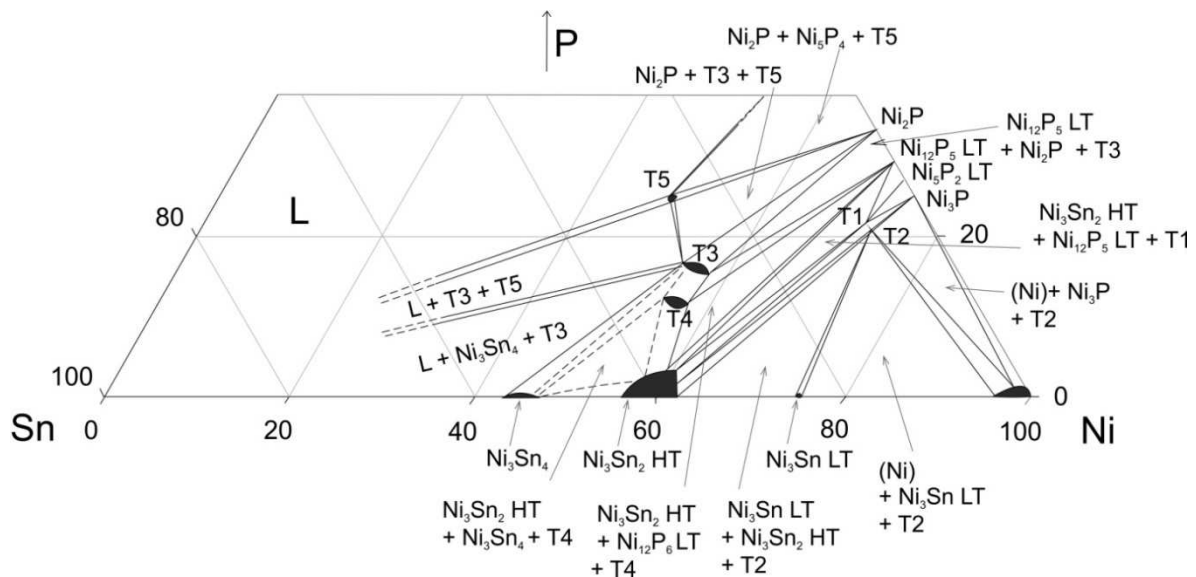


Fig. 2.7 Partial isothermal section of the ternary system Ni-P-Sn at 550°C according to Schmetterer et al. [66]

3 Applied Methods

3.1 Isopiestic method

Already at the beginning of the 20th century the isopiestic method was introduced by several authors (Bousfield and Bousfield [77], Sinclair [78] e.g.). It was used isothermally to observe and compare the vapor pressure of aqueous solutions. In the course of time a non isothermal method was developed (Stokes [79]) and was then used to investigate binary metallic systems (Herasymenko [80], Rayson and Alexander [81]). The equilibration technique and its historical development was described in detail by Ipser et al. [82].

The general principle of the isopiestic method is that a certain number of samples S_x in a temperature gradient react with the vapor of a pure volatile substance V kept at a reservoir temperature T_R in a closed system. The volatile element is maintained at constant pressure by keeping it at constant temperature at the low-temperature end of the reaction vessel. That means the temperature of the reservoir has to be the minimum temperature of the system. The component S may be a pure substance or a master alloy of S and V , $S_{1-x}V_x$. The vapor pressure of S should be at least three orders of magnitude lower than the vapor pressure of V and can therefore be neglected. So the pressure of the system is only defined by the vapor pressure of the volatile component V .

The sample S_x at the sample temperature T_{Sx} is equilibrated with the vapor of V and an alloy containing both components is formed. The increase of V in the sample stops when the equilibrium with the vapor is reached, i.e. the partial pressure of V over the sample at T_{Sx} is equal to the vapor pressure at T_R according to

$$p_V(T_S) = p_V^0(T_R) \quad \text{Eq.3.1}$$

According to that the thermodynamic activity can be calculated by

$$a_V(T_S) = \frac{p_V(T_S)}{p_V^0(T_S)} = \frac{p_V^0(T_R)}{p_V^0(T_S)} \quad \text{Eq.3.2}$$

The vapor pressure of V only depends on the reservoir temperature T_R and is constant in the whole system and independent of the temperature gradient. The only

requirement is the knowledge of the change of the vapor pressure of V as a function of the temperature. The method can be used over a pressure range from 10^{-10} to 10^{-1} bar.

Evaluation of the samples and their actual composition after the experiment can be carried out by chemical analysis or, more simply, by detecting the weight change.

The method is limited by several statistical errors, like inaccuracies during the temperature measurement or systematic errors, like incomplete equilibration or unexpected side reactions. These possible errors are described in detail by Ipser et al. [82].

3.2 X-ray powder diffraction (XRD) [83, 84]

X-ray powder diffraction is one of the most efficient analytical characterization techniques employed to identify phases that are present in crystalline materials and can be further used for determination of structural properties such as grain size, lattice parameters, epitaxy, phase composition and preferred orientation.

3.2.1 Formation of X-rays

X-rays are electromagnetic radiation with energies of about 200 eV to 1 MeV and are produced in an X-ray tube. An X-ray tube (see Fig. 3.1) consists of a vacuum chamber with a cathode emitter and a target anode inside. The cathode emitter, also called electron gun, is a piece of tungsten that is heated in order to generate electrons. The electrons are liberated by thermionic emission and are accelerated in an electric field between (20-60kV) towards the target material. The target is typically layered by metals like Cu, Co, Mo or Fe.

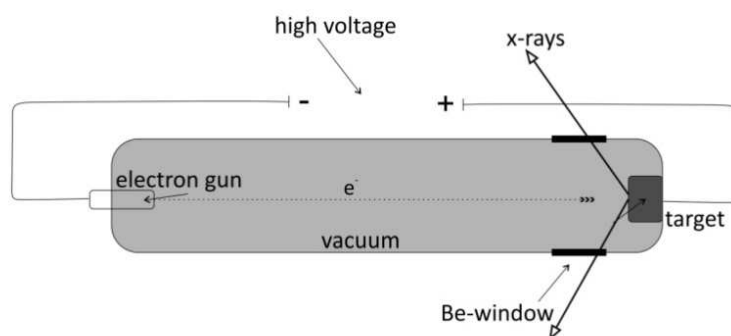


Fig. 3.1 Schematic illustration of an X-ray tube

The high-speed electrons collide with the target and rapidly lose their kinetic energy. Only a very small percentage ($\sim 1\%$) of the kinetic energy of the electrons is converted into X-rays, the major part is transformed into heat. There are two X-ray producing interactions between the incident electrons and the target atoms. In the first a continuous spectrum, called Bremsstrahlung or white radiation, is obtained. The electrons lose their energy by a series of collisions with the target atoms which results in a direct emission of X-rays from the electron. The second interaction happens when the incoming electron ejects electrons from an inner orbital of the target atoms. An electron from an outer orbital is transferred to occupy the inner shell vacancy and an X-ray quantum with characteristic wavelength is emitted. The energy of the X-ray corresponds to the energy loss of the electron. Each metal gives a characteristic X-ray spectrum, the spectrum of Cu as an anode is schematically shown in Fig. 3.2.

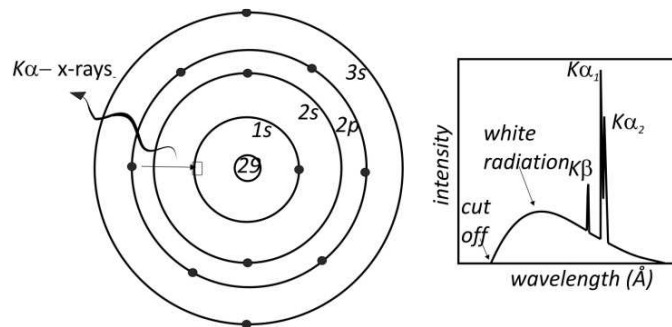


Fig. 3.2 The element Cu (a) the process of emission of characteristic $K\alpha$ X-rays and (b) its X-ray spectrum [83]

The X-rays are then directed onto the sample.

3.2.1 Diffraction of X-rays, powder diffraction

When X-rays are scattered at a crystalline solid they can interfere constructively, producing a diffracted beam. A crystal can be seen as a grating that consists of atomic layers (with the distance d) where diffraction can occur. The wavelength of the X-rays is of the same magnitude as the interatomic distances in the crystal ($\sim 0.2\text{nm}$). The parallel layers are identified by Miller indices (h, k, l). The atoms of each atomic plan form scattering centers, where the incident X-rays are diffracted. The interaction of the incident beams with the sample produces constructive interference when the path length difference is an integer number of the wavelength. The diffracted waves

from different atomic layers produce a certain diffraction pattern, which contains information about the atomic arrangement within the crystal.

The theoretical model to explain the principle of diffraction was described by Bragg. Bragg's law, expressed in Eq.3.3, defines the general relationship between the wavelength of the incident X-rays, angle of incidence and the distance between the layers of atoms. A graphical expression of Bragg's law is shown in Fig. 3.3 .

$$2d_{hkl} * \sin\theta = n\lambda \quad \text{Eq.3.3}$$

where d is the distance between the atomic layers (hkl) in the crystal, n is an integer, θ is the angle and λ is the wavelength of the incident X-ray beam.

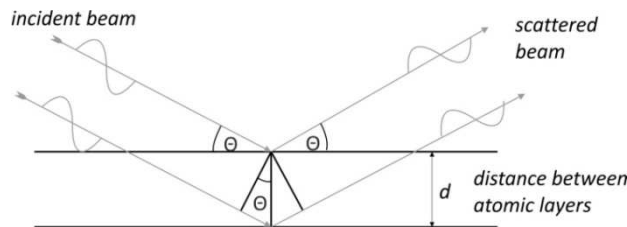


Fig. 3.3 Diffraction according to Bragg's law

The intensities of the diffraction are connected to the atoms in the unit cell by the so called structure factor F according to Eq.3.4 or better with additional correction factors like in Eq.3.5

$$I_{hkl} \propto |F_{hkl}|^2 \quad \text{Eq.3.4}$$

$$I_{hkl} = |F_{hkl}|^2 \cdot H \cdot LP \cdot A \quad \text{Eq.3.5}$$

- F_{hkl} : Structure factor
- H: Multiplicity factor
- LP: Lorentz polarization factor
- A: Absorption factor

The structure factor F carries the structural information according to

$$F_{hkl} = \sum_i f_i \cdot e^{-2\pi i(hx_i + ky_i + lz_i)} \quad \text{Eq.3.6}$$

Where f_i is the scattering or form factor of the atom i . It is the scattering power of a atom as a function of the angle and the wavelength and it also depends on the number of electrons in the atom. It is easier to distinguish between atoms with a higher difference in the electron number. It is also modified by the temperature factor which considers the thermal movement of the electrons.

$$f_i(T) = f_i e^{\frac{-B \sin^2 \theta}{\lambda^2}} \quad \text{Eq.3.7}$$

where B is the temperature factor.

3.2.2 Instrumental setup

The generated X-rays (e.g. Cu-K α_1 , K α_2 , K β) exit the X-ray tube and pass several slits (collimators) in order to provide a linear beam. They are incident on the powdered sample from which they are diffracted into the detector, which can be a strip detector, scintillation counter or an energy dispersive solid state detector. Before the beam reaches the detector it passes through a Ni-filter, in order to remove the K β energy.

Two different geometries can be used during the diffraction measurement in order to focus the divergent X-ray beam; they are called Bragg-Brentano pseudo focusing geometries. There is the $\Theta/2\Theta$ -geometry, which means that the specimen holder and the detector are moving simultaneously. When the specimen holder moves Θ , the detector moves an angle of 2Θ . This arrangement is different to the Θ/Θ -geometry where the source and the detector move on the circle, the sample holder is fixed in the center of the circle.

A XRD-pattern is the result of the diffraction measurement; it is a two dimensional plot of the angle Θ on the x-coordinate against the intensity. The relevant information of the pattern are the diffraction lines, which depend on the lattice parameters and the symmetry, and the intensities, from which the multiplicities and the site occupation can be seen.

3.2.3 Rietveld refinement [83]

The Rietveld refinement is a mathematical method to calculate a theoretical pattern that can describe the measured pattern in order to identify the phases. With this evaluation it is possible to determine the exact structural parameters of the sample such as atomic positions or lattice parameters.

The theoretical pattern is calculated regarding the instrument-related parameters and using a proper starting model including expected structural data which is obtained from databases such as [35].

The refinement is based on the principle of approaching the calculated pattern to the measured one with a least-square-fit algorithm.

$$\chi_1^2 = \frac{\sum_i w_i (y_{oi} - y_{ci})^2}{\sum_i w_i y_{oi}} \quad \text{Eq.3.8}$$

where y_{oi} is the observed and y_{ci} is the calculated intensity at the point i , w_i is the weighting factor that considers that reflected data points carry a higher weight than background points. To calculate the theoretical intensities y_{ci} the following equation is used.

$$y_{ci} = y_{Bi} + S \cdot \sum_{hkl} |F_{hkl}|^2 \cdot p \cdot \left(\frac{1 + \cos^2 2\theta_i}{\sin^2 \theta_i \cos \theta_i} \right) \cdot e^{-\frac{2B \sin^2 \theta}{\lambda^2}} \cdot \phi(2\theta_i - 2\theta_{hkl}) \cdot P_{hkl} \cdot A \cdot S_r \cdot E \quad \text{Eq.3.9}$$

- y_{Bi} : Background at i
- S : Scaling factor (for each phase)
- p : multiplicity factor
- Φ : Profile function
- P_{hkl} : Factor of preferred orientation
- A : Absorption factor
- S_r : Function of surface roughness
- E : Extinction factor

The reliability values or so called R_{wp} -value show the accordance between the measured and the calculated pattern and are hence a criterion for the quality of the refinement, a value below 10 is acceptable. It is calculated according to

$$R_{wp} = \sqrt{\frac{\sum_i w_i |y_{oi} - y_{ci}|^2}{\sum_i w_i y_{oi}^2}} \quad \text{Eq.3.10}$$

3.3 Light optical microscopy (LOM) [83, 85]

The principle of light optical microscopy (LOM) is to shine light through a specimen (transmitted light) or on the surface of a specimen (reflected light) to analyze it under magnification. The main operating components of the microscope are the objective lens, the ocular, the condenser, and the light source. The objective lens magnifies the object, the ocular simply enlarges the image but does not increase the resolution and the condenser focus the light beam to minimize the stray light. The magnification M of a microscope is given by

$$M_{total} = M_{objective} + M_{ocular} \quad \text{Eq.3.11}$$

Another important factor is the resolution of a microscope, which is the ability to distinguish between two points on an image. The resolution limit d_0 was described by Abbe.

$$d_0 = \frac{\lambda}{2NA} \quad \text{Eq.3.12}$$

So the resolution depends on the wavelength λ of the incident light beam, and the so call numerical aperture NA, which is the ability of the lens to gather and focus light according to

$$NA = n * \sin\alpha \quad \text{Eq.3.13}$$

where n is the refraction index of the medium and α is one half of the opening angle of the objective.

Different imaging modes can be used to analyze the sample with the LOM.

- Bright field: It is a direct imaging mode and the most conventional method for the determination of microstructures. It is used to observe primary crystallization and it is possible to get an idea of the average grain size. Phases can be distinguished due to reflectivity, color or roughness differences.
- Dark field: This method is used to control the quality of the polishing of the sample. The primary beam is deviated with the help of a mirror system and the light irradiates the sample at a very low angle. Flat surfaces seem black because the reflected beam does not strike the ocular, uneven areas are bright. Scratches, rough surfaces, holes and also grain boundaries can be seen.
- Polarization mode: After passing a polarizer the linear polarized light hits the sample and the polarization plane is modified according to the optical properties of the sample. The reflected beam hits an analyzer, where only the depolarized light is able to pass, and contrast is detected in this way.
- Differential interference contrast (DIC): With this mode it is possible to visualize height differences in the surface. It is an extension to the polarization mode, the polarized beam is separated by a bi-refringent prism into two parts. After being

reflected by the sample the two beams interfere, the path difference can be seen as elevation difference.

Analysis with these modes can give an overview about the phase ratio in the sample, as well as grain size and the crystallization sequence.

3.4 Scanning electron microscopy (SEM) [83, 86]

A scanning electron microscope (SEM) is a microscope that uses high energy electrons to investigate samples on a very fine scale with a magnification of about 500 times larger than in optical microscopy and a resolution down to several nm.

The signals that derive from electron-sample interactions reveal information about the sample including external morphology (texture), topography, composition, phases and crystallographic information.

The electron beam is generated in a high vacuum column by an electron gun which is a sharp tungsten filament or a LaB₆ tip. The electrons are emitted by the cathode and are then accelerated at a voltage of 15-40 kV towards an anode. Electromagnetic lenses are used to focus the electron beam to a size of less than 1 μm. This focused beam is then applied to scan the surface of a sample. Scanning coils are used for moving the beam over the sample. The analyzed specimen has to be conductive or has to be coated with a conductive material. A schematic illustration of a scanning electron microscope is shown in Fig. 3.4.

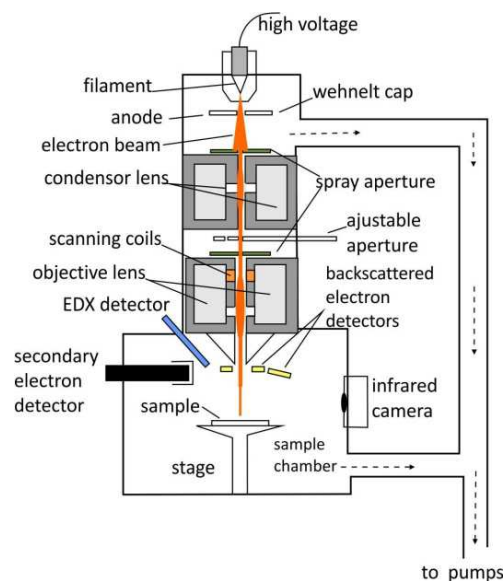


Fig. 3.4 Schematic illustration of an SEM according to [87]

Electrons that are accelerated onto a specimen result in a number of interactions with the atoms of the target material. They can pass through the sample without interaction, undergo elastic scattering and can be inelastically scattered. The following effects occur during the electron-sample interaction (see Fig. 3.5):

- Secondary electrons
- Backscattered electrons
- Characteristic X-rays
- Absorbed electrons
- Auger electrons
- Fluorescence X-rays

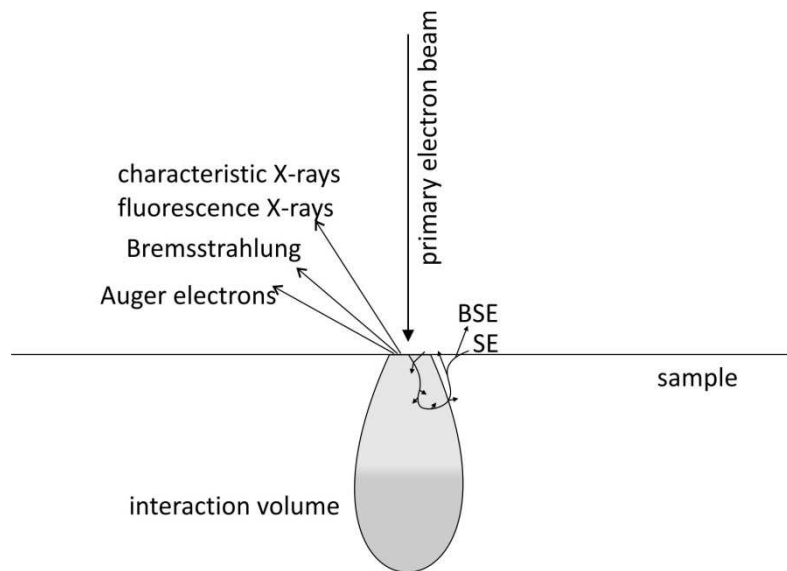


Fig. 3.5 Interaction of the primary electrons with the sample

Secondary electrons and backscattered electrons are typically used for imaging the sample. Secondary electrons are low energy electrons and are most valuable for showing morphology and topography on the sample.

Backscattered electrons are reflected high energy electrons and are useful for illustrating contrasts in composition in multiphase samples. The contrast is induced due to the difference in the atomic number; heavier atoms reflect the electrons more than light atoms.

Characteristic X-rays are generated by inelastic collision of the incident electron beam with electrons in discrete orbitals of the atoms in the sample. The X-rays are used for qualitative and semi-quantitative analysis of the material and can be

detected either by electron-dispersive X-ray spectroscopy (EDX) or wavelength dispersive X-ray spectroscopy (WDX).

With EDX the characteristic X-rays of different elements can be separated and transformed into an energy spectrum, which is used to find the chemical composition of a sample as well as to create element composition maps.

The WDX-detector system uses an oriented monochromator crystal that only allows diffraction X-rays of desired wavelengths into the detector. Different crystals are used for different wavelength ranges. This provides a better resolution and a high quality analysis but needs excessively more time. Due to its high resolution the detector can also be used for quantitative analysis. To get quantitative reliable results it is necessary to employ ZAF matrix correction.

4 Experimental

4.1 The binary system Sn-P

4.1.1 Preparation of samples, Isopiestic method

The method used to investigate the binary system Sn-P is based on isopiestic measurements. The principle of this method is described in section 3.1. The individual alloys in the tube are in equilibrium with the gas phase and the corresponding sample reflects exactly this equilibrium. The setup used in this work slightly differed from the classical assembly illustrated in literature [27, 82, 88]. The experiment was carried out in much smaller dimensions with tubes of 300-400 mm length and the tube is placed horizontally in a two-zone furnace (see Fig. 4.1). This small-scale experiment was already described by Schmetterer et al. [28]. The purpose is to create a temperature gradient inside the furnace chamber by setting two different temperatures in the front and in the back of the furnace. The exact temperature gradient was measured with an external thermocouple Type K (NiCr/Ni) at least twice for each run.



Fig. 4.1 a) Two- zone furnaces with control units
b) Furnace chamber

The schematic illustration of the experimental setup is shown in Fig. 4.2.

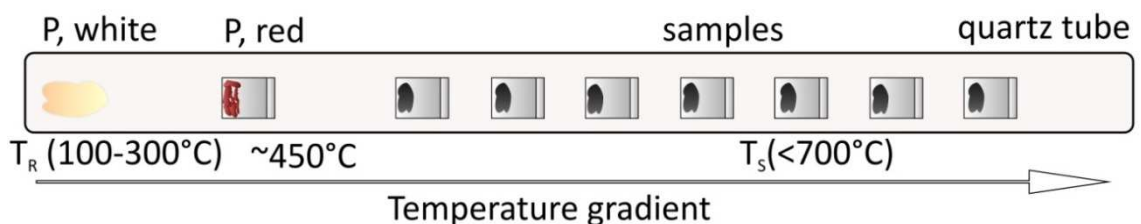


Fig. 4.2 Schematic of mini-isopiestic experimental setup

The assembly consisted of an outer quartz glass tube with 15 or 16 mm O.D. and a wall thickness of 2mm in order to resist the vapor pressure that develops during the experiments. The starting materials were tin pieces (Alfa Aesar, Germany; 99.999 % metallic purity) and lumps of red phosphorus (Alfa Aesar, Germany; Puratronic, 99.999 % metallic purity). Approximately 50-100 mg of the pure Sn were placed in high-purity graphite crucibles with 10 mm O.D. (see Fig. 4.3). Between 4 and 12 of these crucibles were stacked inside the quartz tube.



Fig. 4.3 graphite crucible

Additionally 1 or 2 graphite holders filled with excess amounts of red phosphorus were placed in the tube at a temperature of about 450 °C. The red phosphorus evaporated and recondensed as white phosphorus at the reservoir which was the coolest point of the quartz tube. This temperature defined the vapor pressure of P in the tube. The fully assembled equipment (shown in Fig. 4.4) was repeatedly evacuated and refilled with Ar and then sealed under a dynamic vacuum of minimum 10^{-3} bar.

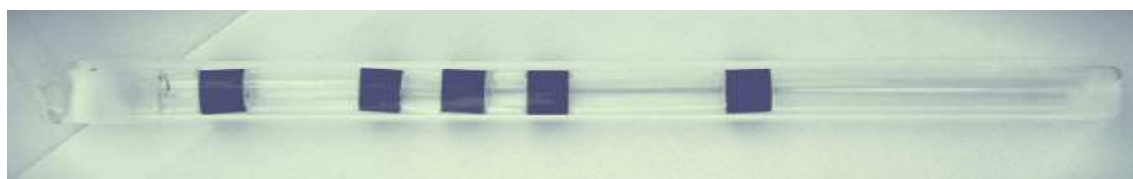


Fig. 4.4 Sealed tube before experiment;
Graphite crucibles with Sn and P, respectively; in between spacers made of quartz glass

The experimental unit was inserted into the furnace chamber and heated for at least 4 days. The temperature of the reservoir (T_R) and the individual sample temperatures were recorded at the beginning and at the end of each run to be sure the temperature gradient is stable. At the end of each run the quartz tube was quenched in cold water, the hotter part of the tube got immersed into the water

first, so that the pressure fixed from the P reservoir would be maintained as long as possible in the tube.

The quartz glass (shown in Fig. 4.5a) was opened under an extractor hood with a diamond saw. All the glass parts contaminated with white phosphorus (see Fig. 4.5b) were placed in a CuSO_4 solution. There the toxic white phosphorus reacted to Cu_3P .

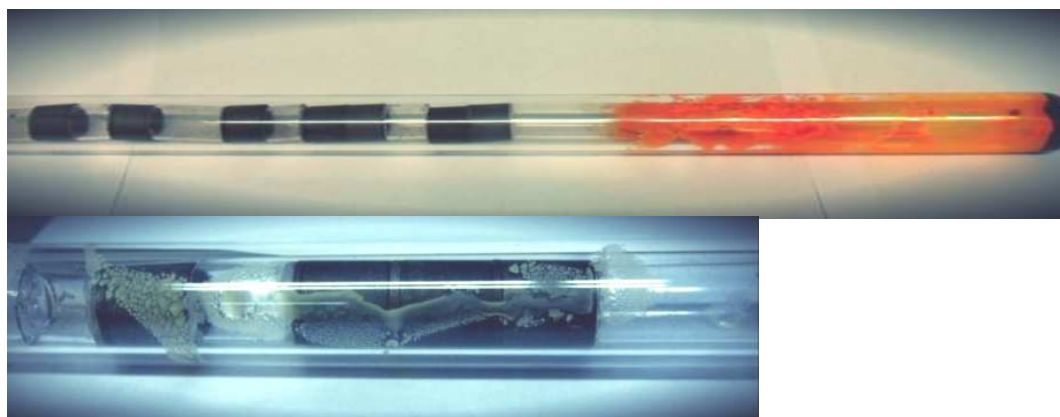


Fig. 4.5 a) Quartz glass tube after the experiment, mixture of red and white phosphorus (reddish-yellow color) b) White phosphorus condensed on the inner quartz glass wall

Each sample was weighed and the mass increase was a measure for the amount of phosphorus absorbed in the sample. An overview of all performed experiments is shown in Tab. 4.1.

Tab. 4.1 Overview of all isopiestic runs in the system Sn-P

run	samples	temperature [°C/K]	pressure p [bar]	heating period [d]	used for further analysis
SnP1	4	260/533	0.70	4	
SnP2	4	259/532	0.69	4	x
SnP3	6	266/539	0.80	4	
SnP4	6	268/541	0.83	4	
SnP5	6	248/521	0.55	6	x
SnP6	6	268/541	0.83	6	
SnP7	6	259/532	0.69	4	x
SnP8	6	260/533	0.71	6	x
SnP9	6	226/499	0.33	5	x
SnP10	6	228/501	0.35	5	x
SnP11	10	279/552	1.02	4	
SnP12	10	213/486	0.24	4	x
SnP13	10	199/472	0.17	4	x
SnP14	8	199/472	0.17	4	x
SnP15	9	245/518	0.52	5	x
SnP16	10	170/443	0.07	4	x
SnP17	10	189/462	0.13	4	x
SnP18	12	170/443	0.07	8	x
SnP19	12	104/377	0.006	8	x

4.1.2 XRD

Characterization of representative samples was obtained by means of X-ray powder diffraction (XRD). The measurements were carried out on a Bruker D8 diffractometer (Bruker AXS, Germany see Fig.4.6) in Bragg-Brentano pseudo-focusing geometry using a $\theta/2\theta$ arrangement. The diffractometer is equipped with a high speed LynxEye one dimensional silicon strip detector (LynxEye™) using Cu-K α 1 radiation with a variable slit aperture of 12 mm. The measurement period was 30 min.

To prepare the samples for the measurement a small piece of it was powdered with a tungsten carbide mortar to a size of approximately 15 μm . Before measuring the powder was placed as a thin layer on a silicon wafer using Vaseline.

The obtained powder patterns were analyzed and refined by means of the software program TOPAS 3 (provided by Bruker) applying Rietveld refinement. Starting parameters were obtained from Pearson [35].



Fig. 4.6 Bruker D8 diffractometer and measuring device

4.2 The ternary system Ni-P-Sn

4.2.1 Sample preparation

Ternary Ni-P-Sn alloys were prepared from Ni powder (99.995 %, Koch Light Laboratories, UK), P powder (red P-lump, 99.999+ %, Alfa Aesar, Germany) as well as pieces of Sn (99.999 %, Alfa Aesar, Germany). Both Ni and P were stored in the glove box, while weighing and preparation of the samples was done on air. The powder of P was made out of P-lumps by powdering it in a tungsten carbide mortar directly before weighing. Samples were weighed with a semi-micro balance with an accuracy of about ± 0.2 mg/ ± 0.1 at% with a total mass of 1200 mg and 800-1500 mg for the second run, respectively.

Some samples should have been prepared by mixing NiP_2 and the ternary phase T_5 in a proper ratio. These two components were made by annealing the pure materials at 550 °C and quenching, followed by a quality check using XRD. Unfortunately, problems occurred with the preparation of NiP_2 because of evaporation of P and due to the lack of time no new samples could be produced.

The powders were thoroughly mixed and filled in an alumina crucible. This was necessary because of problems of embrittlement of the quartz glass mentioned in literature [2, 66]. The samples were sealed in quartz glass tubes after evacuating and refilling with Ar gas several times. The sealed samples (Fig. 4.7) were heated in a muffle furnace according to the temperature program shown in Tab. 4.2



Fig. 4.7 sealed samples of Ni-P-Sn

Tab. 4.2 temperature programs for annealing at 300 and 550 °C

	temperature [°C]	heating rate [K/h]	dwll [h]
↗	400	4	-
↗	640	2	-
→	640	-	24
↗	700	1	-
→	700	-	24
↘	300	8	-
→	300	annealing	
↗	250	4	-
↗	350	2	-
→	350	-	12
↗	450	1	-
→	450	-	48
↗	550	1	-
→	550	annealing	

The heating rate was set between 1 to max. 4 K/h. This was done because samples with a high content of phosphorus already caused problems in an earlier work by Schmetterer [2]. Apart from the significant vapor pressure development of P at higher temperatures, there is also a strongly exothermic reaction between Ni and P that starts at about 550 °C and results in a sudden increase in temperature and pressure in the sample tube. This reaction can cause an explosion of the quartz glass tube. The heating program that was chosen required about 2 weeks. Isothermal segments were chosen at 350/400 °C, 450 °C (just before the sublimation of red P), 550 °C (reaction of P and Ni), and in the first run 640 and 700 °C. In spite of these settings, several samples burst inside the furnace during the temperature treatment (Fig. 4.8a), others showed an extensive evaporation of P (see Fig. 4.8b).



Fig. 4.8 samples that could not be used for analysis due to
a) Bursting in the furnace
b) Extensive evaporation of phosphorus

After annealing the samples were quenched in cold water to freeze the equilibrium state at the annealing temperature. The exact sample compositions together with the annealing periods are shown in Fig. 4.9 and summarized in Tab. 4.3.

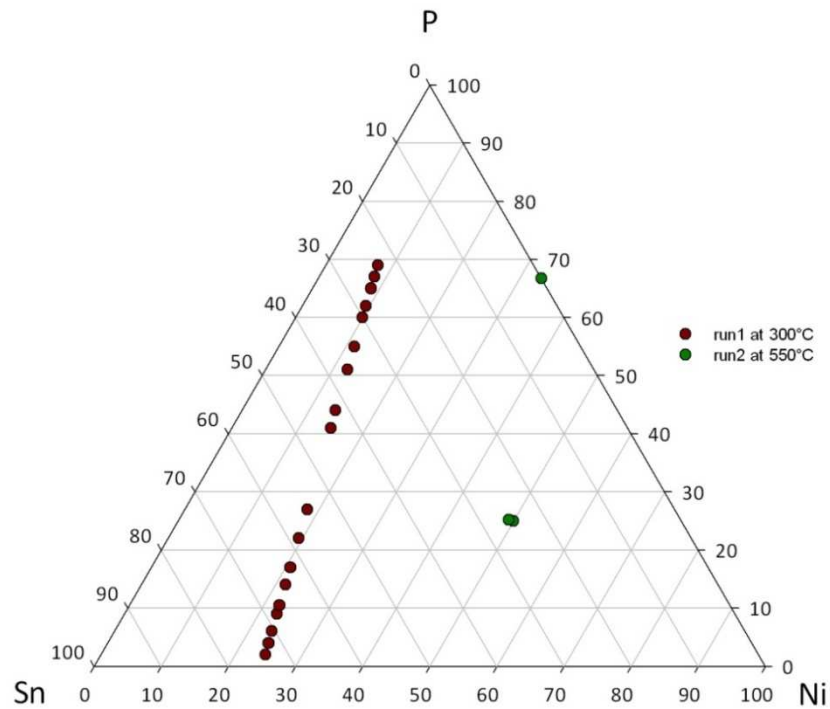


Fig. 4.9 prepared samples in the system Ni-P-Sn

Tab. 4.3 sample composition and annealing procedures

sample	nominal composition [at%]			actual composition [at%]			annealing temp [°C]	annealing duration [days]
	Ni	P	Sn	Ni	P	Sn		
NPS1	24.5	2.00	73.5	24.49	2.01	73.50	300	66
NPS2	24.00	4.00	72.00	24.00	4.01	71.99	300	66
NPS3	23.50	6.00	70.50	23.50	6.01	70.49	300	66
NPS4	22.75	9.00	68.25	22.75	8.99	68.26	300	66
NPS5	22.38	10.5	67.12	22.37	10.50	67.13	300	40
NPS6	21.50	14.00	64.50	21.50	14.01	64.49	300	66
NPS7	20.75	17.00	62.25	20.75	17.01	62.25	300	66
NPS8	19.50	22.00	58.50	19.50	22.01	58.49	300	66
NPS9	18.25	27.00	54.75	18.25	27.00	54.75	300	66
NPS10	14.75	41.00	44.25	14.75	41.01	44.24	300	66
NPS11	14.00	44.00	42.00	14.00	44.01	41.99	300	66
NPS12	12.25	51.00	36.75	12.26	51.00	36.75	300	66
NPS13	11.25	55.00	33.75	11.24	55.00	33.76	300	66
NPS14	10.00	60.00	30.00	no analysis possible ¹⁾			300	66
NPS15	9.50	62.00	28.50	no analysis possible ¹⁾			300	66
NPS16	8.75	65.00	26.25	no analysis possible ²⁾			300	66
NPS17	8.25	67.00	24.75	no analysis possible ¹⁾			300	66
NPS18	7.75	69.00	23.25	no analysis possible ²⁾			300	66

sample	nominal composition [at%]			actual composition [at%]			annealing temp [°C]	annealing duration [days]
	Ni	P	Sn	Ni	P	Sn		
NP_1	33.30	66.70	0.00	no analysis possible ¹⁾			550	25
NP_2	33.30	66.70	0.00	42.00	58.00	0.00 ²⁾	550	25
T5_1	50.00	25.00	25.00	50.30	24.55	25.15	550	25
T5_2	49.20	25.20	25.60	49.41	24.88	25.71	550	25

¹⁾ Explosion of the quartz glass sample in the furnace

²⁾ Condensation of P at the inner quartz glass wall

To prepare the annealed samples for further analysis, they were cut in three parts with a diamond saw (Buehler low speed saw). The saw blade was cooled with a special saw lubricant solvent. After cutting the sample, the pieces were cleaned with acetone in an ultrasonic bath.

4.2.2 XRD

One piece of the sample was analyzed by X-rays. As mentioned above in 4.1.2 the phase identification of the samples was obtained by X-ray powder diffraction with a Bruker D8 diffractometer (see Fig.4.6) by means of the software program TOPAS 3 (provided by Bruker). Starting parameters were obtained from Pearson [35]. The same arrangement was used as for binary Sn-P samples, only the measuring time was extended to one hour. Due to the large amount of tin the samples were quite ductile and could not be powdered in the mortar. Therefore a diamond file was used for powdering. Analysis of the samples was equal, applying Rietveld refinement.

4.2.3 Metallography

For further analysis with light optical microscopy (LOM) and scanning electron microscopy (SEM) another piece of each sample was embedded (Struers LaborPress-1) in a phenolic hot mounting resin (Struers, PolyFast, thermosetting, filler material: carbon). For this, the samples and a small amount of the resin were heated in the embedding cylinder at 180 °C under a pressure of 15 kN for 5 minutes.



Fig. 4.10 embedded samples

To obtain a flat and shiny surface the embedded samples (see Fig. 4.10) were ground with abrasive paper of different roughness and then polished with corundum powder (1 μm) (Buehler grinder/polisher Metaserv 2000).

4.2.3.1 LOM (Light Optical microscopy)

To obtain a first overview of the appearance and the microstructure of the samples they were surveyed by light optical microscopy (LOM) using a binocular reflected-light microscope (Zeiss Axiotech 100) with magnification possibility of 50, 100, 200 and 500. The imaging modes applied were bright field and dark field imaging as well as polarization optics and differential interference contrast (DIC) (for details see section 3.3).

4.2.3.2 SEM (Scanning Electron Microscopy)

To obtain data for the exact composition of the phases that are present in the sample a scanning electron microscope (Zeiss Supra 55 VP ESEM; Fig. 4.11 [89]) was used, working in the energy dispersive mode (EDX-detector). The acceleration voltage was set to 20 kV and an aperture of 120 μm was used. To minimize the statistical error and to get more reliable results each phase composition



was measured at least three times on different spots of the sample. **Fig. 4.11** Zeiss Supra 55

5 Results and discussion

5.1 Results in the system Sn-P

5.1.1 Isopiestic measurements

Successful isopiestic measurements were carried out at nine different reservoir temperatures in a pressure range from 0.006 to 0.69 bar. Sample temperatures were set between 320 and 624 °C. A list of all experimental runs as well as equilibration time is shown in Tab. 4.1 whereas in Tab.5.1 experimental conditions, sample temperatures, results and the phases present in each sample are listed.

Tab.5.1 Isopiestic experimental results

Sample No.	at%P	Ts[°C]/[K]	Phases
T_R [°C]/[K] 104/377			
p[bar] 0.0058 logp -2.2384			
SnP19_4	43.12	332/605	Sn ₄ P ₃
_5	42.80	352/625	Sn ₄ P ₃
_6	42.56	379/652	Sn ₄ P ₃
_7	43.10	404/677	Sn ₄ P ₃
_8	42.71	426/699	Sn ₄ P ₃
_9	42.91	435/708	Sn ₄ P ₃
_10	5.14	447/720	L
_11	4.71	473/746	L
_12	4.96	481/754	L
T_R [°C]/[K] 170/443			
p[bar] 0.0717 logp -1.1445			
SnP16_8	5.68	551/824	L
_9	7.88	598/871	L
_10	5.56	604/877	L
SnP18_1	45.62	302/575	Sn ₄ P ₃ +Sn ₃ P ₄ ^{*)}
_2	47.23	317/590	Sn ₄ P ₃ +Sn ₃ P ₄ ^{*)}
_3	50.43	330/603	Sn ₄ P ₃ +Sn ₃ P ₄ ^{*)}
_4	52.68	344/617	Sn ₄ P ₃ +Sn ₃ P ₄ ^{*)}
_5	53.81	361/634	Sn ₄ P ₃ +Sn ₃ P ₄ ^{*)}
_7	42.74	394/667	Sn ₄ P ₃
_8	42.49	440/713	Sn ₄ P ₃
_9	42.42	460/733	Sn ₄ P ₃
_10	10.67	488/761	L
_11	9.73	509/782	L
_12	9.77	533/806	L
T_R [°C]/[K] 189/462			
p[bar] 0.127 logp -0.8961			
SnP17_1	46.83	320/593	Sn ₄ P ₃ +Sn ₃ P ₄ ^{*)}
_2	49.32	342/615	Sn ₄ P ₃ +Sn ₃ P ₄ ^{*)}
_3	53.32	357/630	Sn ₄ P ₃ +Sn ₃ P ₄ ^{*)}
_4	55.70	390/663	Sn ₄ P ₃ +Sn ₃ P ₄ ^{*)}
_5	42.58	413/686	Sn ₄ P ₃
_6	42.53	430/703	Sn ₄ P ₃
_7	42.76	453/726	Sn ₄ P ₃
_8	8.15	496/769	L
_9	7.13	539/812	L
_10	7.12	574/847	L

Sample No.	at%P	Ts[°C]/[K]	Phases
T_R [°C]/[K] 199/472			
p[bar] 0.168 logp -0.7748			
SnP13_1	58.55	351/624	Sn ₄ P ₃ +SnP ₃
_2	56.71	383/656	Sn ₃ P ₄
_3	56.74	400/673	Sn ₃ P ₄
_4	42.69	414/687	Sn ₄ P ₃
_5	42.77	443/716	Sn ₄ P ₃
_6	42.51	464/737	Sn ₄ P ₃
_7	16.34	512/785	L
_8	11.86	560/833	L
_9	9.00	598/871	L
_10	8.74	614/887	L
SnP14_3	12.09	512/785	L
_4	7.67	538/811	L
_5	12.17	599/872	L
_6	9.05	607/880	L
_7	7.91	615/888	L
_8	9.85	624/897	L
T_R [°C]/[K] 213/486			
p[bar] 0.243 logp -0.6148			
SnP12_2	69.66	370/643	Sn ₄ P ₃ +SnP ₃
_3	42.91	409/682	Sn ₄ P ₃
_4	39.91	485/758	L+Sn ₄ P ₃
_5	13.48	515/788	L
_6	10.25	554/827	L
_7	8.70	570/843	L
_8	7.21	591/864	L
_9	7.43	606/879	L
T_R [°C]/[K] 227/500			
p[bar] 0.342 logp -0.4655			
SnP9_1	42.92	433/706	Sn ₄ P ₃
_2	15.73	510/783	L+ Sn ₄ P ₃
_3	11.83	533/806	L
_4	6.46	577/850	L
_5	5.80	602/875	L
_6	5.63	619/892	L
SnP10_1	42.59	440/713	Sn ₄ P ₃
_2	10.73	513/786	L+ Sn ₄ P ₃
_3	5.08	536/809	L
_4	6.13	572/845	L
_5	5.09	600/873	L
_6	5.41	613/886	L
T_R [°C]/[K] 245/518			
p[bar] 0.515 logp -0.2878			
SnP15_1	57.09	379/652	Sn ₃ P ₄
_2	45.34	434/707	Sn ₄ P ₃ +Sn ₃ P ₄
_3	18.62	518/791	L+Sn ₃ P ₄
_4	14.30	534/807	L
_5	9.55	550/823	L
_6	9.11	568/841	L
_7	7.34	581/854	L
_8	8.70	596/869	L
_9	7.31	603/876	L

Sample No.	at%P	Ts[°C]/[K]	Phases
T_R [°C]/[K] 248/521			
p[bar] 0.550 logp -0.2596			
SnP5_1	42.60	485/758	Sn ₄ P ₃
_2	42.47	510/783	Sn ₄ P ₃
_3	21.63	534/807	L
_4	16.61	577/850	L
_5	16.31	603/876	L
_6	12.55	617/890	L
T_R [°C]/[K] 259/532			
p[bar] 0.693 logp -0.1595			
SnP7_1	43.32	478/751	Sn ₄ P ₃
_2	39.42	510/783	L+Sn ₄ P ₃
_3	13.24	538/811	L
_4	5.76	577/850	L
_5	5.00	602/875	L
_6	5.20	613/886	L
SnP8_1	42.58	487/760	Sn ₄ P ₃
_3	10.29	537/810	L
_4	7.64	573/846	L
_5	5.86	601/874	L
_6	5.23	606/879	L

*) sample not in equilibrium

Temperature measurements during the experiments are estimated to be accurate within ±3K. A diagram of all obtained data points is shown in Fig. 5.1, different vapor pressures are labeled with different characters. This schematic Sn-P phase diagram shows the equilibrium curves for each isopiestic experiment.

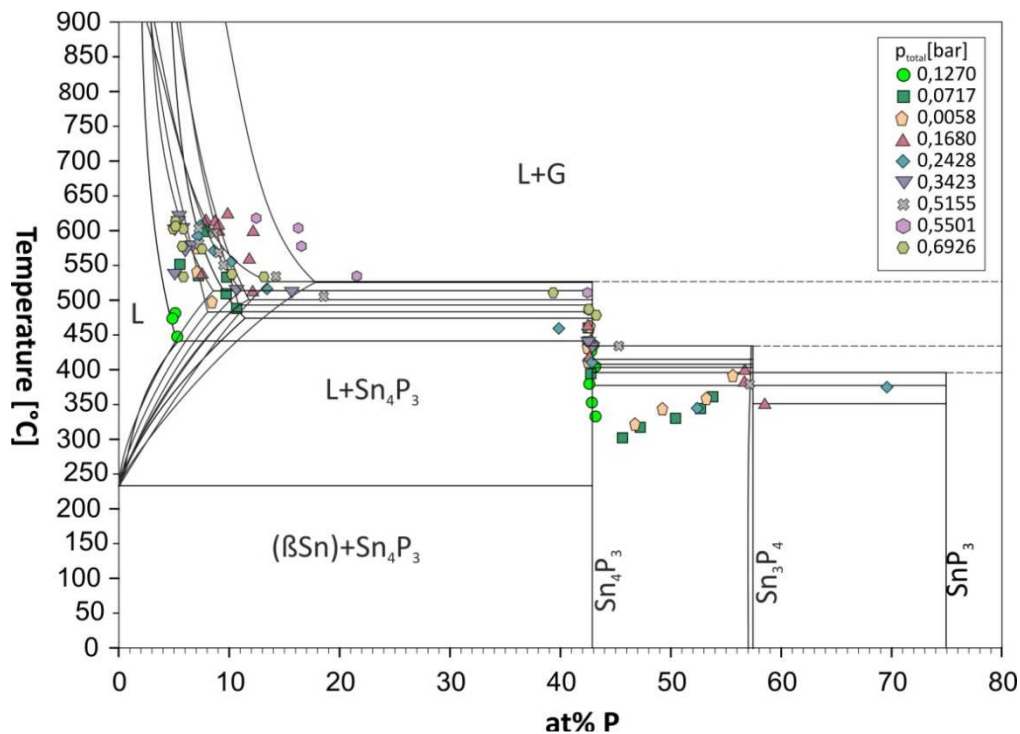


Fig. 5.1 schematic construction of the P-Sn phase diagram, superimposition of all isopiestic experiments

All three binary compounds described in literature were found during the investigations, Sn_4P_3 , Sn_3P_4 and SnP_3 .

The equilibrium samples achieved in all isopiestic experiments cover the phase diagram of Sn-P up to a P content of 70 at%. The majority of the samples are single phase samples, i.e. liquid, Sn_4P_3 and Sn_3P_4 . Some data points are located in the two phase fields ($\text{L}+\text{Sn}_4\text{P}_3$), ($\text{Sn}_4\text{P}_3+\text{Sn}_3\text{P}_4$), ($\text{Sn}_3\text{P}_4+\text{SnP}_3$).

At 0.006 bar the compound Sn_3P_4 was not found at all. This observation is in close agreement with Schmetterer et al. [28] who did not find the phase at 0.04 bar. It indicates that most likely the phase is not stable at lower vapor pressures. At higher pressures, starting at 0.07 bar, Sn_3P_4 was found as in the original phase diagram. The more Sn-rich binary compound Sn_4P_3 was found in each experiment and it seems to be stable in the whole pressure range. Due to its high P-content it was difficult to obtain the third binary compound SnP_3 . It is most likely that samples containing the SnP_3 -phase lost a considerable large amount of P during quenching and could not be identified correctly. Only at two different pressures this phase was found.

From the present investigations the homogeneity range of the binary compounds Sn_4P_3 and Sn_3P_4 was found to be about 0.8 at% and 0.4 at%, respectively.

The additional compounds mentioned in literature, SnP and Sn_7P_{10} , were not formed under the pressure and temperature conditions employed and could not be found in the present experiments. It can be concluded that they do not exist in the present pressure range.

The Sn-rich eutectic was taken as determined at 231 °C and constant in the whole pressure range. The reaction involves only condensed phases, so it is not much influenced by the pressure.

Problems appeared in experiments with P pressures higher than 0.7 bar. Here it was very difficult to maintain the equilibrium state inside the tube because the atmosphere broke down during quenching. It was not possible to immerse the tube into the water fast enough and it has to be assumed that samples with higher P content lost P during quenching. In Fig. 5.2 the phase diagram obtained from an isopiestic experiment at 1.02 bar is shown. It is seen that the temperatures (red) of the three phase equilibria are much lower compared to lower pressures.

The reaction $G+L=Sn_4P_3$ was found to be at about 500 °C which is far too low compared to literature [18, 19, 25] where the syntectic reaction of the liquid miscibility gap is at 550 and 559 °C, respectively. Also, compared to the experimental runs at lower pressures the extrapolation to 1 bar in the plot of p_{P_4} vs. $1/T$ (Fig. 5.4 (a)) would suggest a temperature around 540 °C.

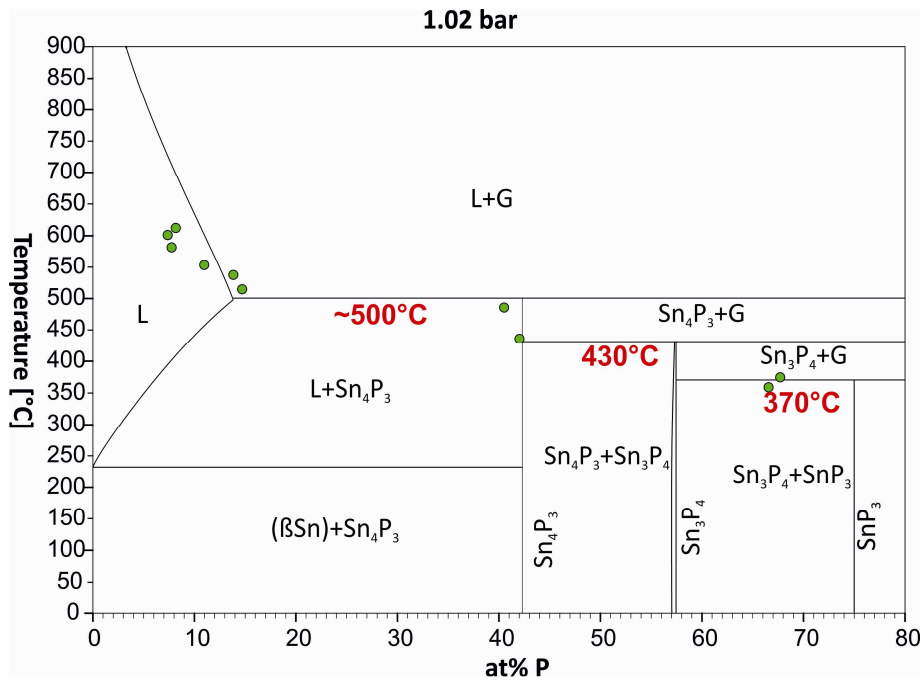
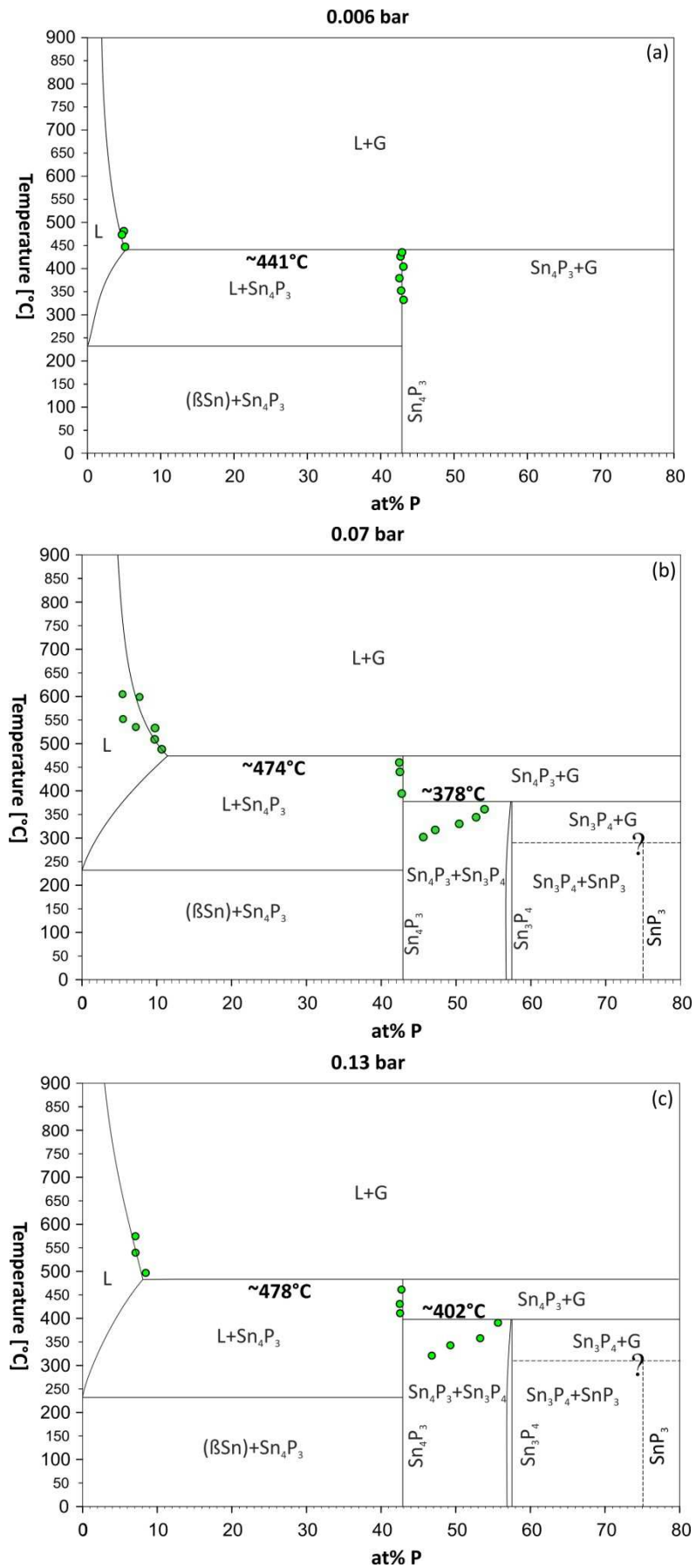


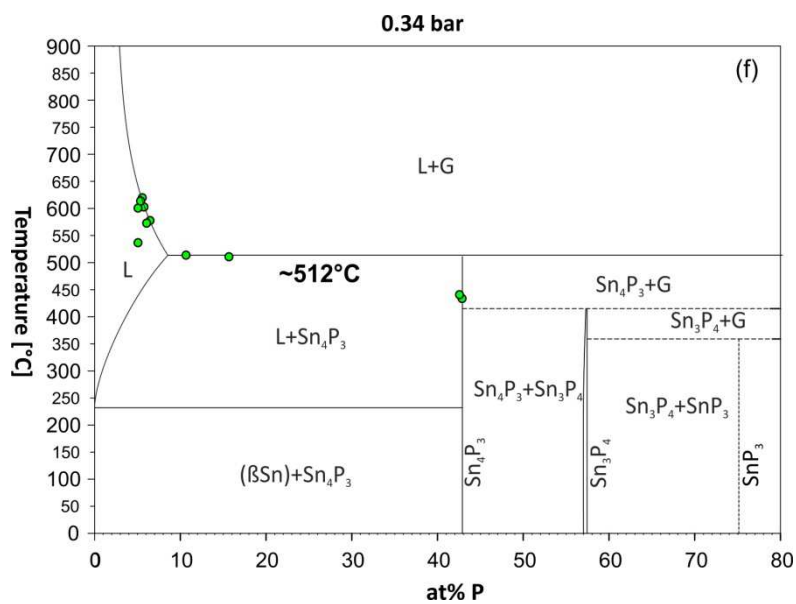
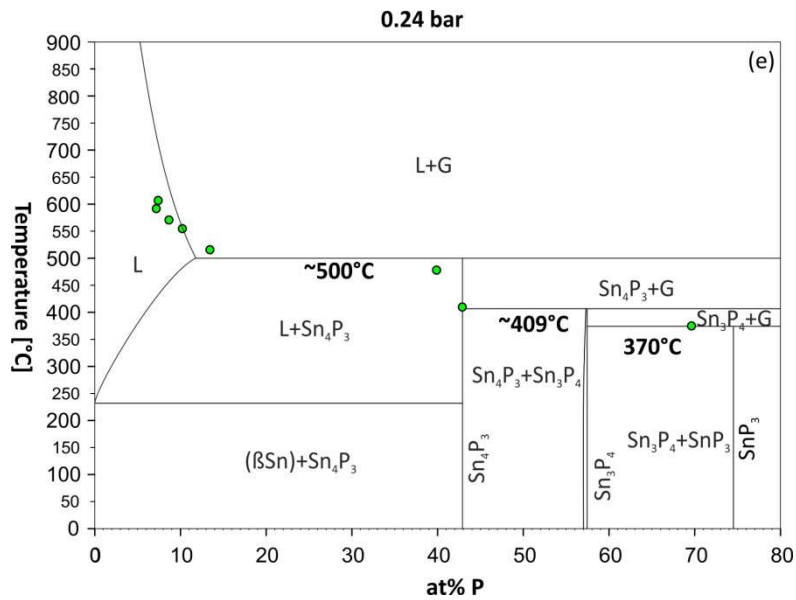
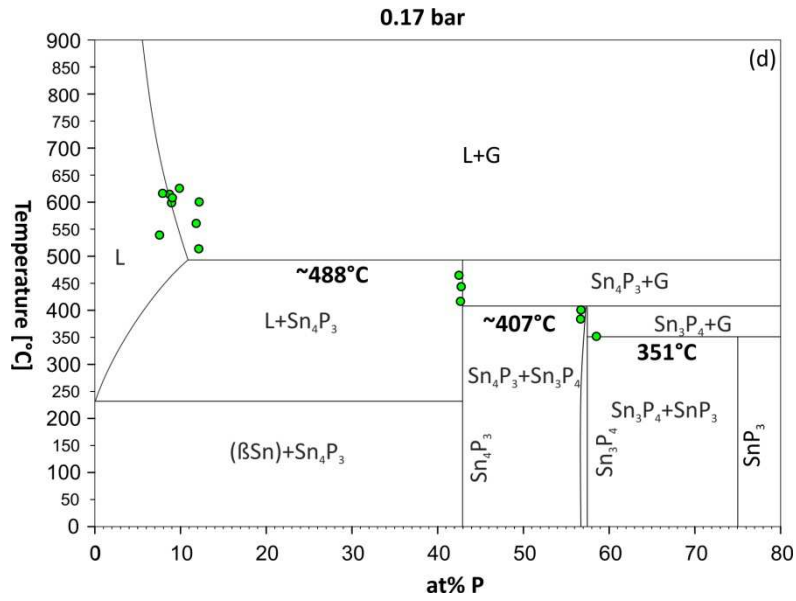
Fig. 5.2 T-x section of the P-Sn phase diagram at 1.023 bar

Even at lower pressure the loss of P from the samples during quenching was a big problem. As already mentioned it was difficult to obtain the most P-rich compound SnP_3 . It was only identified at pressures of 0.17 and 0.24.

For any future experiments the quenching step has to be improved in order to get constant and more reliable results at higher pressures and at increasing P-content. Quenching has to be much faster, so that the atmosphere in the tube does not break down while taking it out of the furnace.

Several samples appeared to have lost Sn during the experiment or during quenching since the weight after equilibration was lower than before. A possible explanation could be that tiny droplets of liquid Sn got separated from the bulk sample and solidified during quenching, sticking to the graphite lid. These samples were not included in the evaluation.





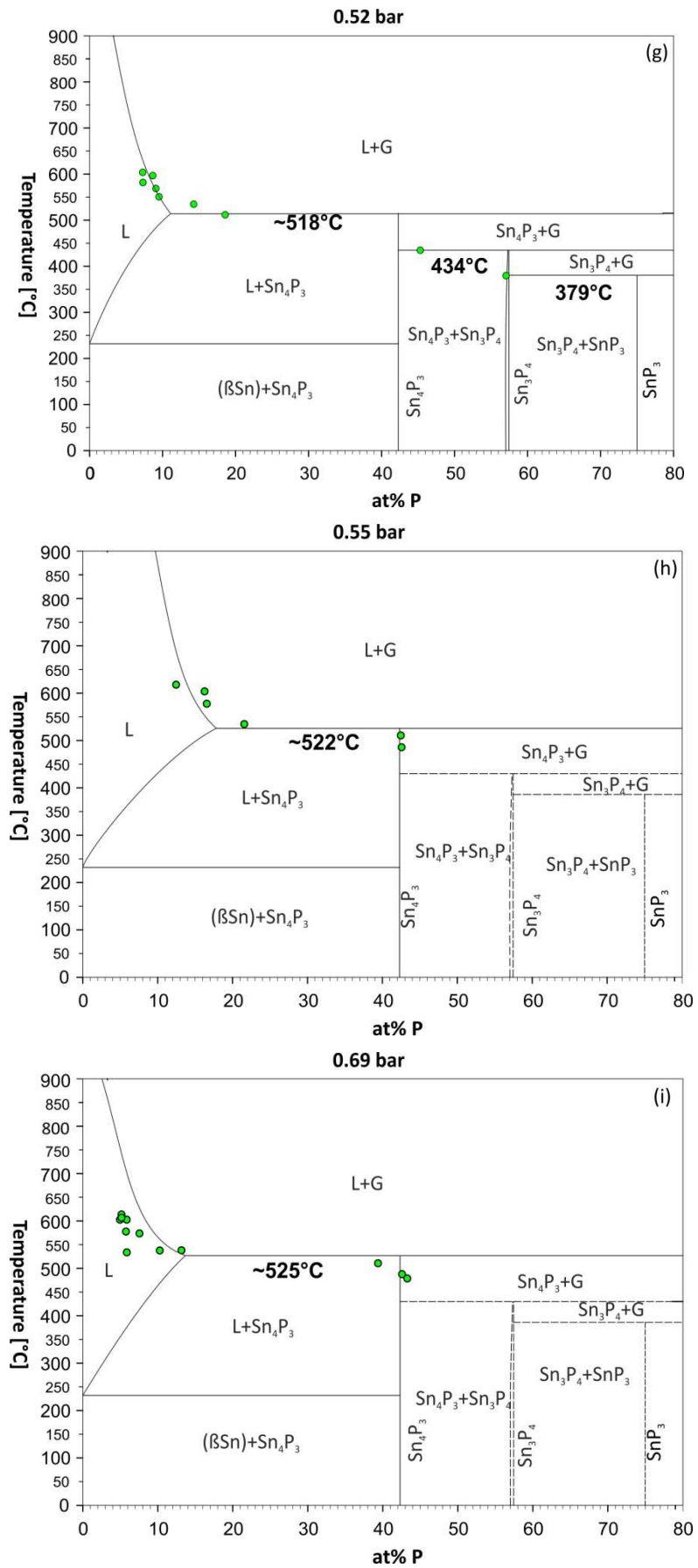


Fig. 5.3 T-x phase diagram of Sn-P at various pressures a)0.0058; b)0.0717; c)0.1270; d)0.1680; e)0.2428; f)0.3423; g)0.5155; h)0.5501, i)0.6926 bar;

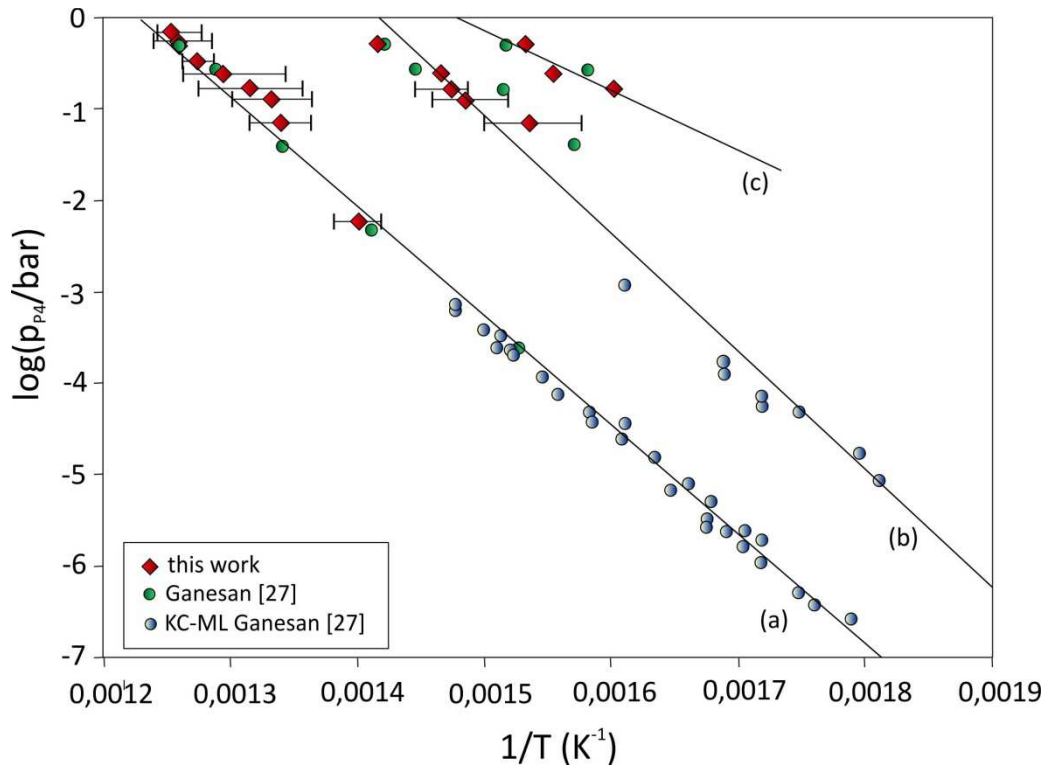


Fig. 5.4 Variation of the phosphorus vapor pressure over the two-phase fields
 (a) $(L+Sn_4P_3)$
 (b) $(Sn_4P_3+Sn_3P_4)$
 (c) $(Sn_3P_4+SnP_3)$

5.1.1.1 Formation of Sn_4P_3

In the work of Vivian [19] the formation of Sn_4P_3 is a syntectic reaction $L1+L2=Sn_4P_3$ whereas Schmetterer et al. [28] suggested a peritectic-like reaction $G+L=Sn_4P_3$ where the gas phase is involved in the formation of the binary phase. The latter authors mentioned the possibility that there could be a change in the formation mechanism of the phase Sn_4P_3 with increasing pressure. In this case there would have to be a quadruple point where L1, L2, G and Sn_4P_3 come together at the composition of the solid binary phase. Two observations that were already noted by Schmetterer et al. [28] would support this suggestion.

- With increasing pressure the limiting liquidus composition of the reaction $G+L=Sn_4P_3$ gets richer in phosphorus
- The equilibrium temperature of the reaction rises with increasing pressure and approaches the temperature suggested in the phase diagram printed in Massalski [18].

This, however, could not be confirmed here and still demands further experiments in the higher pressure range above 0.7 bar.

When looking at the individual phase diagrams established for each pressure in Fig. 5.3 a)-i) it is seen that the most Sn-rich binary compound Sn_4P_3 was found in each experiment, and it is most likely that the compound is stable in the whole pressure range and does not need a certain pressure to be formed. The data of Ganesan et al. [27] are in agreement with this conclusion. Ganesan et al. [27] also performed Knudsen cell based measurements (KC-ML) at very low pressures around 10^{-7} - 10^{-4} bar, which were also included in the discussion.

The equilibrium temperature of the reaction $\text{G}+\text{L}=\text{Sn}_4\text{P}_3$ was analyzed as a function of the pressure. It is seen that the value rises from 441 °C at 0.006 bar to a value of 525 °C at 0.69 bar. Only at three pressures samples were located directly in the two phase field and the exact temperature for the reaction could be derived. In the other cases the mean value between the data points at the phase boundaries (the highest temperature in the single-phase line of Sn_4P_3 and the lowest temperature of the L/L+G boundary) was calculated and this temperature was defined to be the equilibrium temperature. These values are given with error bars as the temperatures are not absolutely correct but should be in the range between the limiting values.

In the phase diagram plotted at 0.24 and 0.69 bar two samples are located inside the two-phase field and one could assume that these two temperatures define the equilibrium lines. However, since the temperatures are far too low compared to other results at comparable pressures, it is more likely that these two samples should rather be single-phase Sn_4P_3 but lost a small amount of P during quenching. The fact that both points are located close to the single-phase boundary of Sn_4P_3 affirms this suggestion. In both cases again the median was calculated to get the equilibrium temperature.

In Fig. 5.5 the results of all isopiestic runs of this work and the isopiestic measurements of the work of Ganesan et al. [27] are plotted, whereas in Fig. 5.4 (a) also the results of the KC-ML method are included. In Tab.5.2 all relevant data are listed. The data of Ganesan et al. [27] agree reasonably well with the present results.

Ganesan et al. [27] pointed out, that due to the good agreement between results of the KC-ML and from the isopiestic method their results should be more reliable than those of Arita and Kamo [22]. This is supported by the present study.

Extrapolation of all data including KC-ML measurements (Fig. 5.4 (a)) would suggest a temperature of ~ 540 °C for the formation of Sn_4P_3 at 1 bar. The value is, although slightly lower, in rather good agreement with the one in the phase diagram printed in Massalski [18] where the syntectic reaction $\text{L1}+\text{L2}=\text{Sn}_4\text{P}_3$ was found at 550 °C. Again, this could also indicate a change in the formation mechanism of the phase Sn_4P_3 with increasing pressure.

The value was obtained by extrapolation of the function to a $\log p_{\text{P}_4}$ value of 0 ($p_{\text{P}_4}=1$ bar). This point represents the value $1/T$. From that it is possible to calculate the temperature at 1 bar.

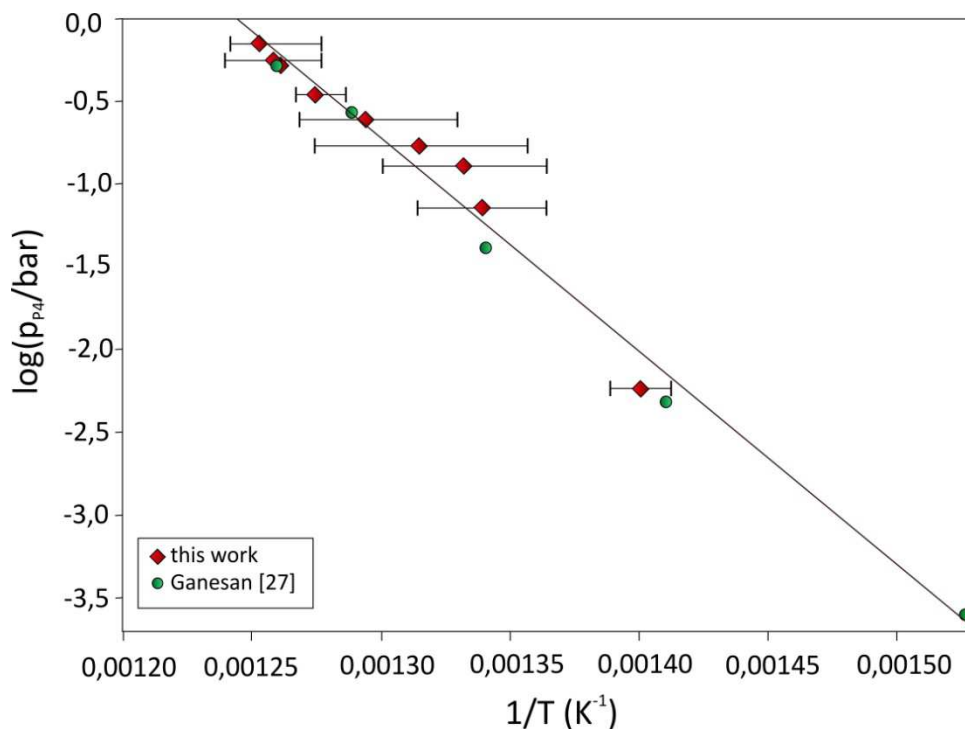


Fig. 5.5 Variation of the P_4 partial pressure with temperature of the reaction $\text{L}+\text{G}=\text{Sn}_4\text{P}_3$; isopiestic experiments

5 Results and discussion

Tab.5.2 Results for the equilibrium L+G = Sn₄P₃

p_{P_4} [bar]	$\log p_{P_4}$ [bar]	T[°C]/[K]	T _{lower limit} [°C]/[K]	T _{upper limit} [°C]/[K]
0.0058	-2.2388	441/714	435/708	447/720
0.0717	-1.1447	474/747	460/733	488/761
0.1270	-0.8963	478/751	460/733	496/769
0.1679	-0.7750	488/761	464/737	512/785
0.2426	-0.6151	500/773	485/758	515/788
0.3422	-0.4658	512/785	510/783	513/786
0.5152	-0.2880	518/791		
0.5497	-0.2599	522/795	510/783	534/807
0.6922	-0.1598	525/798	510/783	538/811
Ganesan et al. [27]				
0.0003	-3.6071	382/655	-	-
0.0048	-2.3194	436/709	-	-
0.0408	-1.3892	473/746	-	-
0.2685	-0.5713	503/776	-	-
0.5155	-0.2880	521/794	-	-
Knudsen cell results [27]				
2.6E-05	-4.5850	349/622	-	-
2.1E-04	-3.6778	384/657	-	-
3.9E-04	-3.4089	394/667	-	-
7.2E-04	-3.1427	404/677	-	-
1.2E-04	-3.9208	374/647	-	-
2.6E-04	-3.5850	389/662	-	-
6.6E-04	-3.1805	404/677	-	-
7.5E-05	-4.1249	369/642	-	-
3.8E-05	-4.4202	358/631	-	-
3.3E-04	-3.4815	388/661	-	-
2.2E-04	-3.6576	384/657	-	-
3.8E-04	-3.4202	394/667	-	-
7.1E-04	-3.1487	404/677	-	-
2.0E-06	-5.6990	309/582	-	-
8.0E-06	-5.0969	329/602	-	-
1.5E-05	-4.8239	339/612	-	-
5.1E-06	-5.2924	323/596	-	-
2.5E-06	-5.6021	313/586	-	-
4.7E-05	-4.3279	359/632	-	-
3.6E-05	-4.4437	348/621	-	-
1.1E-06	-5.9586	309/582	-	-
2.7E-06	-5.5686	324/597	-	-
6.8E-06	-5.1675	334/607	-	-
2.4E-06	-5.6198	319/592	-	-
5.2E-07	-6.2840	299/572	-	-
2.6E-07	-6.5850	286/559	-	-
3.7E-07	-6.4318	295/568	-	-
1.6E-06	-5.7959	314/587	-	-
3.3E-06	-5.4815	324/597	-	-

5.1.1.2 Limiting liquidus composition

The intersection of the equilibrium line for the reaction $L+G=Sn_4P_3$ with the liquidus line indicates the limiting liquidus composition and hence defines the maximum content of phosphorus dissolved in the liquid at a certain pressure. The data values obtained for this point with increasing pressure are listed in Tab. 5.3. A trend to higher P-content with increasing pressure can be seen although there are two data points at 0.34 and 0.55 bar which don't fit to the trend.

The data were analyzed in two ways. In Fig. 5.6 the phosphorous vapor pressures p as a function of the P-content of the limiting liquidus are plotted whereas in Fig. 5.7 the phosphorous pressures p are plotted as logarithmic values. In both figures it is seen that at lower pressures (<0.1 bar) the values of Ganesan et al. [27] are in good agreement with the present ones but deviate towards P-poor compositions at higher pressures.

Tab. 5.3 results for the limiting liquidus composition

p [bar]	log p [bar]	at%P	at%P_{upper limit}
0.0058	-2.2384	5.1	
0.0717	-1.1445	6.9	7.9
0.1270	-0.8961	7.5	9.5
0.1680	-0.7748	10.7	13.1
0.2428	-0.6148	11.8	14.3
0.3423	-0.4655	8.9	10.8
0.5155	-0.2878	11.9	13.8
0.5501	-0.2596	17.8	
0.6926	-0.1595	13.9	
Ganesan [27]			
0.0002	-3.6126	3	-
0.0047	-2.3249	5.5	-
0.0403	-1.3946	6	-
0.2649	-0.5769	7	-
0.5088	-0.2935	8	-

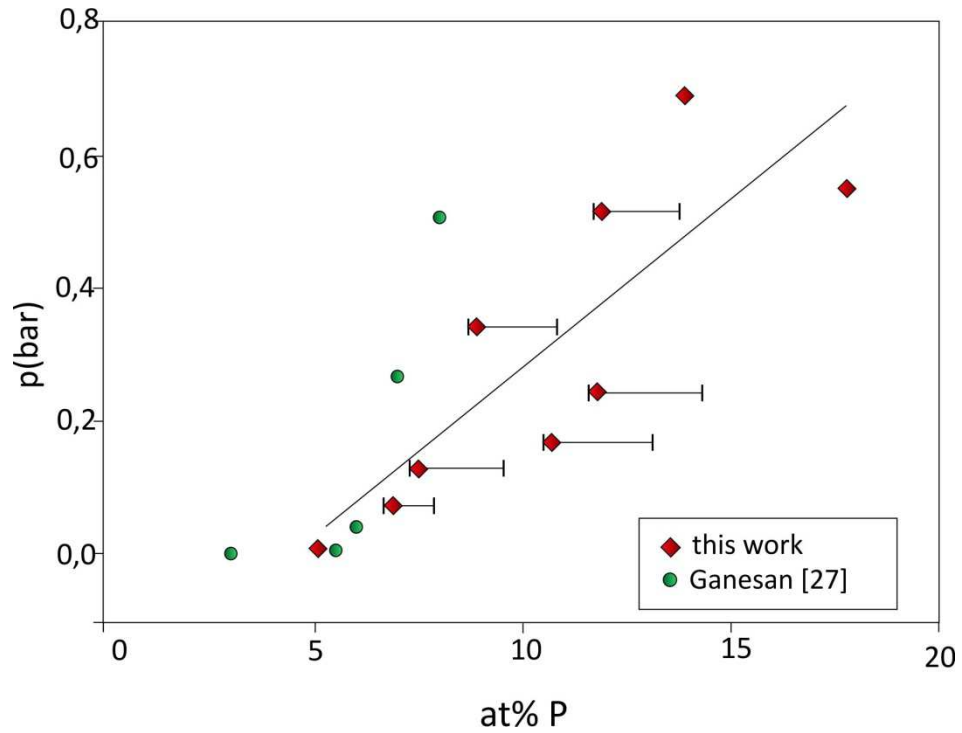


Fig. 5.6 phosphorous pressure p as a function of the composition of the limiting liquidus

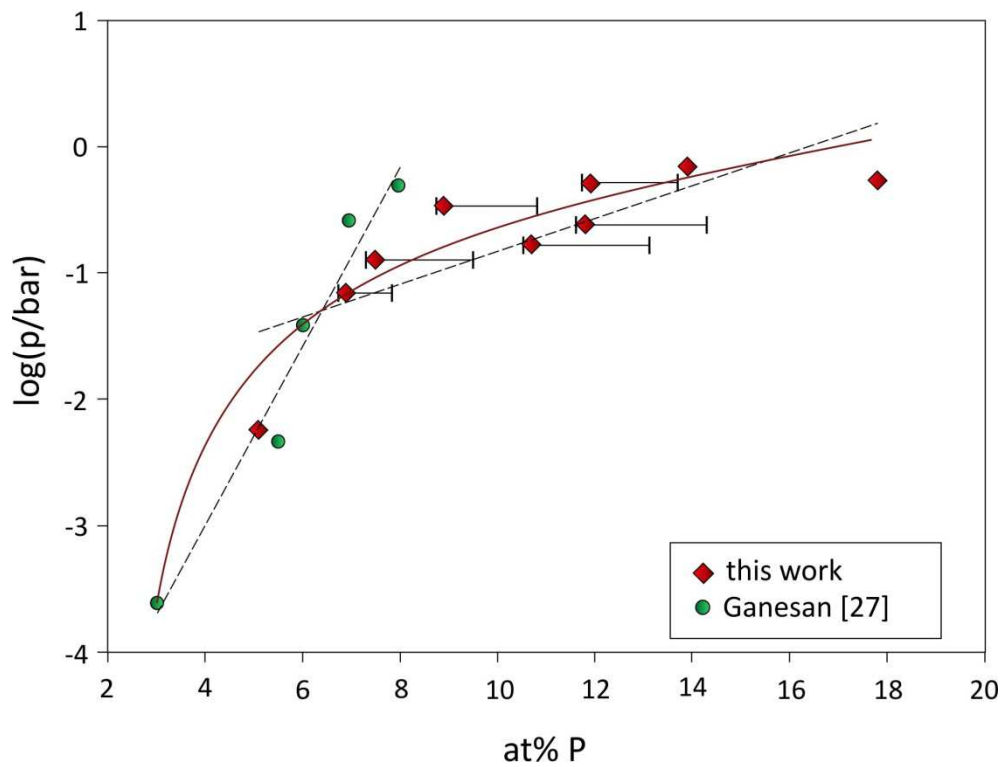


Fig. 5.7 logarithm of the phosphorous pressure $\log p$ as a function of the composition of the limiting liquidus

5.1.1.3 Formation of Sn_3P_4

The formation of Sn_3P_4 In the phase diagram printed in Massalski it is suggested to be a congruent transformation out of the Liquid L2 at 560 °C. From further investigations it is clear that the gas phase is involved in the formation of the compound and that the reaction is in fact the peritectic-type reaction $\text{G} + \text{Sn}_4\text{P}_3 = \text{Sn}_3\text{P}_4$. This conclusion can be made because it is rather apparent that the binary compound needs a certain vapor pressure of P to be formed. In the present work Sn_3P_4 was not found at the lowest pressure 0.006 bar. This determination is in close agreement with Schmetterer et al. [28] who did not find the phase at 0.04 bar. At higher pressures, both in Ref. [28] and in the present work, Sn_3P_4 was found like in the original phase diagram. At pressures above 0.52 bar no sample with Sn_3P_4 was formed but only because no experiments were placed into the temperature region necessary for formation.

Even though Sn_3P_4 was found at 0.07 and 0.13 bar it was not formed as single phase. All data points are located in the two phase field ($\text{Sn}_4\text{P}_3 + \text{Sn}_3\text{P}_4$). These results are in agreement with the work of Ganesan et al. [32] who produced single phase Sn_3P_4 and confirmed that the binary compound cannot be formed in pure form at phosphorus pressures lower than 0.042 bar.

The equilibrium temperature of the reaction $\text{G} + \text{Sn}_4\text{P}_3 = \text{Sn}_3\text{P}_4$ was analyzed as a function of the pressure. Schmetterer et al. [28] reported an unusual behavior of the reaction because it showed no constant trend but the equilibrium temperature decreases and rises again. The results in the present work do not agree with these data. Contrary to their observations the behavior of the formation reaction shows increasing equilibrium temperature values with increasing pressure. The values rise from 332 °C at 0.006 bar to a value of 434 °C at 0.52 bar. Again for pressures where samples were not located in the two phase field the mean value between the values at the phase boundaries was calculated and this temperature was defined to be the equilibrium temperature (see section 5.1.1.1.).

The results of Ganesan et al. [27] are in close agreement with the present ones. In Fig. 5.8 the results of all isopiestic runs of this work and the isopiestic measurements

of the work of Ganesan et al. [27] are plotted, whereas in Fig. 5.4 (b) also the results of the KC-ML method [27] are included. All relevant data are also listed in Tab. 5.4.

Extrapolation of the present data including KC-ML experiments (Fig. 5.4 (b)) would suggest a temperature of ~435 °C for the formation of Sn₃P₄ at 1 bar. This value agrees reasonably with the result of Schmetterer et al. [28] who found an equilibrium temperature of 430 °C at 0.7 bar. Also their other results are matching well with the data values in the present work except for the unusual increase at 0.16 bar to 452 °C.

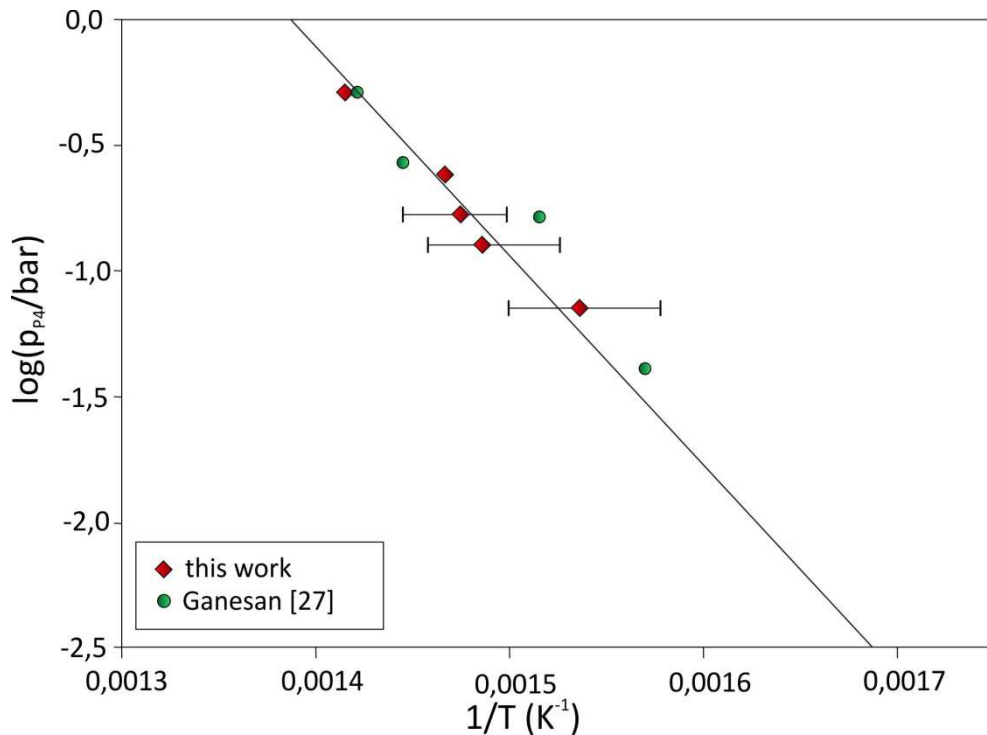


Fig. 5.8 Variation of the P₄ partial pressure with temperature of the reaction G+Sn₄P₃=Sn₃P₄; isopiestic experiments

Tab. 5.4 Results for the equilibrium G+Sn₄P₃=Sn₃P₄

p _{P4} [bar]	log p _{P4} [bar]	T[°C]/[K]	T _{lower limit} [°C]/[K]	T _{upper limit} [°C]/[K]
0.0717	-1.1445	378/651	361/634	394/667
0.1270	-0.8961	402/675	390/663	413/686
0.1680	-0.7748	407/678	400/673	414/687
0.2427	-0.6148	409/682		
0.5155	-0.2878	434/707		
Ganesan [27]				
0.0408	-1.3889	364/637	-	-
0.1634	-0.7866	387/660	-	-
0.2684	-0.5712	419/692	-	-
0.5155	-0.2878	431/704	-	-

p_{P_4} [bar]	$\log p_{P_4}$ [bar]	T [°C]/[K]	$T_{\text{lower limit}}$ [°C]/[K]	$T_{\text{upper limit}}$ [°C]/[K]
Knudsen cell results [27]				
1.2E-03	-2.9208	348/621	-	-
1.7E-04	-3.7696	319/592	-	-
1.7E-05	-4.7696	284/557	-	-
4.8E-05	-4.3188	299/572	-	-
7.1E-05	-4.1487	309/582	-	-
1.3E-04	-3.8861	319/592	-	-
8.8E-06	-5.0555	279/552	-	-
5.7E-05	-4.2441	309/582	-	-

5.1.1.4 Formation of SnP_3

For the formation reaction of the most P-rich phase only three data points were obtained. Already Schmetterer et al. [28] as well as Ganesan et al. [27] reported about problems with the binary compound SnP_3 . Even the phase diagrams present in literature by Massalski [18] or Levinsky [25] give no explicit information in this region. It is very difficult to produce samples in this two phase field ($\text{Sn}_3\text{P}_4+\text{SnP}_3$) because of the high P-content. During quenching the samples in this region lose a large amount of P. The compound has a strong dependence of the vapor pressure and when the atmosphere breaks down in the tube during quenching the sample abruptly loses P.

At lower pressures no SnP_3 was found. It appeared the first time at a pressure of 0.17 bar. Like the formation of Sn_3P_4 it is possible that the binary compound is only formed above a certain vapor pressure. This conclusion is in agreement with the data of Ganesan et al. [27] who obtained only two data points in the two-phase field at pressures above 0.27 bar.

The two data points at 0.17 and 0.24 bar are located directly in the two phase field, the temperature was considered to be the equilibrium temperature. The data point at 0.52 bar was actually a single-phase sample of Sn_3P_4 but was determined as phase boundary of the two phase field.

The equilibrium temperature rises from 351 °C at 0.17 bar to 379 °C at 0.52 bar. In the work of Ganesan et al. [27] the data point of the reaction $\text{G}+\text{Sn}_3\text{P}_4=\text{SnP}_3$ rise from 359 °C at 0.27 bar to 386 °C at 0.52 bar. All data are listed in Tab. 5.5. Although the

values show some scattering they can still be compared reasonably. The data points in the present work are at higher temperatures. In Fig. 5.9 the equilibrium temperatures as a function of the phosphorus vapor pressures are plotted. It is seen that the points have a large variance.

Extrapolation of all available data (Fig. 5.9) would suggest a temperature of ~ 407 °C for the formation of SnP_3 at 1 bar. Due to the lack of information in the works of Schmetterer et al. [28] as well as of Levinsky [25], this value could not be compared. Also, in the phase diagram printed in Massalski [18] the P-rich reaction is only hypothetically at about 570°C and indicated as dotted lines.

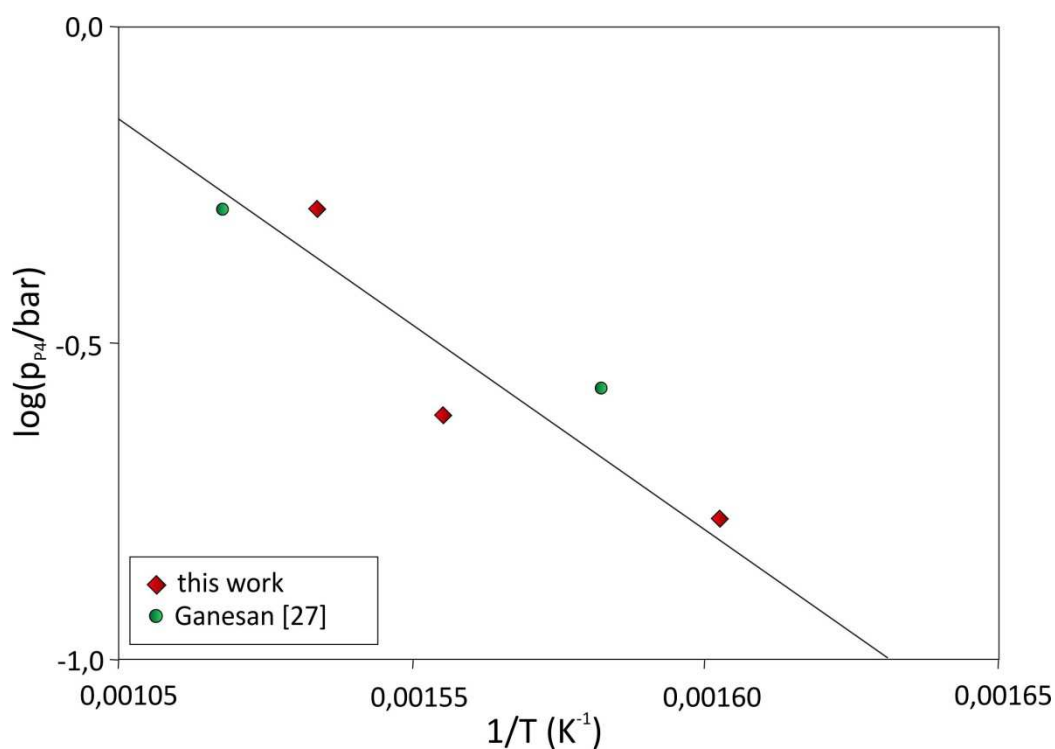


Fig. 5.9 Variation of the P_4 partial pressure with temperature of the reaction $\text{G} + \text{Sn}_3\text{P}_4 = \text{SnP}_3$; isopiestic experiments

Tab. 5.5 Results for the equilibrium $\text{G} + \text{Sn}_3\text{P}_4 = \text{SnP}_3$

p_{P_4} [bar]	$\log p_{\text{P}_4}$ [bar]	T[°C]/[K]
0.1680	-0.7748	351/624
0.2428	-0.6148	370/643
0.5155	-0.2878	379/652
Ganesan [27]		
0.2685	-0.5711	359/632
0.5155	-0.2878	386/659

Although the data, which were obtained at 1.02 bar, were not considered in the present analysis it has to be mentioned that the phase SnP_3 was obtained in this experimental run (see Fig. 5.2). This is also an indication, that the phase is more stable at higher P pressures. The data points are located at ~ 370 °C in the two phase field ($\text{Sn}_3\text{P}_4 + \text{SnP}_3$), which is lower than the calculated value at 1 bar. It is likely that the sample should rather be single phase SnP_3 but lost P during quenching.

5.1.2 Thermodynamic data

As mentioned in section 2.1 in the vapor phase of white phosphorus three different species are mainly present, P_4 and P_2 as well as P atoms. In Hultgren et al. [17] values for the partial pressure of each species up to 600 K are listed as well as the total vapor pressure up to a temperature of 550 K. In the work of Ganesan et al. [55] also a fourth species P_3 was listed which was derived from the SGTE data by Dinsdale [90]. According to these data the values for the molecular species in the vapor pressure in equilibrium were calculated and plotted in Fig. 5.10. As can be seen, P_4 is the dominant species in the vapor. Since the partial pressure values of monoatomic P and the molecule P_3 are so much lower than those of the others, these two species can be omitted in the calculations. As a result the total vapor pressure of white phosphorus can be expressed by

$$p_{\text{total}} = p_{P_2} + p_{P_4} \quad \text{Eq.5.1}$$

where p_{P_2} and p_{P_4} are the partial pressures of the two species.

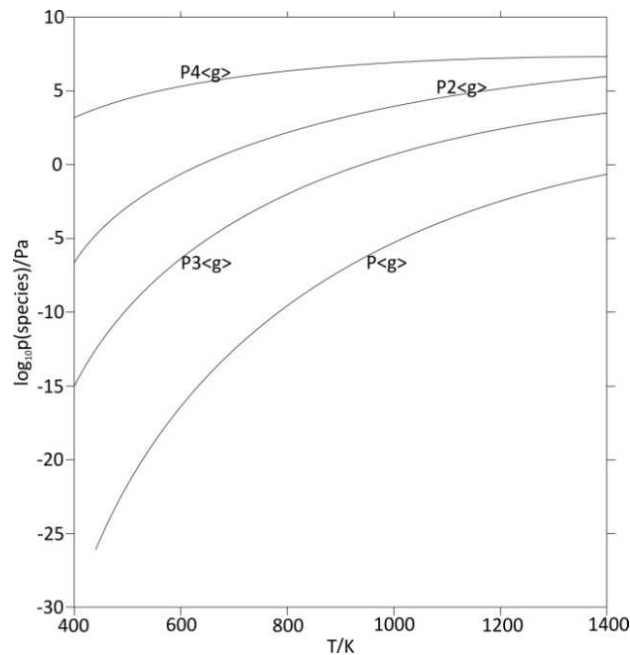


Fig. 5.10 calculated speciation of the gas phase of white phosphorus according to Ganesan [55]

The data listed by Hultgren et al. [17] were used by Ganesan et al. [27] to fit an equation for the total vapor pressure of phosphorus in the system:

$$\log(p_{\text{total}}/\text{bar}) = 19.7676 - 3621.5(K/T) - 4.813 \log(T/K) \quad \text{Eq.5.2}$$

$T: 279 - 550\text{K}$

The equilibrium constant

$$K_{eq} = \frac{p_{P_2}^2}{p_{P_4}} \quad \text{Eq.5.3}$$

defines the equilibrium state between the two species P_4 and P_2 in the gaseous phase according to the reaction



The values for the equilibrium constant can be computed from Eq.5.5 which was again derived by Ganesan et al. [27] from the partial pressure values of Ref. [17] and are in close arrangement with the values determined by Arita and Watanabe [91] for higher temperatures.

$$\log(K_{eq}/\text{bar}) = 10.2827 - 12030.9(K/T) - 0.726 \log(T/K) \quad \text{Eq.5.5}$$

$T: 298 - 600\text{K}$

It is possible to calculate the partial pressure of P_4 according to the sample temperature T_S and the pressure defined by the reservoir from

$$p_{\text{total}} = \sqrt{K_{eq} \cdot p_{P_4}} + p_{P_4} \quad \text{Eq.5.6}$$

For the calculation of the phosphorus activities in the liquid phase only the partial pressure of P_4 was used, as its value is the highest.

$$a_P = \sqrt[4]{\frac{p_{P_4}(T_S)}{p_{P_4}^0(T_S)}} \quad \text{Eq.5.7}$$

$p_{P_4}(T_S)$ is the partial pressure of P_4 over the sample and $p_{P_4}^0(T_S)$ is the vapor pressure of P_4 from pure white phosphorus both at the sample temperature T_S .

According to Ganesan [27] $p_{P_4}^0(T_S)$ can be obtained by

$$\log(p_{P_4}^0/\text{bar}) = 17.8535 - 3513.3(K/T) - 4.182 \log(T/K) \quad \text{Eq.5.8}$$

$T: 298 - 600\text{K}$

All of these functions were used to calculate the vapor pressures in the present work for the whole temperature range.

Tab. 5.6 thermodynamic data obtained from the isopiestic experiments

p_{total} [bar]	T_s [°C]/[K]	$p_{P_4}^0(T_s)$ [bar]	K_{eq}	$p_{P_4}(T_s)$ [bar]	$\ln a_P(T_s)$	at%P	$\overline{\Delta H_P}$ [Jmol ⁻¹]	$\ln a_P$ (750K)
0.0058	447/720	10.582	3.186E-09	0.0058	-1.879	5.14	-19085	-1.75
	473/746	13.495	1.187E-08	0.0058	-1.939	4.71	-20914	-1.92
	481/754	14.481	1.746E-08	0.0058	-1.957	4.96	-19851	-1.97
0.0717	488/761	15.377	2.432E-08	0.0717	-1.342	10.67	4430	-1.33
	509/782	18.256	6.338E-08	0.0716	-1.385	9.73	433	-1.38
	533/806	21.891	1.780E-07	0.0716	-1.431	9.77	603	-1.42
0.1270	551/824	24.853	3.712E-07	0.0715	-1.463	5.63	-17002	-1.71
	598/871	33.474	2.188E-06	0.0713	-1.538	7.88	-7434	-1.70
	604/877	34.660	2.706E-06	0.0713	-1.547	5.56	-17299	-1.95
0.1680	496/769	16.440	3.525E-08	0.1270	-1.216	8.15	-6286	-1.24
	539/812	22.857	2.283E-07	0.1269	-1.298	7.13	-10623	-1.43
	574/847	28.917	9.066E-07	0.1267	-1.358	7.12	-10666	-1.55
0.1680	512/785	18.690	7.237E-08	0.1679	-1.178	12.09	10468	-1.10
	538/811	22.694	2.191E-07	0.1678	-1.227	7.67	-8327	-1.33
	599/872	33.670	2.267E-06	0.1674	-1.326	12.16	10766	-1.08
0.2428	607/880	35.260	3.006E-06	0.1673	-1.338	9.05	-2459	-1.40
	615/888	36.882	3.966E-06	0.1672	-1.349	7.91	-7306	-1.53
	624/897	38.744	5.384E-06	0.1670	-1.362	9.85	943	-1.34
0.2428	560/833	26.407	5.296E-07	0.1677	-1.265	11.86	9490	-1.11
	598/871	33.474	2.188E-06	0.1674	-1.325	9.00	-2671	-1.38
	614/887	36.678	3.832E-06	0.1672	-1.348	8.74	-3777	-1.44
0.2428	515/788	19.130	8.254E-08	0.2426	-1.092	13.48	16379	-0.97
	554/827	25.366	4.183E-07	0.2424	-1.163	10.25	2644	-1.12
	570/843	28.189	7.790E-07	0.2423	-1.189	8.70	-3947	-1.26
0.2428	591/864	32.113	1.701E-06	0.2421	-1.222	7.21	-10283	-1.44
	606/879	35.060	2.903E-06	0.2419	-1.244	7.43	-9347	-1.46

p_{total} [bar]	T_s [°C]/[K]	$p_{P_4}^0(T_s)$ [bar]	K_{eq}	$p_{P_4}(T_s)$ [bar]	$\ln a_P(T_s)$	at%P	$\Delta \overline{H}_P$ [Jmol ⁻¹]	$\ln a_P$ (750K)
0.3423	536/809	22.371	2.017E-07	0.3421	-1.045	5.08	-19340	-1.27
	572/845	28.552	8.405E-07	0.3418	-1.106	6.13	-14875	-1.37
	600/873	33.867	2.349E-06	0.3414	-1.149	5.09	-19298	-1.59
	613/886	36.474	3.702E-06	0.3412	-1.168	5.41	-17937	-1.61
	577/850	29.470	1.015E-06	0.3418	-1.114	6.46	-13472	-1.37
	602/875	34.263	2.522E-06	0.3414	-1.152	5.80	-16279	-1.53
	619/892	37.705	4.547E-06	0.3411	-1.176	5.63	-17002	-1.61
0.5155	550/823	24.683	3.567E-07	0.5151	-0.967	9.55	-333	-0.97
	568/841	27.828	7.217E-07	0.5149	-0.997	9.11	-2204	-1.04
	581/854	30.214	1.178E-06	0.5147	-1.018	7.34	-9730	-1.21
	596/869	33.082	2.037E-06	0.5145	-1.041	8.70	-3947	-1.13
	603/876	34.461	2.612E-06	0.5143	-1.051	7.31	-9858	-1.28
0.5501	577/850	29.470	1.015E-06	0.5493	-0.996	16.61	29689	-0.44
	603/876	34.461	2.612E-06	0.5489	-1.035	16.31	28413	-0.38
	617/890	37.293	4.247E-06	0.5485	-1.055	12.55	12424	-0.74
0.6926	533/806	21.891	1.780E-07	0.6922	-0.863	13.24	15358	-0.69
	537/810	22.532	2.102E-07	0.6922	-0.871	10.29	2814	-0.84
	573/846	28.734	8.730E-07	0.6918	-0.932	7.64	-8454	-1.09
	577/850	29.470	1.015E-06	0.6917	-0.938	5.76	-16449	-1.25
	601/874	34.065	2.434E-06	0.6913	-0.974	5.86	-16024	-1.34
	602/875	34.263	2.522E-06	0.6912	-0.976	5.00	-19681	-1.43
	606/879	35.060	2.903E-06	0.6911	-0.982	5.23	-18702	-1.42
	613/886	36.474	3.702E-06	0.6910	-0.992	5.20	-18830	-1.46

5.1.2.1 Partial enthalpy of mixing

The calculation of the partial enthalpy of formation $\Delta\overline{H}_P$ is based on the data of Ganesan et al. [27]. They derived the values for $\Delta\overline{H}_P$ by plotting the natural logarithms of the phosphorus activity for selected compositions in the liquid region against $1/T$ with hypothetical sample temperatures for the selected compositions. These temperatures were derived by extrapolation of the equilibrium curves in the liquid region. With the obtained $\ln a_p$ values the partial enthalpies were fitted according to

$$\frac{\partial \ln a_p}{\partial (1/T)} = \frac{\Delta\overline{H}_P}{R} \quad \text{Eq.5.10}$$

where R is the gas constant.

Their values for $\Delta\overline{H}_P$ were plotted against the composition and a least square fitted straight line expression was obtained. This expression was used to calculate the partial enthalpies for each sample in the liquidus phase at the derived composition. The values for $\Delta\overline{H}_P$ were then used to transform the activities of phosphorus to a temperature of 750 K according to

$$\ln a_p(750) = \ln a_p(T_S) + \frac{\Delta\overline{H}_P}{R} \left(\frac{1}{750} - \frac{1}{T_S} \right) \quad \text{Eq.5.11}$$

The results for $\Delta\overline{H}_P$ as well as for the activities $\ln a_p(750)$ are listed in Tab. 5.6 and a diagram of $\ln a_p(750)$ as a function of the composition in the liquid phase is shown in Fig. 5.11. The diagram includes the data points in the liquid phase obtained by Ganesan et al. [27] and it is seen that the data values are in good agreement with the results obtained in the present work. It can be seen in Fig. 5.11 that the data points show a nicely shaped logarithmic function, the values of Ganesan et al. [27] start at lower pressure values from 0.0002 to 0.52 bar whereas the data points of the present work cover a pressure range of 0.006 to 0.69 bar.

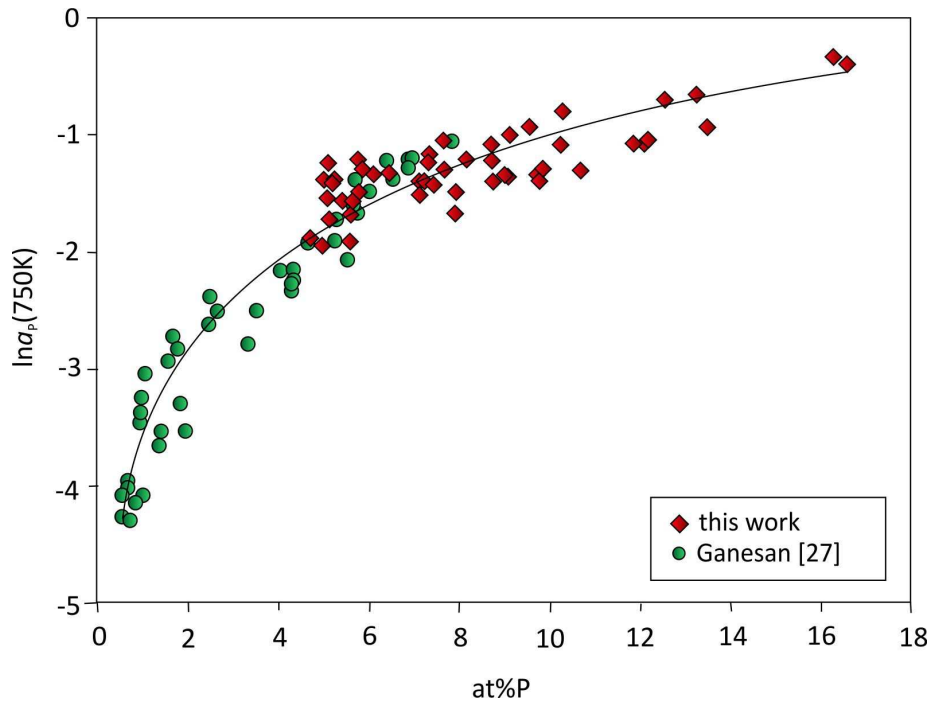
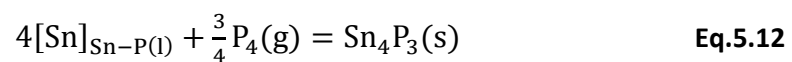


Fig. 5.11 Natural logarithm of the phosphorus activity $\ln a_P$ as a function of the composition in the liquid phase at 750K

5.1.2.2 Standard molar Gibbs energy of formation

5.1.2.2.1 Sn_4P_3

The phosphorus pressure p_{P_4} that was measured over the two phase field (L + Sn_4P_3) correlates to the equilibrium



Applying the least-squares method to the pressure data leads to the following equation

$$\log(p_{\text{P}_4}/\text{bar}) = 16.16 - 12988(\text{K}/T) \quad \text{Eq.5.13}$$

$T: 714 - 798\text{K}$

Calculation of the standard molar Gibbs energy of formation of $\text{Sn}_4\text{P}_3(\text{s})$ was carried out according to

$$\Delta_f G_m^0(\text{Sn}_4\text{P}_3)(\text{s}) = 4RT \ln a_{\text{Sn}} + \frac{3}{4}RT \ln p_{\text{P}_4} \quad \text{Eq.5.14}$$

where the measured phosphorus data were used for p_{P_4} .

Assuming Raoult's law for the Sn-rich liquid it is possible to express a_{Sn} as x_{Sn} and further, any non-stoichiometry for the phase Sn_4P_3 was neglected.

The obtained standard molar Gibbs energy of formation of $\text{Sn}_4\text{P}_3(\text{s})$ from the present measurements as well as the data points of Ganesan et al. [27] are plotted in Fig. 5.12. By comparing the values it is seen that the data are in good agreement. The values for $\Delta_f G_m^0(\text{Sn}_4\text{P}_3)(\text{s})$ of the present work can be calculated as

$$\Delta_f G_m^0(\text{Sn}_4\text{P}_3)(\text{s})(\text{kJmol}^{-1}) = -158.6 + 0.192(T/\text{K}) \quad \text{Eq.5.15}$$

$$T: 714 - 798\text{K}$$

Due to the fact, that the data of Ganesan et al. [27] cover a much larger temperature range and are in very good agreement with the present data, the equation computed in Ref. [27] as

$$\Delta_f G_m^0(\text{Sn}_4\text{P}_3)(\text{s}) \pm 1.1/(\text{kJmol}^{-1}) = -166.5 + 0.2007(T/\text{K}) \quad \text{Eq.5.16}$$

$$T: 559 - 794\text{K}$$

was used for further calculation instead of Eq.5.15.

In Tab. 5.7 all relevant data are listed.

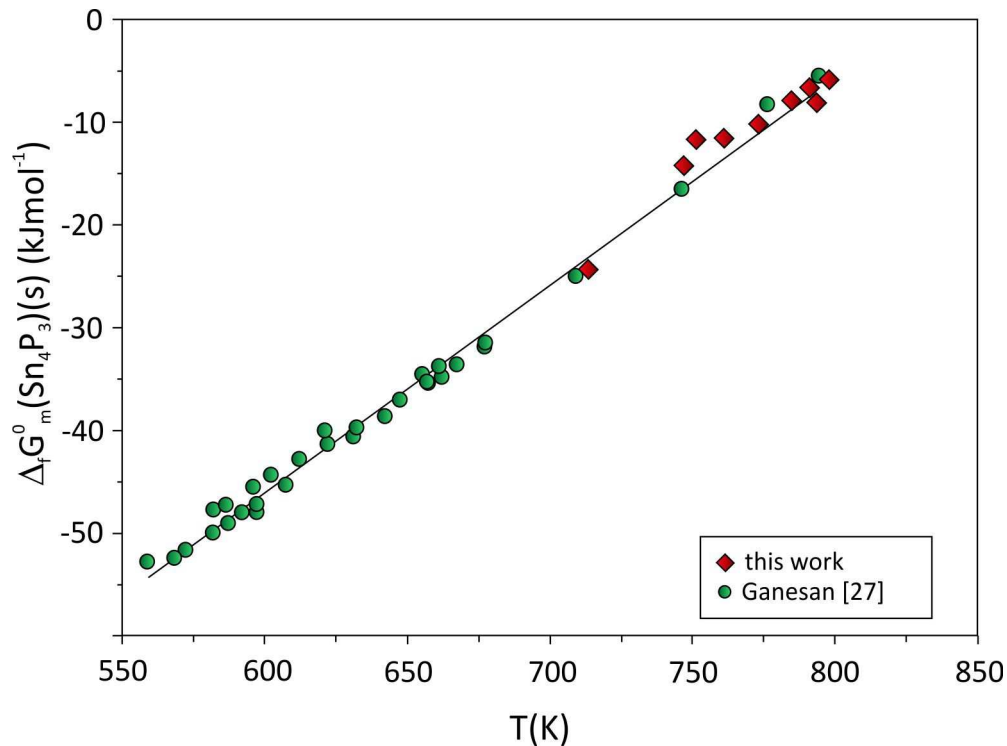


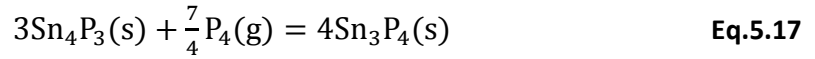
Fig. 5.12 Variation of the standard molar Gibbs energy of formation of $\text{Sn}_4\text{P}_3(\text{s})$ with temperature

Tab. 5.7 results for the standard molar Gibbs energy of formation of Sn_4P_3 (s)

T[K]	p_{P_4} [bar]	$x_{\text{Sn}}=a_{\text{Sn}}$	$\Delta_f G_m^0(\text{Sn}_4\text{P}_3)(s)$ [kJmol ⁻¹]
714	0.0058	0.949	-24.19
747	0.0717	0.931	-14.05
751	0.1270	0.925	-11.61
761	0.1679	0.893	-11.33
773	0.2426	0.882	-10.05
785	0.3422	0.911	-7.68
791	0.5152	0.881	-6.60
795	0.5497	0.822	-8.15
798	0.6922	0.861	-5.80
Ganesan [27]			
655	0.0002	0.970	-34.59
709	0.0048	0.945	-24.95
746	0.0408	0.940	-16.42
776	0.2685	0.930	-8.24
794	0.5155	0.920	-5.49
KC-ML [27]			
622	$2.60 \cdot 10^{-05}$	0.979	-41.39
657	$2.10 \cdot 10^{-04}$	0.967	-35.42
667	$3.90 \cdot 10^{-04}$	0.964	-33.46
677	$7.20 \cdot 10^{-04}$	0.961	-31.45
647	$1.20 \cdot 10^{-04}$	0.971	-37.06
662	$2.60 \cdot 10^{-04}$	0.966	-34.84
677	$6.60 \cdot 10^{-04}$	0.961	-31.82
642	$7.50 \cdot 10^{-05}$	0.972	-38.62
631	$3.80 \cdot 10^{-05}$	0.976	-40.56
661	$3.30 \cdot 10^{-04}$	0.966	-33.80
657	$2.20 \cdot 10^{-04}$	0.967	-35.23
667	$3.80 \cdot 10^{-04}$	0.964	-33.57
677	$7.10 \cdot 10^{-04}$	0.961	-31.51
582	$2.00 \cdot 10^{-06}$	0.992	-47.77
602	$8.00 \cdot 10^{-06}$	0.986	-44.35
612	$1.50 \cdot 10^{-05}$	0.982	-42.75
596	$5.10 \cdot 10^{-06}$	0.988	-45.53
586	$2.50 \cdot 10^{-06}$	0.991	-47.31
632	$4.70 \cdot 10^{-05}$	0.976	-39.79
621	$3.60 \cdot 10^{-05}$	0.979	-40.05
582	$1.10 \cdot 10^{-06}$	0.992	-49.94
597	$2.70 \cdot 10^{-06}$	0.987	-47.99
607	$6.80 \cdot 10^{-06}$	0.984	-45.36
592	$2.40 \cdot 10^{-06}$	0.989	-47.99
572	$5.20 \cdot 10^{-07}$	0.996	-51.69
559	$2.60 \cdot 10^{-07}$	1.000	-52.85
568	$3.70 \cdot 10^{-07}$	0.997	-52.51
587	$1.60 \cdot 10^{-06}$	0.991	-49.03
597	$3.30 \cdot 10^{-06}$	0.987	-47.24

5.1.2.2.2 Sn₃P₄

The phosphorus pressure p_{P_4} that was measured over the two phase field (Sn₄P₃ + Sn₃P₄) correlates to the equilibrium



Applying the least-squares method to the pressure data leads to the following equation

$$\log(p_{P_4}/\text{bar}) = 9.887 - 7209(\text{K}/T) \quad \text{Eq.5.18}$$

$T: 650 - 707\text{K}$

Calculation of the standard molar Gibbs energy of formation of Sn₃P₄(s) was carried out according to

$$4\Delta_f G_m^0(\text{Sn}_3\text{P}_4)(\text{s}) = 3\Delta_f G_m^0(\text{Sn}_4\text{P}_3)(\text{s}) + \frac{7}{4}RT \ln p_{P_4} \quad \text{Eq.5.19}$$

where $\Delta_f G_m^0(\text{Sn}_4\text{P}_3)(\text{s})$ was obtained from Eq.5.16 by extrapolation to lower temperatures and the measured pressure data were used for p_{P_4} .

The standard molar Gibbs energy of formation was calculated neglecting any non-stoichiometry for the binary compounds Sn₄P₃ and Sn₃P₄.

Again a very good agreement can be seen by comparing the Gibbs data of the present work with the values obtained by Ganesan et al. [27], as seen in Fig. 5.13.

Due to the fact, that the data of [27] cover a much larger temperature range and are in very good agreement with the present data, the equation computed in Ref. [27] as

$$\Delta_f G_m^0(\text{Sn}_3\text{P}_4)(\text{s}) \pm 1,8/(\text{kJmol}^{-1}) = -234.4 + 0.3053(T/\text{K}) \quad \text{Eq.5.20}$$

$T: 552 - 705\text{K}$

was used for further calculation.

In Tab. 5.8 all relevant data are listed.

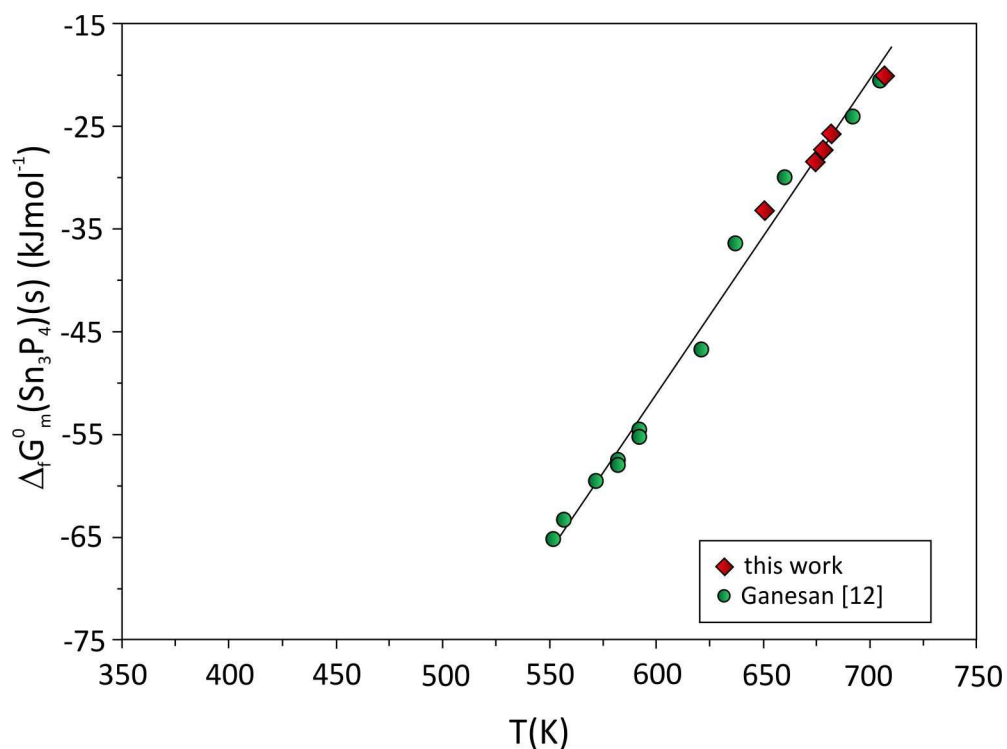


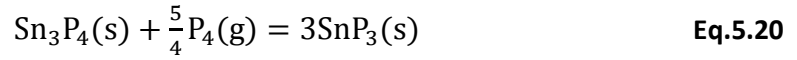
Fig. 5.13 Variation of the standard molar Gibbs energy of formation of $\text{Sn}_3\text{P}_4(\text{s})$ with temperature

Tab. 5.8 results for the standard molar Gibbs energy of formation of $\text{Sn}_3\text{P}_4(\text{s})$

T[K]	p_{P_4} [bar]	$\Delta_f G_m^0(\text{Sn}_3\text{P}_4)(\text{s})$ [kJmol^{-1}]
651	0.0717	-33.12
675	0.1270	-28.34
678	0.1680	-27.22
682	0.2427	-25.73
707	0.5155	-20.16
Ganesan [27]		
637	0.0408	-36.40
660	0.1644	-29.86
692	0.2684	-24.02
704	0.5155	-20.60
KC-ML [27]		
592	$1.20 \cdot 10^{-03}$	-46.59
557	$1.70 \cdot 10^{-04}$	-54.46
572	$1.70 \cdot 10^{-05}$	-63.28
582	$4.80 \cdot 10^{-05}$	-59.47
592	$7.10 \cdot 10^{-05}$	-57.49
552	$1.30 \cdot 10^{-04}$	-55.03
582	$8.80 \cdot 10^{-06}$	-65.16

5.1.2.2.3 SnP₃

The phosphorus pressure p_{P_4} that was measured over the two phase field (Sn₃P₄ + SnP₃) correlates to the equilibrium



Applying the least-squares method to the pressure data leads to the following equation

$$\log(p_{P_4}/\text{bar}) = 9.553 - 6466(\text{K}/T) \quad \text{Eq.5.21}$$

$T: 624 - 652\text{K}$

Calculation of the standard molar Gibbs energy of formation of SnP₃(s) was carried out according to

$$3\Delta_f G_m^0(\text{SnP}_3)(\text{s}) = \Delta_f G_m^0(\text{Sn}_3\text{P}_4)(\text{s}) + \frac{5}{4}RT \ln p_{P_4} \quad \text{Eq.5.23}$$

where $\Delta_f G_m^0(\text{Sn}_3\text{P}_4)(\text{s})$ was obtained from Eq.5.20 by extrapolation to lower temperatures and the measured pressure data were used for p_{P_4} .

The standard molar Gibbs energy of formation was again calculated neglecting any non-stoichiometry for the binary compound Sn₃P₄.

In Fig. 5.14 the obtained standard molar Gibbs energy of formation of Sn₄P₃(s) from the present measurements as well as the data points of Ganesan et al. [27] are plotted. The values show some scattering but can still be compared reasonably.

The values for $\Delta_f G_m^0(\text{SnP}_3)(\text{s})$ of the present work can be calculated as

$$\Delta_f G_m^0(\text{SnP}_3)(\text{s})(\text{kJmol}^{-1}) = -130.0 + 0.1787(T/\text{K}) \quad \text{Eq.5.24}$$

$T: 624 - 652\text{K}$

Whereas Ganesan et al. [27] obtained the following expression

$$\Delta_f G_m^0(\text{SnP}_3)(\text{s})(\text{kJmol}^{-1}) = -113.0 + 0.1523(T/\text{K}) \quad \text{Eq.5.25}$$

$T: 632 - 659\text{K}$

The data in this region of the phase diagram are rather limited and the values for $\Delta_f G_m^0(\text{SnP}_3)(\text{s})$ at least give an estimate of the stability of this P-rich phase.

All relevant data are listed in Tab. 5.9.

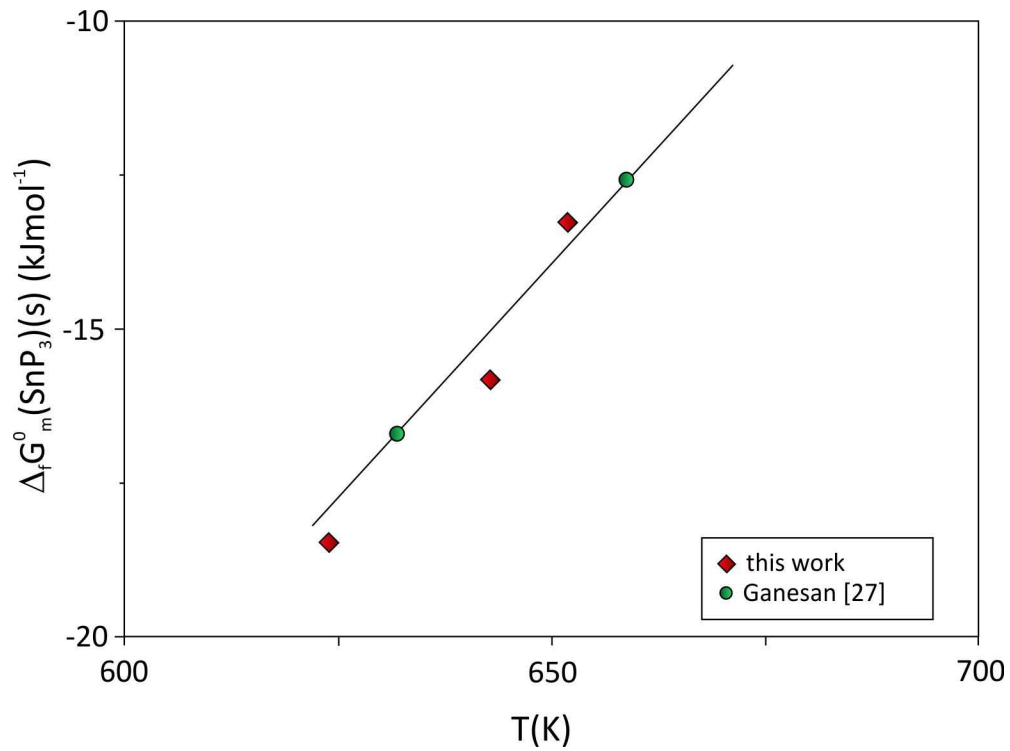


Fig. 5.14 Variation of the standard molar Gibbs energy of formation of $\text{SnP}_3(\text{s})$ with temperature

Tab. 5.9 results for the standard molar Gibbs energy of formation of $\text{SnP}_3(\text{s})$

T[K]	p_{P_4} [bar]	$\Delta_f G_m^0(\text{Sn}_3\text{P}_4)(\text{s})$ [kJmol^{-1}]
624	0.1680	-18.49
643	0.2428	-15.85
652	0.5155	-13.28
Ganesan [27]		
632	0.2685	-16.70
659	0.5155	-12.58

5.2 Results in the system Ni-P-Sn

An isothermal section of the Ni-P-Sn phase diagram was made at 300 °C in the Sn-rich part of the phase diagram with a constant ratio of Sn:Ni of about 3:1.

Several problems occurred during the experiments.

- Samples with a P-content higher than 60 at% caused problems because of the high evaporation of P in the sample tubes. As already shown in section 4.2.1 (Tab. 4.3 and Fig. 4.8) the most P-rich samples could not be analyzed. Some of the sample tubes burst in the furnace during the temperature treatment because of the high vapour pressure that developed in the quartz tube. This could possibly be avoided by an even slower heating rate than chosen at critical temperatures, such as at the sublimation of P at 450 °C and at the high exothermic reaction of P with Ni at 550°C. Other samples could not be used for further investigations due to the condensation of phosphorous at the inner quartz glass wall, which happened most likely during quenching.
- Most of the samples are not in the equilibrium state. At a P-content of more than 15 at% in nearly all samples four phases were found in XRD or EDX. So further interpretations of the data can only be considered as an assumption. It can be assumed that the non equilibrium-state in most of the samples is due to the low annealing temperature of 300 °C and could maybe improved by longer annealing durations. Furthermore, the arising gaseous phase of P can be an explanation for the missing equilibria. Schmetterer [2] explained the appearance of more than three phases by an additional reason. T5 is formed out of Ni₂P and the liquid in a (quasi-binary) peritectic reaction. The appearance of Ni₂P can indicate an incomplete formation of T5. In the present work, though, the binary phase Ni₂P was never found next to T5.
- The vapour pressure dependence of the binary phase diagrams is still a large problem for getting constant and reliable results.

Already Schmetterer [2] found out that at 200 °C the solubility of Ni and P in the solid solution of (Sn) is rather insignificant like in the binary systems Ni-Sn and P-Sn. The same observation was made in the samples in the ternary at 300 °C. EDX

measurements show that the homogeneity range of the (Sn)-liquid is rather small. The solubility was found to be between 0 and 0.6 at% for both elements, Ni and P.

All relevant experimental results for the ternary system are listed in Tab. 5.10

Tab. 5.10 Experimental results of phase analysis of the Ni-P-Sn system

Sample	Nominal composition	Phase	Structure type	XRD		EDX at%		
				Lattice parameters Å		Ni	P	Sn
NPS1	Ni _{24.51} P _{1.93} Sn _{73.56}	(Sn)*	βSn	a=5.8291 c= 3.1799	0.61		99.39	
		T5	Ni ₂ PSn	a=12.8091 b=3.6017 c=5.0958	42.53	24.66	57.47	
		Ni ₃ Sn ₄	Ni ₃ Sn ₄	a= 12.1963 b=4.0581 c=5.2165 β=105.192	48.54		26.80	
NPS2	Ni _{24.00} P _{4.01} Sn _{71.99}	(Sn)*	βSn	a=5.8317 c= 3.1815	0.22		99.79	
		T5	Ni ₂ PSn	a=12.8160 b=3.5970 c=5.0880	48.60	24.67	26.74	
		Ni ₃ Sn ₄	Ni ₃ Sn ₄	a=12.1988 b= 4.0601 c=5.2170 β=105.194	42.18		57.82	
NPS3	Ni _{23.54} P _{5.81} Sn _{70.65}	(Sn)*	βSn	a= 5.8314 c= 3.1814	0.51		99.49	
		T5	Ni ₂ PSn	a=12.8235 b=3.5975 c=5.0932	48.21	24.81	26.99	
		Ni ₃ Sn ₄	Ni ₃ Sn ₄	a=12.2020 b=4.0582 c=5.2196 β=105.231	42.16		57.84	
NPS4	Ni _{22.76} P _{8.97} Sn _{68.28}	(Sn)*	βSn	a=5.8316 c= 3.1815	0.42		99.59	
		T5	Ni ₂ PSn	a=12.8287 b=3.5984 c=5.0938	49.24	24.62	26.14	
		Ni ₃ Sn ₄	Ni ₃ Sn ₄	a=12.2011 b=4.0579 c=5.2203 β=105.232	42.05		57.96	
NPS5	Ni _{22.41} P _{10.36} Sn _{67.24}	(Sn)*	βSn	a=5.8317 c= 3.1815	0.28		99.72	
		T5	Ni ₂ PSn	a= 12.8275 b=3.5962 c=5.0914	49.44	24.65	25.91	
		Ni ₃ Sn ₄	Ni ₃ Sn ₄	not found in XRD	42.14		57.86	
NPS6	Ni _{21.53} P _{13.86} Sn _{64.60}	(Sn)*	βSn	a=5.8316 c= 3.1815	0.50		99.50	
		T5	Ni ₂ PSn	a= 12.8226 b=3.5906 c=5.0876	48.78	25.71	25.51	
NPS7	Ni _{20.78} P _{16.86} Sn _{62.35}	(Sn)*	βSn	a=5.8313 c= 3.1812			100	
		T5	Ni ₂ PSn	a= 12.8217 b=3.5918 c=5.0883	48.92	25.29	25,80	
		NiP ₂	NiP ₂	a=6.3685 b=5.6164 c=6.0727	33.45	66.56		
		Ni ₅ P ₄	Ni ₅ P ₄	a= 6.7992 c=11.0231	55.17	43.96	0.87	
NPS8	Ni _{19.50} P _{22.01} Sn _{58.49}	(Sn)*	βSn	a=5.8317 c= 3.1815			100	
		T5	Ni ₂ PSn	a= 12.8310 b=3.5904 c=5.0908	49.31	25.18	25.52	
		NiP ₂	NiP ₂	a= 6.3687 b=5.6162 c=6.0731	33.43	66.55	0.02	
		Ni ₅ P ₄	Ni ₅ P ₄	a=6.8002 c=11.0219	not found		in SEM	
NPS9	Ni _{18.31} P _{26.76} Sn _{54.93}	(Sn)*	βSn	a=5.8318 c= 3.1816	0.06	0.11	99.83	
		T5	Ni ₂ PSn	a= 12.8340 b=3.5906 c=5.0891	49.26	25.27	25.47	
		NiP ₂	NiP ₂	a=6.3690 b=5.6158 c=6.0731	55.00	44.21	0.79	
		Ni ₅ P ₄	Ni ₅ P ₄	a=6.8025 c=11.0164	33.34	66.65	0.02	

Sample	Nominal composition	Phase	Structure type	XRD	EDX at%		
				Lattice parameters Å	Ni	P	Sn
NPS10	Ni _{14.75} P _{40.99} Sn _{44.25}	(Sn)*	βSn	a= 5.8317c= 3.1816	0.12	0.23	99.65
		NiP ₂	NiP ₂	a=6.3681 b=5.6163 c=6.0731	33.36	66.58	0.07
		Sn ₄ P ₃	Bi ₃ Se ₄	a= 3.9666 c= 35.3522	0.16	42.20	57.64
		NiP ₃	NiP ₃	a= 7.8209	25.09	74.86	0.06
NPS11	Ni _{14.00} P _{43.98} Sn _{42.02}	(Sn)*	βSn	a=5.8298 c= 3.1808		0.44	99.56
		NiP ₂	NiP ₂	a=6.3652 b=5.6143 c=6.0701	32.88	66.97	0.16
		Sn ₄ P ₃	Bi ₃ Se ₄	a= 3.9658 c=35.3342	0.05	42.16	57.79
		NiP ₃	NiP ₃	a=7.8185	not found		in SEM
NPS12	Ni _{12.27} P _{50.96} Sn _{36.78}	(Sn)*	βSn	a=5.8323 c= 3.1817	0.15	0.58	99.28
		NiP ₂	NiP ₂	a=6.3675b= 5.6160 c=6.0724	33.15	66.70	0.15
		Sn ₄ P ₃	Bi ₃ Se ₄	a= 3.9675 c= 35.3478		42.31	57.69
		NiP ₃	NiP ₃	a=7.8210	24.53	75.41	0.06
NPS13	Ni _{11.26} P _{54.93} Sn _{33.81}	Sn ₄ P ₃	Bi ₃ Se ₄	a= 3.9699c= 35.3611		42.67	57.34
		NiP ₃	NiP ₃	a=7.8235	25.00	74.96	0.05

*Sn(l) at 300°C, solidified during quenching

In samples NPS 1 to NPS 5 three phases were found, besides the liquid of (Sn) the ternary compound T5 and the binary phase Ni₃Sn₄ were present in the sample. These five samples can be correlated to a phase triangulation [(Sn) (l) +T5+ Ni₃Sn₄]. These data stand in contrast to the results of Schmetterer [2]. His isothermal section at 200 °C shows the two phase triangulations [(Sn) +T3+ Ni₃Sn₄] and [(Sn) +T3+T5]. Nevertheless, in the present work no indication for the ternary phase T3 had been found. In Fig. 5.16 the SEM image of the sample NPS 1 is shown. One can see the liquid solution of (Sn) surrounding small crystals of T5 and larger crystals of Ni₃Sn₄.

The sample NPS 6 was found to be a two phase sample of (Sn)(l) and T5.

In samples NPS 7 to NPS 9 four phases were found; again (Sn)(l), T5 and two binary compounds of the Ni-P system, namely Ni₅P₄ and NiP₂, apparently as a consequence of incomplete annealing. This could either indicate the existence of a three-phase field [(Sn) (l) + T5 + NiP₂] where Ni₅P₄ has not disappeared completely or the existence of two separate three-phase equilibria [(Sn)(l) + T5 + Ni₅P₄] and [(Sn)(l) + NiP₂ + Ni₅P₄] which would be in agreement with the results of Schmetterer [2] at 200 °C.

Also four phases were found in samples NPS 10 to NPS 12: the solution of (Sn)(l), two binary phases of the Ni-P system, namely NiP_2 and NiP_3 and the most Sn-rich binary phase in the Sn-P system, namely Sn_4P_3 . Two possible phase triangulations can be concluded from these results: either the two phase triangulations [(Sn) (l) + Sn_4P_3 + NiP_2] and [Sn_4P_3 + NiP_2 + NiP_3] or [(Sn) (l) + NiP_2 + NiP_3] and [(Sn) (l) + Sn_4P_3 + NiP_3]. In Fig. 5.17 an SEM image of sample NPS 10 is shown. A small amount of (Sn) (l) is seen as well as a larger area of Sn_4P_3 . The binary phases NiP_2 and NiP_3 are harder to distinguish because seem to be crystallized together.

Sample NPS 13 was the only sample where no (Sn) (l) was found. Only two phases were found in this sample, Sn_4P_3 and NiP_3 .

In Fig. 5.15 the isothermal section at 300 °C is shown. Phase fields that are based on non equilibrium samples are drawn with dotted lines. Interpretation of the data was performed in all possible ways and drawn in different colors. The grey lines define the phase triangulations that are in agreement with Schmetterer [2].

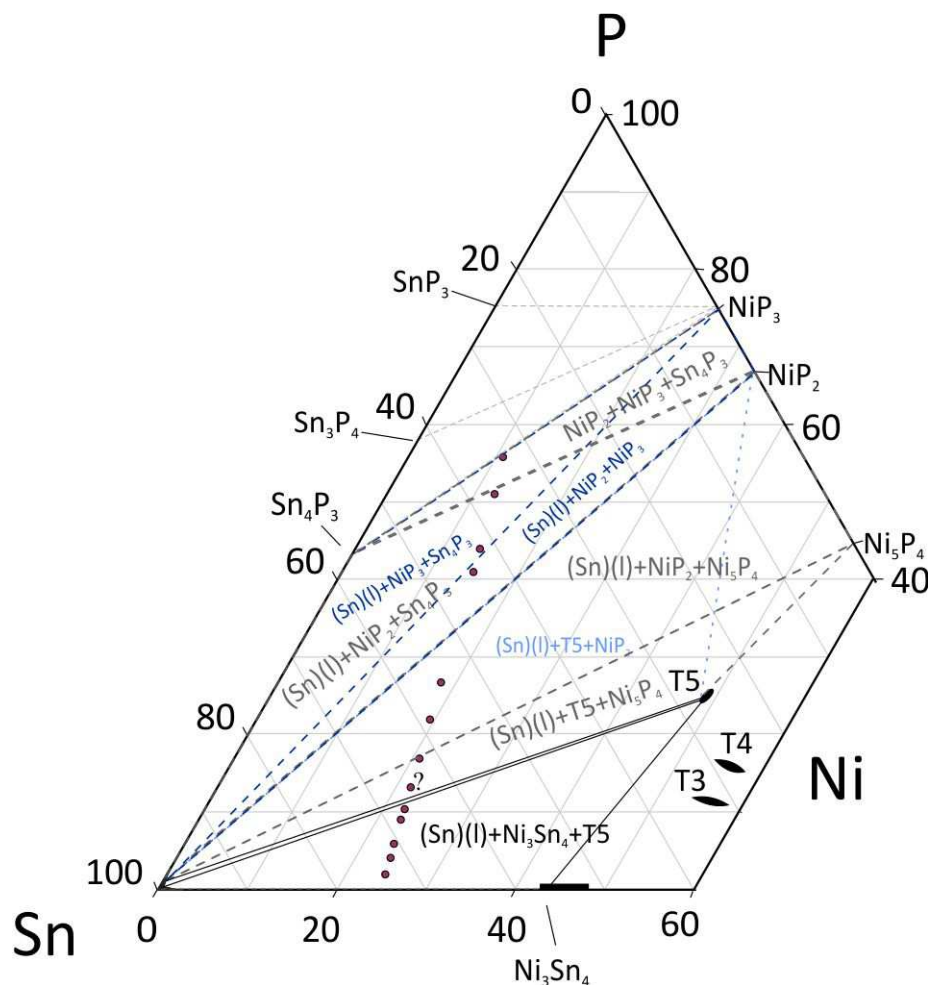


Fig. 5.15 partial isothermal section of the Ni-P-Sn system at 300 °C;

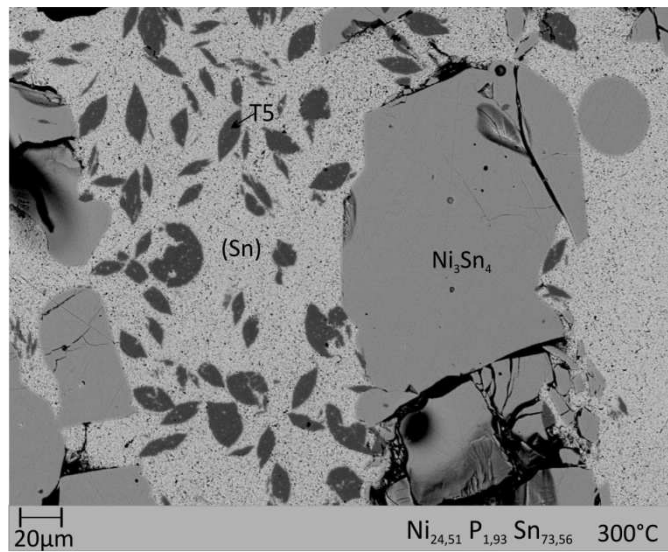


Fig. 5.16 SEM image of sample NPS 1

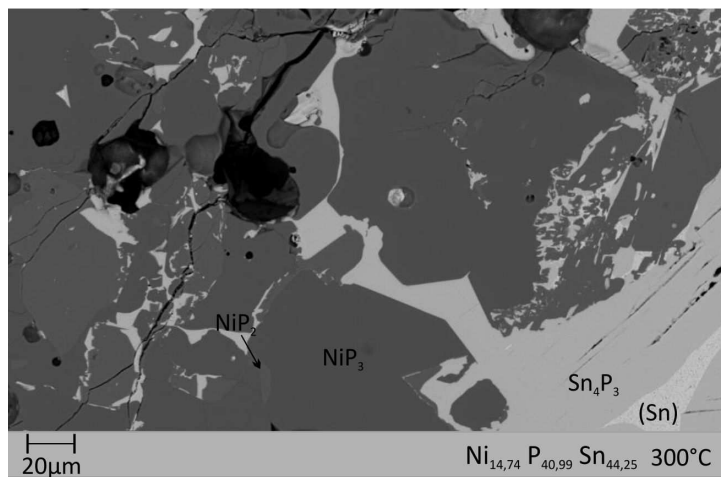


Fig. 5.17 SEM image of sample NPS 10

All of the interpretations are speculations and the system should be further investigated to ensure consistent and reliable results.

6 Summary

6.1 Summary (English)

In the electronic industry nickel is often used for protective coatings of metal surfaces, e.g. Cu, to protect them against corrosion, to increase the hardness or the solderability. These protective layers are usually applied by means of electroless plating using phosphorus-containing solutions. The Ni-P layers that are formed in this process can have a P content of up to 15 at%. During the soldering process there is an interaction of these Ni(P)-layers with the tin-rich solder alloy. This causes the formation of so called intermetallic compounds (IMC) in the solder joint. In order to explain the occurring reactions and the reaction products that are formed during the soldering process, it is necessary to investigate the corresponding phase diagrams.

In the present thesis, the systems Sn-P and Ni-Sn-P have been investigated. The binary system shows a strong dependence on the vapor pressure of phosphorus. Hence, isopiestic experiments with different vapor pressures of P were performed. Successful measurements were carried out at nine different pressures in a range from 0.006 to 0.69 bar and for these pressures phase diagrams could be created up to a P content of 70 at%. With the obtained data the change of the equilibrium temperatures of the formation reactions for the three binary compounds (Sn_4P_3 , Sn_3P_4 , SnP_3) with increasing pressure could be analyzed and extrapolated to 1 bar. Further, the pressure-dependent maximum solubility of phosphorus in the tin-rich liquidus was investigated according to the obtained results. Finally, partial thermodynamic properties of phosphorus, such as partial enthalpies of mixing and activities, as well as integral Gibbs energies of formation were derived and compared with literature data.

In the ternary system samples in the Sn-rich part of the phase diagram were prepared and then investigated by means of X-ray diffraction (XRD) and scanning electron microscopy (SEM). With these data an isothermal section at 300 ° C should have been created. However, phosphorus and its vapor pressure caused significant problems during sample preparation and interpretation of the results. Samples with a phosphorus content of more than 60 at% could not be used for evaluation. Some quartz tubes burst during the sample preparation, in other samples P condensed

during quenching on the quartz wall. Further, most samples with a P-content of more than 15 at% were not in thermodynamic equilibrium. These non-equilibrium samples were most likely obtained due to the influence of the gas phase and the low annealing temperature. As a result of these experimental difficulties, no reliable and consistent isothermal section of the Ni-Sn-P phase diagram could be created.

6.2 Zusammenfassung (Deutsch)

In der Elektronikindustrie wird Nickel oft zur Beschichtung von Metalloberflächen, z.B. Kupfer, verwendet um diese gegen Korrosion zu schützen, zu härten oder die Lötbarkeit zu erhöhen. Diese Beschichtung wird üblicherweise mittels electroless plating unter Verwendung von phosphorhaltigen Substanzen aufgetragen. Dabei werden Ni-P-Schichten gebildet, die einen P-Gehalt von bis zu 15 at% aufweisen können. Während des Lötvorgangs tritt diese Ni(P) Schicht mit zinnreichen Lötlegierungen in Kontakt. Die Qualität dieser Lötverbindungen ist ein wesentliches Thema in der Werkstoff- und Elektrotechnik, deshalb ist es von essentieller Bedeutung, die Bildung intermetallischer Verbindungen (IMC) an den Lötstellen zu verstehen. Um die auftretenden Reaktionen und entstehenden Verbindungen erklären zu können, ist es nötig die dazugehörigen Phasendiagramme zu erforschen.

In der vorliegenden Arbeit wurden die Systeme Sn-P und Ni-P-Sn untersucht. Das binäre System zeigt eine starke Abhängigkeit vom Dampfdruck des Phosphors. Diesbezüglich wurden isopiestiche Versuche mit unterschiedlichen P-Dampfdrücken durchgeführt. Für neun verschiedene Drücke im Bereich zwischen 0,006 und 0,69 bar konnten erfolgreich Phasendiagrammeversionen bis zu einem maximalen P-Gehalt von 70 at% erstellt werden. Mit den erhaltenen Daten wurden die Gleichgewichtstemperaturen der Bildungsreaktionen für die drei existierenden binären Verbindungen (Sn_4P_3 , Sn_3P_4 , SnP_3) für unterschiedliche Dampfdrücke verglichen und auf 1 bar extrapoliert. Weiters wurde die ebenfalls druckabhängige maximale Löslichkeit von Phosphor in der zinnreichen Flüssigkeit mit Hilfe der experimentellen Ergebnisse abgeschätzt. Abschließend wurden partielle thermodynamische Eigenschaften wie partielle Mischungsenthalpien und Phosphoraktivitäten sowie integrale Gibbs Bildungsenergien der binären Verbindungen abgeleitet und mit Literaturdaten verglichen.

Im ternären System wurden Proben im Sn-reichen Teil des Phasendiagramms hergestellt, und mit Hilfe von Röntgenbeugung (XRD) und Elektronenmikroskopie (SEM) Daten sollte ein isothermer Schnitt bei 300 °C erstellt werden. Die Probenherstellung sowie die Interpretation der Ergebnisse wurden jedoch maßgeblich durch den hohen Dampfdruck von Phosphor erschwert. Proben ab einem

Phosphorgehalt von mehr als 60 at% konnten nicht für die Auswertung herangezogen werden. Einige Quarzrohre explodierten während der Probenherstellung, in anderen Proben kondensierte P während des Abschreckens an der Quarzglaswand. Weiter waren die meisten Proben ab einem Phosphorgehalt von 15 at% auch nach langem Tempern nicht im thermodynamischen Gleichgewicht. Dies ist vermutlich auf die entstehende phosphorhaltige Gasphase in den Proben und die niedrige Gleichgewichtsglühtemperatur zurückzuführen. Aufgrund dieser experimentellen Schwierigkeiten konnte kein konsistenter isothermer Schnitt des Ni-P-Sn Phasendiagramms erstellt werden.

7 References

- [1] G.O. Mallory, J.B. Hajdu, *Electroless plating : fundamentals and applications*, American Electroplaters and Surface Finishers Society, 1990.
- [2] C. Schmetterer, *Investigations in the Systems Ni-P and Ni-P-Sn*, PhD-thesis, Univ. of Vienna, 2009.
- [3] A. Brenner, G.E. Riddell, *Nickel plating by chemical reduction*, in, *Application: US*, 1950.
- [4] K. Zeng, K.N. Tu, *Six cases of reliability study of Pb-free solder joints in electronic packaging technology*, *Mater. Sci. Eng., R*, R38 (2002) 55-105.
- [5] J.-W. Yoon, J.-H. Park, C.-C. Shur, S.-B. Jung, *Characteristic evaluation of electroless nickel-phosphorus deposits with different phosphorus contents*, *Microelectron. Eng.*, 84 (2007) 2552-2557.
- [6] M.O. Alam, Y.C. Chan, K.C. Hung, *Reliability study of the electroless Ni-P layer against solder alloy*, *Microelectron. Reliab.*, 42 (2002) 1065-1073.
- [7] K. Zeng, V. Vuorinen, J.K. Kivilahti, *Interfacial reactions between lead-free SnAgCu solder and Ni(P) surface finish on printed circuit boards*, *IEEE Trans. Electron. Packag. Manuf.*, 25 (2002) 162-167.
- [8] A. Kumar, Z. Chen, *Influence of solid-state interfacial reactions on the tensile strength of Cu/electroless Ni-P/Sn-3.5Ag solder joint*, *Mater. Sci. Eng., A*, A423 (2006) 175-179.
- [9] H.-S. Chun, J.-W. Yoon, S.-B. Jung, *Solid-state interfacial reactions between Sn-3.5Ag-0.7Cu solder and electroless Ni-immersion Au substrate during high temperature storage test*, *J. Alloys Compd.*, 439 (2007) 91-96.
- [10] M.O. Alam, Y.C. Chan, K.N. Tu, *Effect of reaction time and P content on mechanical strength of the interface formed between eutectic Sn-Ag solder and Au/electroless Ni(P)/Cu bond pad*, *J. Appl. Phys.*, 94 (2003) 4108-4115.
- [11] Y.-C. Lin, T.-Y. Shih, S.-K. Tien, J.-G. Duh, *Morphological and microstructural evolution of phosphorous-rich layer in SnAgCu/Ni-P UBM solder joint*, *J. Electron. Mater.*, 36 (2007) 1469-1475.
- [12] Y.-C. Lin, K.-J. Wang, J.-G. Duh, *Detailed Phase Evolution of a Phosphorous-Rich Layer and Formation of the Ni-Sn-P Compound in Sn-Ag-Cu/Electroplated Ni-P Solder Joints*, *J. Electron. Mater.*, 39 (2010) 283-294.

- [13] K. Chen, C. Liu, D.C. Whalley, D.A. Hutt, J.F. Li, S.H. Mannan, A comparative study of the interfacial reaction between electroless Ni-P coatings and molten tin, *Acta Mater.*, 56 (2008) 5668-5676.
- [14] Y.-C. Lin, J.-G. Duh, Optimal phosphorous content selection for the soldering reaction of Ni-P under bump metallization with Sn-Ag-Cu solder, *J. Electron. Mater.*, 35 (2006) 1665-1671.
- [15] Y.C. Sohn, J. Yu, S.K. Kang, D.Y. Shih, T.Y. Lee, Spalling of intermetallic compounds during the reaction between lead-free solders and electroless Ni-P metallization, *J. Mater. Res.*, 19 (2004) 2428-2436.
- [16] A.F. Holleman, E. Wiberg, *Lehrbuch der anorganischen Chemie*, 101. ed., de Gruyter, Berlin, 1995.
- [17] R.R. Hultgren, *Selected values of the thermodynamic properties of the elements*, Am.Soc.Met., Metals Park, Ohio, 1973.
- [18] T.B. Massalski, H. Okamoto, *Binary alloy phase diagrams*, 2nd ed., ASM International, Materials Park, Ohio, 1990.
- [19] A.C. Vivian, Tin-phosphorus alloys, *J.Inst. Metals.*, (1920) 325-366.
- [20] M. Hansen, K. Anderko, *Constitution of Binary Alloys*, 2d ed., McGraw-Hill, New York, 1958.
- [21] O. Olofsson, X-ray investigations of the tin-phosphorus system, *Acta Chem. Scand.*, 24 (1970) 1153-1162.
- [22] M. Arita, K. Kamo, Measurement of vapor pressure of phosphorus over tin-phosphorus alloys by dew point method, *Trans. Jpn. Inst. Met.*, 26 (1985) 242-250.
- [23] H. Okamoto, P-Sn (Phosphorus-Tin), *J. Phase Equil.*, 14 (1993) 263-264.
- [24] B. Predel, *Landolt-Börnstein, Group IV, Vol.5, Phase Equilibria, Crystallographic and Thermodynamic Data of Binary Alloys, Sub-Vol. I*, Springer Verlag, Berlin, in: O. Madelung (Ed.), 1998.
- [25] J.V. Levinsky, P-Sn (Phosphorus-Tin), in: G. Effenberger (Ed.) *Pressure Dependent Phase Diagrams of Binary Alloys*, 1997.
- [26] J.V. Zaikina, K.A. Kovnir, A.N. Sobolev, I.A. Presniakov, V.G. Kytin, V.A. Kulbachinskii, A.V. Olenev, O.I. Lebedev, G. Van Tendeloo, E.V. Dikarev, A.V.

- Shevelkov, Highly Disordered Crystal Structure and Thermoelectric Properties of Sn_3P_4 , *Chem. Mater.*, 20 (2008) 2476-2483.
- [27] R. Ganesan, A. Ciccioli, G. Gigli, H. Ipser, Thermochemical investigations in the tin-phosphorus system, *Int. J. Mater. Res.*, 102 (2011) 93-103.
- [28] C. Schmetterer, Ganesan, R. , Ipser, H. , Interaction of Sn-based Solders with Ni(P) Substrates: Phase Equilibria and Thermochemistry, in: K.N. Subramanian (Ed.) *Lead-free Solders: Materials Reliability for Electronics*, John Wiley & Sons, Ltd., 2012, pp. 71-113.
- [29] P. Eckerlin, Kischio W., Darstellung und Kristallstruktur der Phasen " Sn_4P_3 " und " Sn_4As_3 ", *Z. anorg. allg. Chemie*, 363 (1968).
- [30] O. Olofsson, Crystal structure of Sn_4P_3 , *Acta Chem. Scand.*, 21 (1967) 1659-1660.
- [31] J. Gullman, O. Olofsson, Crystal structure of tin phosphide and a note on the crystal structure of germanium phosphide, *J. Solid State Chem.*, 5 (1972) 441-445.
- [32] R. Ganesan, K.W. Richter, C. Schmetterer, H. Effenberger, H. Ipser, Synthesis of Single-Phase Sn_3P_4 by an Isopiestic Method, *Chem. Mater.*, 21 (2009) 4108-4110.
- [33] G. Katz, J.A. Kohn, J.D. Broder, Crystallographic data for tin monophosphide, *Acta Crystallogr.*, 10 (1957) 607.
- [34] P.C. Donohue, Synthesis, structure, and superconducting properties of new high-pressure forms of tin phosphide, *Inorg. Chem.*, 9 (1970) 335-337.
- [35] P. Villars, L.D. Calvert, *Pearson's handbook of crystallographic data for intermetallic phases*, 2nd ed., ASM International, Materials Park, OH, 1991.
- [36] J.V. Levinsky, Ni-P (Nickel- Phosphorous), in: G. Effenberger (Ed.) *Pressure Dependent Phase Diagrams of Binary Alloys*, 1997.
- [37] K.J. Lee, P. Nash, Ni-P (Nickel-Phosphorous), in: P. Nash (Ed.) *Phase diagrams of binary nickel alloys*, ASM International, Materials Park, OH, 1991.
- [38] P. Jolibois, Two New Phosphides of Nickel, *Compt. rend.*, 150 (1910) 106-108.
- [39] W. Biltz, M. Heimbrecht, Systematic study of affinity. The nickel phosphides, *Z. Anorg. Allg. Chem.*, 237 (1938) 132-144.
- [40] N. Konstantinov, Compounds of Nickel and Phosphorus, *Z. Anorg. Chem.*, 60 (1909) 405-415.

- [41] H. Nowotny, E. Henglein, X-ray investigation in the system nickel-phosphorus, *Z. physik. Chem.*, B40 (1938) 281-284.
- [42] L.M. Yupko, A.A. Svirid, S.V. Muchnik, Phase equilibriums in nickel-phosphorus and nickel-phosphorus-carbon systems, *Poroshk. Metall. (Kiev)*, (1986) 78-83.
- [43] S. Oryshchyn, V. Babizhetskyy, S. Chykhriy, L. Aksel'rud, S. Stoyko, J. Bauer, R. Guerin, Y. Kuz'ma, Crystal Structure of Ni_5P_2 , *Inorg. Mater.*, 40 (2004) 380-385.
- [44] C. Schmetterer, J. Vizdal, H. Ipser, A new investigation of the system Ni-P, *Intermetallics*, 17 (2009) 826-834.
- [45] H. Okamoto, Ni-P (Nickel-Phosphorus), *J. Phase Equilib. Diffus.*, 31 (2010) 200-201.
- [46] R. Kohlhaas, P. Duenner, N. Schmitz-Pranghe, Temperature dependence of lattice parameters of iron, cobalt, and nickel at high temperatures, *Z. Angew. Phys.*, 23 (1967) 245-249.
- [47] B. Aronsson, The crystal structure of Ni_3P (Fe_3P type), *Acta Chem. Scand.*, 9 (1955) 137-140.
- [48] S. Rundqvist, E. Larsson, Crystal structure of Ni_{12}P_5 , *Acta Chem. Scand.*, 13 (1959) 551-560.
- [49] S. Rundqvist, X-ray investigations of Mn_3P , Mn_2P , and Ni_2P , *Acta Chem. Scand.*, 16 (1962) 992-998.
- [50] M. Elfstrom, Crystal structure of Ni_5P_4 , *Acta Chem. Scand.*, 19 (1965) 1694-1704.
- [51] E. Larsson, X-ray investigation of the Ni-P system and the crystal structures of NiP and NiP_2 , *Ark. Kemi*, 23 (1965) 335-365.
- [52] S. Rundqvist, N.O. Ersson, Structure and bonding in skutterudite-type phosphides, *Ark. Kemi*, 30 (1968) 103-114.
- [53] E. Schlesinger Mark, The thermodynamic properties of phosphorus and solid binary phosphides, *Chem Rev*, 102 (2002) 4267-4301.
- [54] J.-H. Shim, H.-J. Chung, D.N. Lee, Calculation of phase equilibria and evaluation of glass-forming ability of Ni-P alloys, *J. Alloys Compd.*, 282 (1999) 175-181.
- [55] R. Ganesan, A.T. Dinsdale, H. Ipser, Thermochemistry of the nickel-phosphorus system, *Intermetallics*, 19 (2011) 927-933.

- [56] P. Nash, A. Nash, The Ni-Sn (nickel-tin) system, *Bull. Alloy Phase Diagrams*, 6 (1985) 350-359, 395-356.
- [57] C. Schmetterer, H. Flandorfer, K.W. Richter, U. Saeed, M. Kauffman, P. Roussel, H. Ipser, A new investigation of the system Ni-Sn, *Intermetallics*, 15 (2007) 869-884.
- [58] G. Ghosh, Thermodynamic modeling of the nickel-lead-tin system, *Metall. Mater. Trans. A*, 30A (1999) 1481-1494.
- [59] H.S. Liu, J. Wang, Z.P. Jin, Thermodynamic optimization of the Ni-Sn binary system, *CALPHAD Comput. Coupling Phase Diagrams Thermochem.*, 28 (2005) 363-370.
- [60] K. Schubert, W. Burkhardt, P. Esslinger, E. Gunzel, H.G. Meissner, W. Schutt, J. Wegst, M. Wilkens, Some structural results on metallic phases, *Naturwissenschaften*, 43 (1956) 248-249.
- [61] A. Leineweber, O. Oeckler, U. Zachwieja, Static atomic displacements of Sn in disordered NiAs/Ni₂In type HT-Ni_{1+δ}Sn, *J. Solid State Chem.*, 177 (2004) 936-945.
- [62] A. Leineweber, E.J. Mittemeijer, M. Knapp, C. Baehtz, In situ and ex situ observation of the ordering kinetics in Ni_{1.50}Sn, *Mater. Sci. Forum*, 443-444 (2004) 247-250.
- [63] A. Leineweber, M. Ellner, E.J. Mittemeijer, A NiAs/Ni₂In-Type Phase Ni_{1+x}Sn (0.35<x<0.45) with Incommensurate Occupational Ordering of Ni, *J. Solid State Chem.*, 159 (2001) 191-197.
- [64] A. Leineweber, Variation of the crystal structures of incommensurate LT¹-Ni_{1+δ}Sn (δ = 0.35, 0.38, 0.41) and commensurate LT-Ni_{1+δ}Sn (δ = 0.47, 0.50) with composition and annealing temperature, *J. Solid State Chem.*, 177 (2004) 1197-1212.
- [65] W. Mikulas, L. Thomassen, C. Upthegrove, Equilibrium relations in the nickel-tin system, *Am. Inst. Mining Met. Eng., Inst. Metals Div., Tech. Pub., No. 814* (1937) 23 pp.
- [66] C. Schmetterer, J. Vizdal, A. Kroupa, A. Kodentsov, H. Ipser, The Ni-rich Part of the Ni-P-Sn System: Isothermal Sections, *J. Electron. Mater.*, 38 (2009) 2275-2300.
- [67] V. Keimes, H.M. Blume, A. Mewis, Preparation and crystal structure of ANi₁₀P₃ (A: Zn, Ga, Sn, Sb), *Z. Anorg. Allg. Chem.*, 625 (1999) 207-210.
- [68] C. Schmetterer, M. Wildner, G. Giester, K.W. Richter, H. Ipser, The crystal structure of Ni₂₁Sn₂P₆, *Z. Anorg. Allg. Chem.*, 635 (2009) 301-306.

- [69] F.J. Garcia-Garcia, A.K. Larsson, S. Furuseth, The crystal structure of $\text{Ni}_{10}\text{Sn}_5\text{P}_3$, *J. Solid State Chem.*, 166 (2002) 352-361.
- [70] F.J. Garcia-Garcia, A.K. Larsson, S. Furuseth, The crystal structure of $\text{Ni}_{13}\text{Sn}_8\text{P}_3$ elucidated from HREM, *Solid State Sci.*, 5 (2003) 205-217.
- [71] S. Furuseth, H. Fjellvaag, Properties of the NiAs-type phase $\text{Ni}_{1+m}\text{Sn}_{1-x}\text{P}_x$, *Acta Chem. Scand.*, 48 (1994) 134-138.
- [72] S. Furuseth, H. Fjellvaag, Crystal structure and properties of nickel tin phosphide (Ni_2SnP), *Acta Chem. Scand., Ser. A*, A39 (1985) 537-544.
- [73] Z.P. Xia, Y. Lin, Z.Q. Li, A new phase in Ni-Sn-P system and its property as an anode material for lithium-ion batteries, *Mater. Charact.*, 59 (2008) 1324-1328.
- [74] Y.K. Jee, J. Yu, Y.H. Ko, Effects of Zn addition on the drop reliability of $\text{Sn}_{-3.5}\text{Ag}_x\text{Zn/Ni(P)}$ solder joints, *J. Mater. Res.*, 22 (2007) 2776-2784.
- [75] C.-w. Hwang, K. Suganuma, M. Kiso, S. Hashimoto, Interface microstructures between Ni-P alloy plating and Sn-Ag-(Cu) lead-free solders, *J. Mater. Res.*, 18 (2003) 2540-2543.
- [76] C. Schmetterer, H. Ipser, Ni-Rich Part of the System Ni-P-Sn: Thermal Behavior, *Metall. Mater. Trans. A*, 41A (2010) 43-56.
- [77] W.R. Bousfield, C.E. Bousfield, Vapor pressure and density of sodium chloride solutions, *Proc. R. Soc. London, Ser. A*, 103 (1923) 429-443.
- [78] D.A. Sinclair, A simple method for accurate determinations of vapor pressure of solutions, *J. Phys. Chem.*, 37 (1933) 495-504.
- [79] R.H. Stokes, The measurement of vapor pressure of aqueous solutions by bi-thermal equilibrations through the vapor phase, *J. Am. Chem. Soc.*, 69 (1947) 1291-1296.
- [80] P. Herasymenko, Thermodynamic properties of solid solutions. I. Vapor pressures of cadmium over alpha silver-cadmium alloys, *Acta Metall.*, 4 (1956) 1-6.
- [81] H.W. Rayson, W.A. Alexander, Isopiestic techniques applied to phase-diagram determination in the systems silver-cadmium and copper-cadmium, *Can. J. Chem.*, 35 (1957) 1571-1575.

- [82] H. Ipsler, R. Krachler, K.L. Komarek, The isopiestic method and its application to a thermodynamic study of the gold-zinc system, NATO ASI Ser., Ser. C, 286 (1989) 293-306.
- [83] K.W. Richter, VO Charakterisierung anorganischer Materialien - Methoden und Modellierung, B Methods for combination., (2009).
- [84] C. Suryanarayana, M.G. Norton, X-Ray diffraction : a practical approach, Plenum Press, New York, 1998.
- [85] K. H.G., Microscopy from the very beginning, [http://www.zeiss.de/C1256B5E0051569F/EmbedTitelIntern/Microscopy_from_the_very_beginning\\$File/Microscopy_from_the_very_beginning.pdf](http://www.zeiss.de/C1256B5E0051569F/EmbedTitelIntern/Microscopy_from_the_very_beginning$File/Microscopy_from_the_very_beginning.pdf), (1994).
- [86] Geochemical Instrumentation and Analysis, available from: http://serc.carleton.edu/research_education/geochemsheets/browse.html, (14.05.2012).
- [87] Schematic illustration SEM, available from: http://www4.nau.edu/microanalysis/Microprobe-SEM/Images/SEM_schematic.jpg, (15.05.2012).
- [88] T. Gnanasekaran, H. Ipsler, Thermodynamic properties of ternary liquid Cu-Mg-Ni alloys, Metall. Mater. Trans. B, 25B (1994) 63-72.
- [89] Nanozentrum. Physikalisches Institut Wien, Available from: <http://nanozentrum.univie.ac.at/home/zeiss-supra-55-vp/>, (27.03.2012).
- [90] A.T. Dinsdale, SGTE data for pure elements, CALPHAD Comput. Coupling Phase Diagrams Thermochem., 15 (1991) 317-425.
- [91] M. Arita, M. Watanabe, Equilibrium constant of gaseous reaction $2P_2 = P_4$ and vapor pressure of liquid phosphorus, Trans. Jpn. Inst. Met., 26 (1985) 175-182.

8 Appendices

8.1 List of figures

Fig. 1.1 Schematic illustration of UBM-process with ENIG-protected Cu	3
Fig. 2.1 Binary Sn-P phase diagram according to Massalski [18].....	5
Fig. 2.2 Isobaric Sn-P phase diagram at a P pressure of 0.7 bar according to Levinsky [25]	6
Fig. 2.3 Ni-P phase diagram according to Okamoto [44].....	10
Fig. 2.4 Enlarged Ni-P phase diagram (18-40 at%P) according to Okamoto [44].....	10
Fig. 2.5 Ni-Sn phase diagram according to Massalski [18] (based on Nash and Nash [55])	13
Fig. 2.6 Ni-Sn phase diagram according to Schmetterer et al. [56].....	14
Fig. 2.7 Partial isothermal section of the ternary system Ni-P-Sn at 550°C according to Schmetterer et al. [65].....	18
Fig. 3.1 Schematic illustration of an X-ray tube.....	20
Fig. 3.2 The element Cu (a) the process of emission of characteristic $K\alpha$ X-rays and (b) its X-ray spectrum [82].....	21
Fig. 3.3 Diffraction according to Bragg's law	22
Fig. 3.4 Schematic illustration of an SEM according to [86].....	26
Fig. 3.5 Interaction of the primary electrons with the sample.....	27
Fig. 4.1 a) Two- zone furnaces with control units b) Furnace chamber	29
Fig. 4.2 Schematic of mini-isopiestic experimental setup	29
Fig. 4.3 graphite crucible.....	30
Fig. 4.4 Sealed tube before experiment;	30
Fig. 4.5 a) Quartz glass tube after the experiment, mixture of red and white phosphorus (reddish-yellow color) b) White phosphorus condensed on the inner quartz glass wall.....	31
Fig. 4.6 Bruker D8 diffractometer and measuring device.....	32
Fig. 4.7 sealed samples of Ni-P-Sn	33
Fig. 4.8 samples that could not be used for analysis due to a) Bursting in the furnace b) Extensive evaporation of phosphorus	34
Fig. 4.9 prepared samples in the system Ni-P-Sn	35
Fig. 4.10 embedded samples	36
Fig. 4.11 Zeiss Supra 55 VP.....	37
Fig. 5.1 schematic construction of the P-Sn phase diagram, superimposition of all isopiestic experiments	40

Fig. 5.2 T-x section of the P-Sn phase diagram at 1.023 bar	42
Fig. 5.3 T-x phase diagram of Sn-P at various pressures a)0.0058; b)0.0717; c)0.1270; d)0.1680; e)0.2428; f)0.3423; g)0.5155; h)0.5501, i)0.6926 bar;	45
Fig. 5.4 Variation of the phosphorus vapor pressure over the two-phase fields (a)(L+Sn ₄ P ₃) ----- (b)(Sn ₄ P ₃ +Sn ₃ P ₄)----- (c) (Sn ₃ P ₄ +SnP ₃)-----	46
Fig. 5.5 Variation of the P ₄ partial pressure with temperature of the reaction L+G=Sn ₄ P ₃ ; isopiestic experiments	48
Fig. 5.6 phosphorous pressure p as a function of the composition of the limiting liquidus	51
Fig. 5.7 logarithm of the phosphorous pressure logp as a function of the composition of the limiting liquidus	51
Fig. 5.8 Variation of the P ₄ partial pressure with temperature of the reaction G+Sn ₄ P ₃ =Sn ₃ P ₄ ; isopiestic experiments	53
Fig. 5.9 Variation of the P ₄ partial pressure with temperature of the reaction G+Sn ₃ P ₄ =SnP ₃ ; isopiestic experiments.....	55
Fig. 5.10 calculated speciation of the gas phase of white phosphorus according to Ganesan [54].....	57
Fig. 5.11 Natural logarithm of the phosphorus activity ln a _p as a function of the composition in the liquid phase at 750K.....	62
Fig. 5.12 Variation of the standard molar Gibbs energy of formation of Sn ₄ P ₃ (s) with temperature	63
Fig. 5.13 Variation of the standard molar Gibbs energy of formation of Sn ₃ P ₄ (s) with temperature	66
Fig. 5.14 Variation of the standard molar Gibbs energy of formation of SnP ₃ (s) with temperature	68
Fig. 5.15 partial isothermal section of the Ni-P-Sn system at 300 °C;	72
Fig. 5.16 SEM image of sample NPS 1	73
Fig. 5.17 SEM image of sample NPS 10	73

8.2 List of tables

Tab.2.1 Crystal structure data in the system Sn-P.....	8
Tab. 2.2 Crystal structure data of the system Ni-P (comp. maximum range according to Okamoto [44])	11
Tab. 2.3 Invariant reactions in the system Ni-P according to Schmetterer et al. [43] ...	12
Tab. 2.4 Ni-Sn crystal structure data according to Schmetterer et al.[56].....	15
Tab. 2.5 Invariant reactions in the system Ni-Sn according to Schmetterer et al. [56] .	15
Tab. 2.6 the ternary Ni-P-Sn phases according to Schmetterer et al. [65].....	17
Tab. 4.1 Overview of all isopiestic runs in the system Sn-P	31
Tab. 4.2 temperature programs for annealing at 300 and 550 °C	34
Tab. 4.3 sample composition and annealing procedures.....	35
Tab.5.1 Isopiestic experimental results	38
Tab.5.2 Results for the equilibrium $L+G = Sn_4P_3$	49
Tab. 5.3 results for the limiting liquidus composition	50
Tab. 5.4 Results for the equilibrium $G+Sn_4P_3=Sn_3P_4$	53
Tab. 5.5 Results for the equilibrium $G+Sn_3P_4=SnP_3$	55
Tab. 5.6 thermodynamic data obtained from the isopiestic experiments.....	59
Tab. 5.7 results for the standard molar Gibbs energy of formation of Sn_4P_3 (s).....	64
Tab. 5.8 results for the standard molar Gibbs energy of formation of Sn_3P_4 (s).....	66
Tab. 5.9 results for the standard molar Gibbs energy of formation of SnP_3 (s).....	68
Tab. 5.10 Experimental results of phase analysis of the Ni-P-Sn system.....	70

8.3 Curriculum vitae

Anna Ritscher

Vienna, Austria

Degree	Bakk. rer. nat
Nationality	Austria

Education

- 10/2009-07/2012 **Master studies of Chemistry, University of Vienna, Austria**
 specialising in Materials Chemistry and Physical Chemistry
 thesis 08/2011 - 06/2012, Institute of Inorganic Chemistry/Materials Chemistry
 topic: Pressure Dependence of the Sn-P phase diagram and investigations in the
 ternary System Ni-P-Sn
- 10/2006-10/2009 **Bachelor studies of Chemistry, University of Vienna, Austria**
 thesis 05-06/2009, Institute of Inorganic Chemistry/Materials Chemistry
 thesis title: Syntheses und Structural Analyses of $\text{Mo}(\text{Si}_{1-x}\text{Al}_x)_2$ in the Ternary System
 Al-Mo-Si
- 1998-2006 **Secondary school, BG/BRG Villach Perau, Austria**
 school leaving exam 6/2006 with success
- 1994-1998 **Elementary school, VS1 Villach, Austria**

International Experience

- 01/2010-08/2010 **ERASMUS semester, Institute of DNA-sensors, UAB Barcelona, Barcelona, Spain**
 research topic: Electrochemical Impedance Spectroscopy of Genosensors containing
 Nf-Polyanilin

Professional Experience

- 08-09/2009 **LUA Carinthia, Austria**
 internship, water laboratory
 quality control of drinking water, fountains and public swimming pools
- 08-09/2008 **Chemson Polymere – Additive AG Arnoldstein, Austria**
 internship, department of research and development
- 07-08/2007 **Omya GesmbH Gummern, Austria**
 internship, laboratory
- 07/2006 + 08/2005 **Hospital LKH Villach, Austria**
 internship, office

Teaching Experience

03/2012-07/2012 **Tutor, University of Vienna, Austria**
Basic Chemistry Laboratory Course I – Introductory Lab Course
Supervisor of a group: Basic Chemistry Laboratory Course I - Proseminar

Awards

2010 Performance Scholarships, University of Vienna, offered by the BMWF
2008 Performance Scholarships, University of Vienna, offered by the BMWF
2007 Performance Scholarships, University of Vienna, offered by the BMWF

Languages

German Mother tongue
English Fluent in spoken and written
Spanish Advanced, training ongoing
French Basic
Russian Basic

Publications

11/2010 N.Ponweiser, W.Paschinger, A.Ritscher, J.C.Schuster, K.W.Richter;
Phase Equilibria In The Al-Mo-Si System;
Intermetallics,19,3,409-418

Vienna, June/2012